



Influence of Strut Radius and Relative Density of Lattice Structures used as Sandwich Panels' Core

Diogo Miguel Rosa Pereira

Thesis to obtain the Master of Science Degree in

Mechanical Engineering

Supervisors: Prof. Maria de Fátima Reis Vaz
Eng. Manuel de Figueiredo Cravo Relvas Sardinha

Examination Committee

Chairperson: Prof. Luís Filipe Galvão dos Reis
Supervisor: Prof. Maria de Fátima Reis Vaz
Member of the Committee: Prof. Augusto Manuel Moura Moita de Deus

January 2021

Dedicated to Avô Pimpão. I promised you would have seen me with my masters finished and working.
Sorry for not fulfilling that promise.

Acknowledgments

Firstly, I would like to thank Prof. Fátima Vaz and Prof. Manuel Sardinha for their help, guidance, availability and teachings during the development of this thesis.

I would like to thank Frederico Alves for all the unimaginable support and patience he had when assisting me with the numerical simulations.

I also thank all my colleagues from Lab2ProD who never hesitated to stop whatever they were doing to help me when I needed.

I thank all the teachers associated to the Lab2ProD for all their inputs, suggestions and criticisms made during our biweekly meetings.

I would like to thank all my friends and university colleagues who accompanied me during these years at Instituto Superior Técnico. Thank you all for making this journey easier. A special mention to João Lobo, who supported me whenever I needed for every course and even during this master's thesis.

I thank Greta for motivating and cheering me up on my worst days.

Finally, and most importantly, I thank my entire family for all the support given to me during these years. I can't wait to have the honor to help them when they need.

Resumo

Painéis sanduíche com núcleo em favo de mel são extensamente utilizados em várias indústrias. Recentemente vários estudos foram desenvolvidos sobre a possibilidade de substituir o favo de mel por uma estrutura do tipo treliças, chamadas lattices. Esta opção mantém os elevados valores de rigidez, resistência mecânica e absorção de energia, e torna a estrutura mais leve.

O principal objetivo desta dissertação é investigar a influência que o raio e densidade relativa da estrutura treliçada básica têm no comportamento à flexão dos painéis sanduíche. Uma investigação feita anteriormente estudou a topologia de estruturas em lattice, e usou várias geometrias paralelepípedicas baseadas nas estruturas cristalinas atômicas. Essa investigação concluiu que a melhor opção seria uma geometria de corpo e face centrados com colunas no eixo z (body and face centered geometry with z-strut, BFCZ). No presente trabalho, estudaram-se os valores de densidade relativa utilizados de 0.25, 0.3 e 0.35 e os valores de raio utilizados foram 0.8 mm, 0.92 mm e 1.1 mm. Para estudar todas as combinações de raio e densidade relativa existentes, foram criados nove painéis em sanduíche. A abordagem experimental e numérica foram utilizadas para avaliar o comportamento das estruturas em testes de flexão a três pontos. A análise numérica foi realizada utilizando o software Siemens NX. Usou-se um processo de fabrico aditivo, designado por fused deposition modelling (FDM) ou também denominado por fused filament fabrication (FFF) para imprimir as nove estruturas em ácido polilático neutro. Os painéis em sanduíche são constituídos por núcleos em lattice formados pela repetição da estrutura celular unitária e por duas faces finas, uma superior e outra inferior ao núcleo. Estes três elementos foram fabricados juntos através de FDM. Posteriormente, estes provetes foram testados experimentalmente para avaliar a sua resposta mecânica à flexão e o tipo de falha apresentada.

Os resultados obtidos apontam para o fato de que a diminuição da densidade relativa das estruturas resultar em maior resistência mecânica e maior rigidez. Também foi concluído que a variação do raio terá diferentes resultados dependente da densidade relativa das estruturas. Para valores baixos de densidade relativa, o aumento do raio leva ao aparecimento de um valor mínimo de resistência e rigidez. No entanto, a mesma variação de raio feita a estruturas com alta densidade relativa leva ao aparecimento de um valor máximo de resistência e rigidez. Em relação à absorção de energia, nenhuma tendência foi encontrada quando se varia a densidade relativa ou o raio.

Palavras-chave: Painéis sanduíche, estrutura lattice, topologia, ensaio de flexão a três pontos, método de elementos finitos, fused deposition modeling

Abstract

Sandwich panels with a honeycomb core are extensively used in various industries. Recently, several studies were developed on the possibility of replacing the honeycomb with a lattice structure. This option preserves the high values of strength, high stiffness and energy absorption, and the structure becomes lighter.

The main objective of this research is to investigate the influence that the strut radius and the relative density of the basic lattice structure have on the flexural behaviour of the sandwich panels. A research on the topology of the basic lattice structure was previously made using various geometry based on the crystalline structure with parallelepiped arrangements inspired in atomic structures. This research concluded that the best option would be a geometry with body and face centered geometry with z-struts (BCFZ). In the present work, the values of relative density used were 0.25, 0.3 and 0.35 and the values of radius used were 0.8 mm, 0.92 mm and 1.1 mm. In order to study all the possible combinations, 9 sandwich panels were designed. Experimental and numerical analysis were used to evaluate the behaviour of the structures under 3-point bending. The numerical analysis was made using the Siemens NX software. The fused deposition modeling (FDM), also denoted by fused filament fabrication (FFF) was used to print the nine structures using polylactic neutral acid. The sandwich panels manufactured had a core made by the repetition of the basic lattice structure and two thin skins, one above and the other below the core. These three elements were all manufactured together using FDM. Afterwards, these structures were subjected to experimental tests to evaluate their mechanical flexural response and the type of failure was assessed.

The results found suggest that decreasing the relative density of the structures leads to an improvement in the strength and stiffness of the panels. It was also found that varying the strut radius of the structures would lead to different variations of the measured parameters dependently of the relative density of the structures. At high values of relative density, there are minimal values of strength and stiffness dependent on the strut radius but at lower values of relative density the same variation of strut radius leads to maximum values of strength and stiffness. Regarding the energy absorption, no trend was found when varying the relative density or radius.

Keywords: Sandwich panels, lattice structure, topology, 3-point bending test, finite element method, fused deposition modeling

Contents

- Acknowledgments v
- Resumo vii
- Abstract ix
- List of Tables xiii
- List of Figures xv
- Nomenclature xix

- 1 Introduction 1**
- 1.1 Motivation 1
- 1.2 Background 1
- 1.3 Objectives 2
- 1.4 Thesis Outline 2

- 2 Literature review 3**
- 2.1 Sandwich Panels 3
- 2.2 Core - Materials and Analysis 4
 - 2.2.1 Two Dimensional Structures - Honeycomb Structures 4
 - 2.2.2 Three Dimensional Structures 6
- 2.3 Additive Manufacturing 7
- 2.4 Fused Deposition Modelling 8
 - 2.4.1 FDM Printing Process 8
 - 2.4.2 FDM Parameters 11
 - 2.4.3 FDM Printing Defects 16
- 2.5 Behaviour of a cell in a Cellular Material 19
- 2.6 Meta-materials 20
 - 2.6.1 Lattice Structures 21
 - 2.6.2 Relative Density 23
- 2.7 Failure Modes and Mechanisms of Lattice Structures 24

- 3 Materials and Methods 29**
- 3.1 Design 29
 - 3.1.1 Material 29

3.1.2	Specimens Design	30
3.2	Specimens Manufacture	39
3.3	Experimental Procedure	42
3.4	Numerical Simulation	44
3.4.1	Part file	44
3.4.2	Fem file	45
3.4.3	Sim File	48
3.4.4	Solution Solver	50
3.4.5	Mesh Refinement	50
4	Results	53
4.1	Numerical Simulations	53
4.2	Experimental Results	60
4.2.1	Failure Observations	65
4.3	Comparison between methods	68
5	Conclusions	75
5.1	Achievements	75
5.2	Future Work	76
	Bibliography	77
	A Technical drawings	83
	B Manufacturing Parameters	93

List of Tables

2.1	Properties of ABS and PLA [35]	15
3.1	PLA-N properties of the material used [66]	30
3.2	Study of the height and relative density for specimens with 0.8 mm of radius	33
3.3	Study of the height and relative density for specimens with 0.92 mm of radius	34
3.4	Study of the height and relative density for specimens with 1.1 mm of radius	35
3.5	Dimensions and relative densities of the specimens. ρ_{Rel} is the real relative density obtained from the CAD software, ρ_{Teo} is the theoretical relative density that was desired and e_{Rel} (%) is the relative error between both.	37
3.6	Dimensions of the structures	38
3.7	Number of cell repetitions in the length and width directions	39
3.8	Dimensions of the specimens measured after manufacturing and theoretical printing times	41
3.9	Midspan and overhang distances	42
3.10	Results of the mesh refinement applied to the 2D bounded planes	52
4.1	FEA Results	53
4.2	FEA Results, specifically the force applied to the top roller, the maximum von Mises stress registered in the top skin, the stiffness and the absorbed energy by the specimens until a displacement of 4 mm	58
4.3	FEA results, where the specimens are grouped by radius	59
4.4	FEA results, where the specimens are grouped by relative density	59
4.5	Experimental results, specifically the force applied to the top roller, the stiffness and the absorbed energy by the specimens until the fracture	64
4.6	Specimens grouped according to their fracture modes. Mode 1 corresponds to the failure of the struts; mode 2 corresponds to failure in the connection between the struts and top skin; mode 3 corresponds to mixed failure mode	65

- 4.7 Values of the rupture displacement (d_{Fail}), maximum load (Load), stiffness (k) and energy absorption (E) from the numerical and experimental results. "Num" and "Exp" refer to numerical and experimental values, respectively. All the experimental values presented are averages of the values of each specimen. All the numerical values were calculated using the average rupture displacement. In this table the specimens are grouped according to the strut radius (specimens 1, 2 and 3 have a strut radius of 0.8 mm; specimens 4, 5 and 6 have strut a radius of 0.92 mm; specimens 7, 8 and 9 have strut a radius of 1.1 mm). 70
- 4.8 The same values of the rupture displacement (d_{Fail}), maximum load (Load), stiffness (k) and energy absorption (E) from the numerical and experimental results that were presented in table 4.7 but in this table the specimens are grouped according to their relative density (specimens 1, 4 and 7 have a relative density of 0.25; specimens 2, 5 and 8 have a relative density of 0.3; specimens 3, 6 and 9 have strut a relative density of 0.25). 70

List of Figures

2.1	Components of a sandwich panel [3]	3
2.2	Honeycomb Sandwich Panel	4
2.3	Manufacturing of a honeycomb core using adhesive bonding and the expansion process	5
2.4	Manufacturing of a honeycomb core using adhesive bonding and the corrugation method [7]	5
2.5	Typical cellular structure [6]	6
2.6	Properties of a cellular material [6]	6
2.7	Idealization of a cell from a cellular material [6]	7
2.8	The various methods of additive manufacturing [28]	8
2.9	The FDM printing process [28]	9
2.10	Approximation of pherical surface using stereolithography with different degrees of approximation [29]	9
2.11	Ultimaker Cura, the splicer program used for this research	10
2.12	Movements of the printer head and of the build plane [30]	11
2.13	Part printed with the same shell thickness but different percentages of infill [31]	12
2.14	Building direction considering the stresses applied [32]	13
2.15	Overhangs and bridges represented by the letters Y, H and T [33]	13
2.16	Overhangs with and without the need of support which depends on the angle with the horizontal. In the first figure, the angle with the horizontal is 45 degrees, so there is no need of support. In the second figure, the angle with the horizontal is smaller than 45 degrees so support is needed. [34]	14
2.17	Failure caused by printing the letter T without support [33]	14
2.18	Dividing a part that needs a support structure into two that do not need support structures. [32]	14
2.19	Diagram of materials used in FDM. [28]	15
2.20	Edge Warping of an FDM part caused by the existing stresses in the layers [37]	17
2.21	Example of print fail due to bad adhesion	17
2.22	Print made for this work that failed.	18
2.23	Filament that was ground during the manufacture of specimens	19
2.24	Compressive stress-strain behaviour of a bending-dominated lattice [6]	20

2.25 Bending-dominated lattice under stress [6]	20
2.26 Examples of metamaterials [38]	21
2.27 Various examples of shoes that use 3D printed lattice structures [40–42]	22
2.28 3D printed bicycle saddle [45]	23
2.29 American Football helmet which uses 3D printed struts [46]	23
2.30 Pavilion made of 3D printed lattice structures [43]	23
2.31 High porosity - cellular solid [58]	24
2.32 Low porosity - isolated pores in solid [58]	24
2.33 Example of a lattice structure under 3PB loading [59]	25
2.34 Failure modes of a sandwich beam under 3PB loading [59]	26
3.1 PLA-N spool used in this work [64]	29
3.2 Core unit geometries studied by Monteiro et al. [5]. (a) BC - Body Centred; (b) BCZ - Body Centred with Z axis struts; (c) BFCZ - Body and Face Centred with Z axis struts; FCZ - Face Centred with Z axis struts; PS - Parallelepipedic Simple. [5]	30
3.3 Unit Cell 1	36
3.4 Unit Cell 2	36
3.5 Unit Cell 3	36
3.6 Unit Cell 4	36
3.7 Unit Cell 5	36
3.8 Unit Cell 6	36
3.9 Unit Cell 7	37
3.10 Unit Cell 8	37
3.11 Unit Cell 9	37
3.12 Specimen 5 - one example of the specimens designed for this study	39
3.13 Ultimaker 3 - The 3D printer used to manufacture all the specimens	40
3.14 Two photographs taken during the printing process. In these photographs, we can see that two specimens are being printed at the same time. This option, despite being valid, is more prone to printing problems.	40
3.15 Loading diagram of a 3PB test	42
3.16 Two different specimens before the beginning of the experimental procedure	43
3.17 Instron 3369 with a specimen prior to initiating a procedure	43
3.18 One of the part files created	45
3.19 One of the fem files created	46
3.20 1D mesh characteristics	46
3.21 1D point to face connections characteristics	46
3.22 2D mesh characteristics	47
3.23 3D mesh characteristics	47
3.24 A sim file created	48

3.25 Contact parameters used for both contacts	49
3.26 Enforced displacement constraint parameters	49
3.27 Constraint for the struts when using a y0z symmetry plane	49
3.28 Constrain for the polygon edges when using a x0z symmetry plane	49
3.29 Solution characteristics - The case control section where the outputs are defined and bulk data section where the solution parameters are defined.	50
3.30 Mesh refinement for the specimen 1	51
3.31 Mesh refinement for the specimen 2	51
3.32 Mesh refinement for the specimen 3	51
3.33 Mesh refinement for the specimen 4	51
3.34 Mesh refinement for the specimen 5	51
3.35 Mesh refinement for the specimen 6	51
3.36 Mesh refinement for the specimen 7	52
3.37 Mesh refinement for the specimen 8	52
3.38 Mesh refinement for the specimen 9	52
4.1 FEA of the specimen 1 under a 3PB test. The first picture presents the vertical displace- ment, the second picture presents the σ_{VM} on the skins and the third picture presents the vertical reaction forces applied to the rollers.	54
4.2 FEA of the specimen 2 under a 3PB test. The results presented are the σ_{VM} on the skins elements.	55
4.3 FEA of the specimen 3 under a 3PB test. The results presented are the σ_{VM} on the skins elements.	55
4.4 FEA of the specimen 4 under a 3PB test. The results presented are the σ_{VM} on the skins elements.	56
4.5 FEA of the specimen 5 under a 3PB test. The results presented are the σ_{VM} on the skins elements.	56
4.6 FEA of the specimen 6 under a 3PB test. The results presented are the σ_{VM} on the skins elements.	56
4.7 FEA of the specimen 7 under a 3PB test. The results presented are the σ_{VM} on the skins elements.	57
4.8 FEA of the specimen 8 under a 3PB test. The results presented are the σ_{VM} on the skins elements.	57
4.9 FEA of the specimen 9 under a 3PB test. The results presented are the σ_{VM} on the skins elements.	57
4.10 Numerical load-displacement curves of all the specimens analysed in this document . . .	58
4.11 Experimental load-displacement curves of all the specimens 1	61
4.12 Experimental load-displacement curves of all the specimens 2	61
4.13 Experimental load-displacement curves of all the specimens 3	61

4.14 Experimental load-displacement curves of all the specimens 4	62
4.15 Experimental load-displacement curves of all the specimens 5	62
4.16 Experimental load-displacement curves of all the specimens 6	62
4.17 Experimental load-displacement curves of all the specimens 7	63
4.18 Experimental load-displacement curves of all the specimens 8	63
4.19 Experimental load-displacement curves of all the specimens 9	63
4.20 First fracture mode - Failure of the struts. The red circles highlight the failure of the struts.	66
4.21 Second fracture mode - Failure of the connection between the struts and the top skin. . .	66
4.22 Third fracture mode - Mixed failure mode with total rupture of struts and skins in its mid- plane.	67
4.23 Comparison between the experimental load-displacement curves and the numerical sim- ulation of specimen 1	71
4.24 Comparison between the experimental load-displacement curves and the numerical sim- ulation of specimen 2	71
4.25 Comparison between the experimental load-displacement curves and the numerical sim- ulation of specimen 3	71
4.26 Comparison between the experimental load-displacement curves and the numerical sim- ulation of specimen 4	72
4.27 Comparison between the experimental load-displacement curves and the numerical sim- ulation of specimen 5	72
4.28 Comparison between the experimental load-displacement curves and the numerical sim- ulation of specimen 6	72
4.29 Comparison between the experimental load-displacement curves and the numerical sim- ulation of specimen 7	73
4.30 Comparison between the experimental load-displacement curves and the numerical sim- ulation of specimen 8	73
4.31 Comparison between the experimental load-displacement curves and the numerical sim- ulation of specimen 9	73

Nomenclature

ρ_{Rel}	Relative Density
ρ_{Teo}	Theoretical relative density
σ_{VM}	Maximum von Mises stress
E	Young's Modulus
E_{absExp}	Experimental value of the absorbed energy
E_{absNum}	Numerical value of the absorbed energy
H_u	Unit cell height
K	Initial Stiffness
L	Length of specimens
L_u	Unit cell length
T	Total thickness of specimens
t_c	Core thickness
t_p	Plate thickness
v	Printing velocity
V_{Pol}	Volume of polygon inscribing the core unit
V_{unit}	Volume of the core unit
W	Width of specimens
W_u	Unit cell width
1D	One Dimensional
2D	Two Dimensional
3D	Three Dimensional
3PB	Three Point Bending

δ Percent relative error

ABS Acrylonitrile Butadiene Styrene

AISI American Iron and Steel Institute

AM Additive Manufacturing

ASTM American Society for Testing and Materials

BFCZ Body and Face Centred with z-struts

CAD Computer Aided Design

d Fail Rupture displacement

FDM Fused Deposition Modeling

FEA Finite Element Analysis

FEM Finite Element Method

FFF Fused Filament Fabrication

K Exp Experimental value of the initial stiffness

K Num Numerical value of the initial stiffness

Load Exp Maximum experimental load registered

Load Num Maximum numerical load registered

NC Numerical Control

PLA Polylactic Acid

PLA-N Polylactic Neutral Acid

SLM Selective Laser Melting

STL Standard Triangle Language

Chapter 1

Introduction

The goal of structural engineering is to design parts that have high stiffness and strength with the lowest weight possible. One part that is commonly used and also meets these requirements are sandwich panels. Sandwich panels are used in various industries due to their high versatility and extremely advantageous properties but conserving a relative low weight. The core of these panels is where the most alteration can be made in order to improve its properties.

1.1 Motivation

Because of its use as a way to rapidly produce prototypes, Additive Manufacturing (AM) has had a significant impact in research and development of improved sandwich structures. As studies using this technology are now becoming more relevant, AM is an attractive method to apply to the development of structural design, such as lattice structures. The fused deposition modeling (FDM), also denoted by fused filament fabrication (FFF), is part of the Material Extrusion category of AM, as stated by the terminology of ASTM [1]. Besides being the most common AM manufacturing method, FDM is the method available at Lab2ProD at Instituto Superior Técnico in Lisbon. As such, it was the chosen manufacturing method for this study.

1.2 Background

Sandwich panels are structures that due to their properties and great variety can be manufactured in different ways to be used in a wide variety of applications. They are divided in two main groups according to the topology of the core. These groups are 2D honeycombs and 3D foams.

Studies developed in Lab2ProD showed promising results when producing sandwich panels with 3D lattice structures instead of the of the 2D honeycombs. Various geometries found in atomic crystalline structures were tested and a Body and Face Centered geometry with z-struts (BFCZ) was considered the most satisfactory unit cell for the core

1.3 Objectives

The objective of this thesis is to design, produce and analyse the stiffness, strength and energy absorption of nine different sandwich panels with the BFCZ unit cell in the core geometry. The differences between these nine panels will be the strut radius and relative geometry of the basic unit cell. The values used for the radius of the struts were 0.8 mm, 0.92 mm and 1.1 mm and the relative density values used were 0.25, 0.3 and 0.35. To accomplish this, the following steps needed to be achieved:

1. Design nine unit cells beam structures (panels) with different combinations of strut radius and relative density of the unit cell but all with approximately similar global dimensions;
2. Carry out a Finite Element Analysis (FEA) to each one of the sandwich panels subjected to a three-point bending loading;
3. Produce all the sandwich panels using the FDM process in a commercial 3D printing machine;
4. Experimental testing of all the nine panels subjected to a three-point bending loading;
5. Compare the nine lattice structures in terms of load-displacement curves, rigidity and absorbed energy with the benchmark honeycomb structure;
6. Compare the results of FEA with the experimental tests.

1.4 Thesis Outline

The present thesis is organized as follows:

- Chapter 1 - Introduction
- Chapter 2 - Literature Review
- Chapter 3 - Materials and Methods
- Chapter 4 - Results
- Chapter 5 - Conclusions

Chapter 2

Literature review

2.1 Sandwich Panels

Sandwich panels are a type of composite materials which are made of 3 components. The top and bottom layer are thin solid face-sheets made of the same material with high flexural stiffness. The middle layer, more commonly known as the core, is a lightweight material which is thicker than the other layers and has a high bending and buckling resistance which results in an excellent shear stiffness and energy absorption capability [2]. An example of this type of panels is presented in figure 2.1.

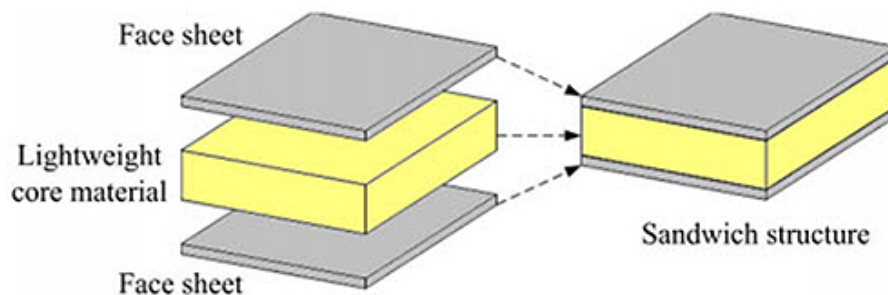


Figure 2.1: Components of a sandwich panel [3]

Because of the combination of these two types of materials, the sandwich panels have a high strength, high energy absorption, high stiffness but a low density. This set of properties means that these types of panels can be used in a wide array of applications, such as helmets used in sports and much larger applications in the automobile and aeronautic industries [4].

The properties of the sandwich panel are derived not only from the properties of the material that make the panel but also from the geometrical parameters and the topology used. In particular, the core is much more important than the other layers because the lower the weight of the core, the lower the weight of the overall structure, maintaining, of course, the functionalities of the panel [2, 5].

2.2 Core - Materials and Analysis

The materials used in the core of these panels can be divided in two major groups depending on their topology. The first group are two-dimensional structures. The most important and commonly used structure of these two-dimensional structures is the honeycomb [6]. The honeycomb is a periodic structure which is normally made of aluminium or polymers. The second group is three-dimensional structures, such as foams and lattices, which are also known as cellular solids [6].

2.2.1 Two Dimensional Structures - Honeycomb Structures

The honeycomb structure, which can be seen in figure 2.2, is the most commonly used in sandwich panels. Since the 1940s that honeycombs have been made from a variety of materials, as just about any thin flat plate material can be used to manufacture a honeycomb structure. Some of the more common materials used are aluminium, stainless steel and titanium as metallic materials; fiberglass, Nomex, Kraft paper and carbon fabric as non-metallic materials. Cores made in a carbon fabric have been used in sandwich since the end of the XX century and achieve a shear modulus as high as the aluminium honeycomb core [7].

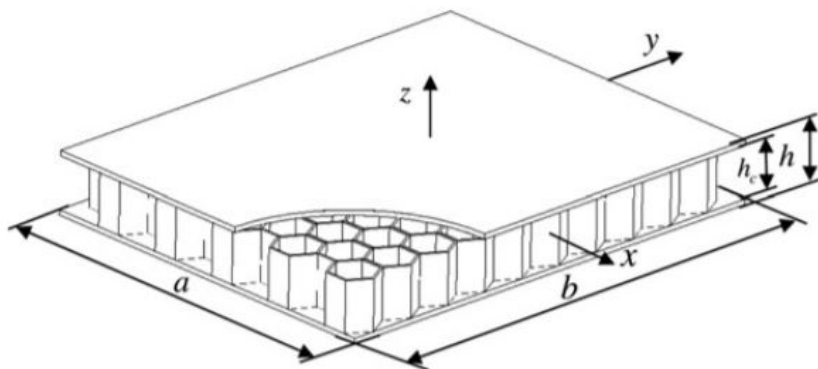


Figure 2.2: Honeycomb sandwich panel [8]

There are five ways of manufacturing a honeycomb panel: adhesive bonding, resistance welding, brazing, diffusion bonding and thermal fusion which all differ depending on how the nodes are attached. The most common of these methods by far is adhesive bonding, which is used in about 95% of the honeycomb cores [7]. The resistance welding, brazing and diffusion bonding are methods only used in cores that are exposed to high temperatures. These methods are much more expensive than adhesive bonding, but can withstand temperatures up to 400 degrees Celsius. Using the adhesive bonding method, there are two processes that can be used, the expansion process and the corrugation process [7].

The expansion process is the most efficient process, so almost all of the cores manufactured using the adhesive bonding are made through this process. In this process, a coating, used to improve the resistance to corrosion, is applied to the sheets of material and the adhesive lines are printed. The sheets are then subjected to an initial cut, stacked and the adhesive is cured at an elevated temperature.

The sheets are then trimmed to the desired final size and expanded. The whole process is presented in figure 2.3. If the material is metallic, the sheets will yield plastically at the node-free walls and maintain the expanded shape. If the material is non-metallic, it will not maintain its shape after being expanded and must be held in a rack to maintain the expanded geometry. Then the non-metallic cores are dipped in a liquid resin and cured in an oven, with the exception of most papers cores which will retain the expanded form [7].

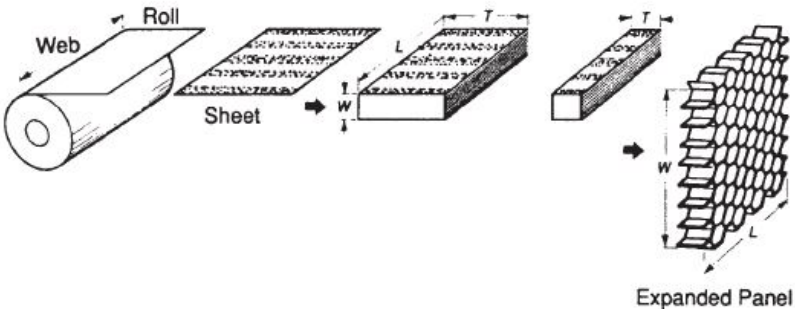


Figure 2.3: Manufacturing of a honeycomb core using adhesive bonding and the expansion process [7]

The corrugation method, shown in figure 2.4, is the original method to manufacture a honeycomb core. In this process, the sheets are first corrugated and then the adhesive is applied to the nodes. The corrugated sheets are then stacked and cured in an oven. Because only light pressure can be applied to the block of stacked corrugated sheets, the adhesive node (10% of the total weight) is much thicker than the one in the expansion process (1% of the total weight). In some cases, if the core is made of a non-metallic material, it must be dipped in resin to achieve the optimum resin-to-reinforcement ratio [7].

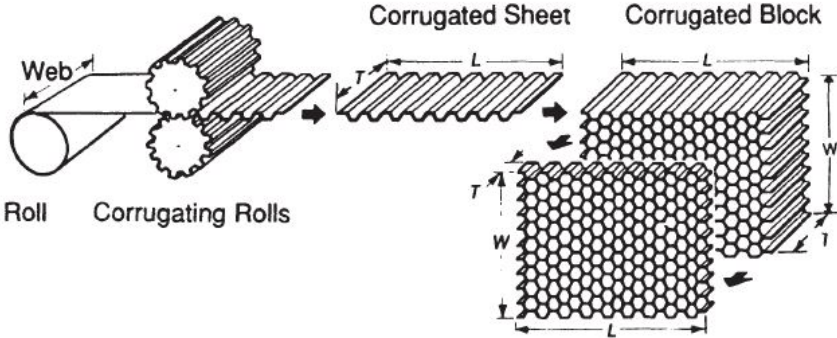


Figure 2.4: Manufacturing of a honeycomb core using adhesive bonding and the corrugation method [7]

Because of the properties of this structure, various studies have been made to validate its usage in multiple and very different areas. There are various types of studies on impact from low velocity impact [9] to hypervelocity impact [10] ; studies under different conditions such as in water [11], high temperatures [12] or under air blast [13]; also stress tests with different focuses such as elastic-viscoplastic behaviour [14], failure modes maps [15], indentation failure [16], predicting failure on damaged panels [17] and predicting failure on panels under bending [18].

2.2.2 Three Dimensional Structures

A three dimensional structure consists in a connected array of struts or plates that is characterized by a typical cell with certain symmetry elements. An example of a typical three dimensional cellular structure can be seen in figure 2.5.

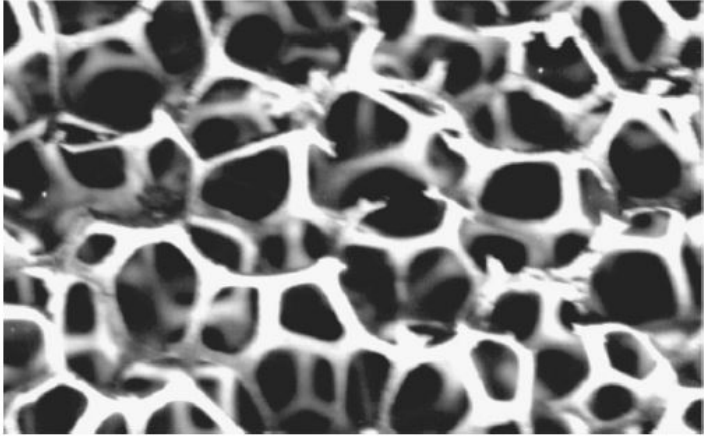


Figure 2.5: Typical cellular structure [6]

These three dimensional structures can be manufactured with three different types of material: ceramics, metals and polymers. Of these three, polymers are by far the most studied, although more recently some studies have been made on the others two types [19].

Despite the three different types of structure, the principles that will influence their properties are the same for all three. The factors with the most importance to define the properties are the properties of the base solid, the topology and shape of the cell edges and faces, and the relative density of the cell [4]. Some of the more important properties of the individual material which constitute these structures are stiffness, strength, thermal conductivity and diffusivity, electrical resistivity among many others. Figure 2.6 provides a better understanding of how the properties of a cellular material are obtained [6].

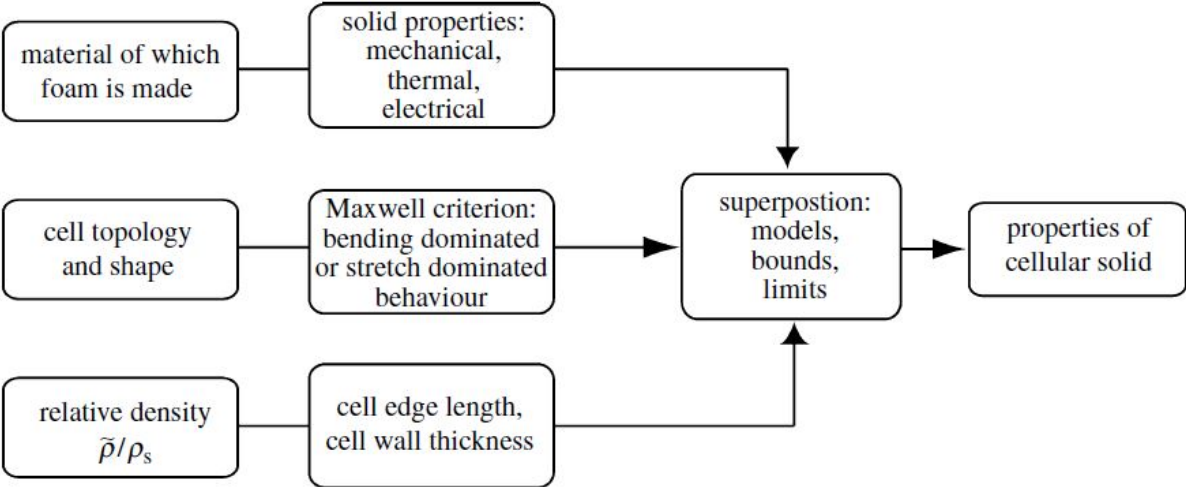


Figure 2.6: Properties of a cellular material [6]

This extension or improvement of the properties is made using struts. In structural engineering terms,

a lattice truss is a set of joints which are connected in order to create stiff, load-bearing structures using the minimum material possible which results in a light weight. Most of the time, the struts are connected in a way that make the structure symmetrical [6].

Because of the similarities that exists between these material and lattice struts, they can be analysed in two different ways. On the one hand, you can approach them as a material and draw comparisons between it and other conventional isotropic materials. On the other hand, these material can be analyzed as if they were a lattice structure [6].

The figure 2.7 shows an approximation of a cell of a cellular material. It is made up of struts connected at the nodes and surrounded by void space which can be filled by a gas or a liquid.

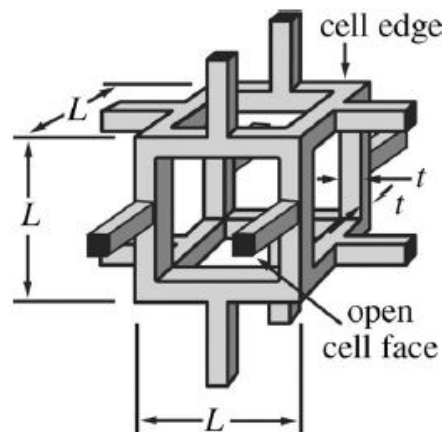


Figure 2.7: Idealization of a cell from a cellular material [6]

Cellular solids are characterized by their relative density, as long as the condition of $t \ll L$ is respected. The relative density is given by

$$\frac{\tilde{\rho}}{\rho_s} \propto \left(\frac{t}{L}\right)^2, \quad (2.1)$$

where t is the thickness of the cell edges, L is the cell size, $\tilde{\rho}$ is the density of the foam and ρ_s is the density of the solid of which the foam it is made.

2.3 Additive Manufacturing

Additive Manufacturing (AM) is a name used to describe all the technologies that create 3D objects by adding consecutive layers of material on top of each other. The main advantage of this method when compared to traditional manufacturing methods, is the flexibility of design [20]. This technology can be used not only with the common polymers, but also with other materials such as metals or even organic materials such as wood, with studies made on the advantages and limitations of using the various materials [21–24].

When it was created, this method was used mainly to produce prototypes. However, with advances in the technology, this method is now used in various fields to meet diverse needs and its usage is growing exponentially. It is used in such diverse fields as aircraft products, dental and medical implants, automobiles and even in fashion products. Due to its high degree of sophistication it can be used to manufacture advanced prototypes, highly customized products, small lots and even replacement parts for additive manufacturing machines [20, 25–27].

There are various methods that constitute the additive manufacturing family, as it can be seen in 2.8, but all of them are assisted by a 3D modelling software such as a **Computer Aided Design (CAD)** software. The products are first designed in this CAD software and then must be converted to a code which in the machine environment translates to the localization of the layers. This conversion from CAD design can be done with dedicated software (such as Ultimaker CURA) or by the manufacturing machines themselves.

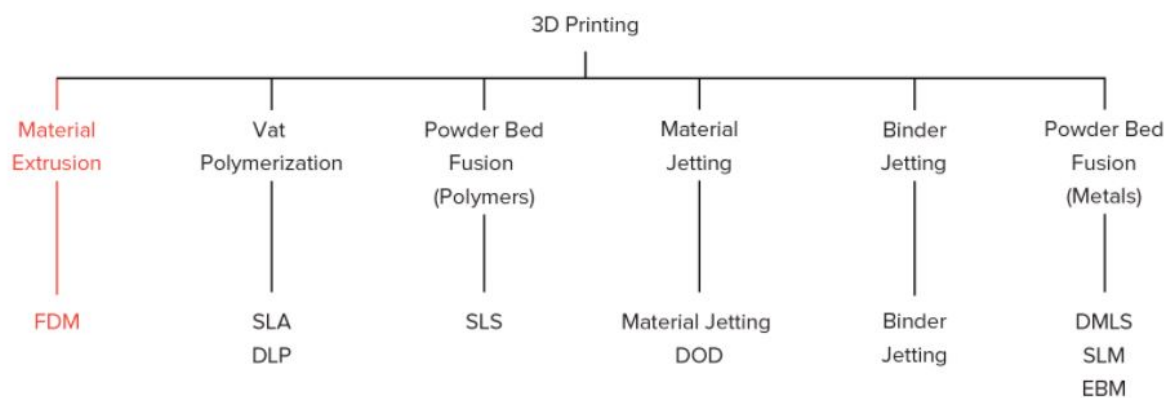


Figure 2.8: The various methods of additive manufacturing [28]

2.4 Fused Deposition Modelling

The most common and widely used method of the AM methods is the **Fused Deposition Modeling (FDM)**, which can also be known as Fused Filament Fabrication (FFF). It makes the bulk of all the printers sold globally and so it has become the method that the average person associates with 3D printing [25].

This method is part of the material extrusion method family. In this method, melted material is deposited in a pre-determined path layer-by-layer, as it can be seen in figure 2.9. This material will then cool down and solidify and so creating a solid piece [28].

2.4.1 FDM Printing Process

The process to manufacture a part using FDM starts with the design of the part. The design is done with the support of a CAD software. Although this process may feel very straightforward, the designer has to consider the many different characteristics that this process has when compared to more traditional

manufacturing processes and even to other AM processes. These characteristics will be explored and explained later in this thesis.

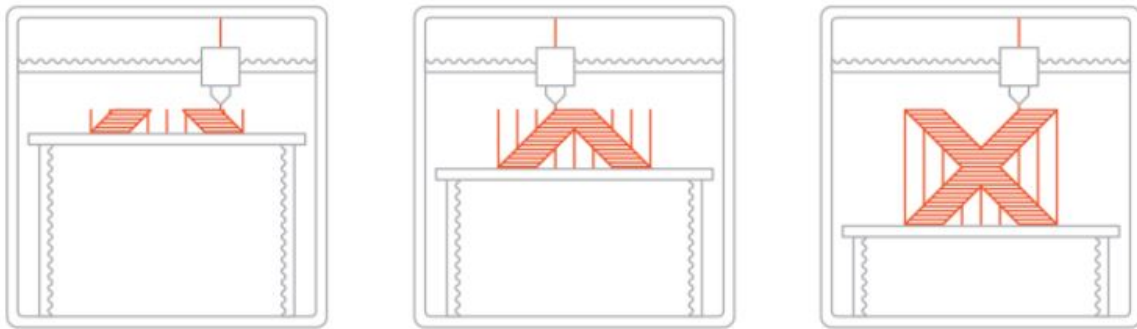


Figure 2.9: The FDM printing process [28]

Once the CAD part is properly designed it must be converted and saved into a STL (**S**tandard **T**riangle **L**anguage) file, which will represent the part with a stereolithography format. This means that the surfaces of the part will be converted into a mesh of various small triangles that will form individual surfaces. The characteristics of these triangles will result in smoother or more coarse approximation, as it can be seen in the figure 2.10. If we use few and big triangles the model will be very coarse, but if we use many and smaller triangles the approximation will be much smoother [29].

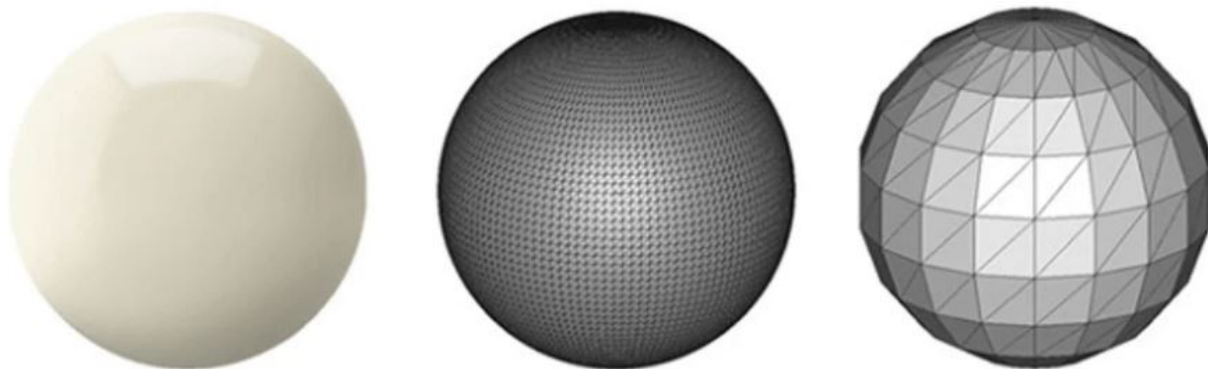


Figure 2.10: Approximation of spherical surface using stereolithography with different degrees of approximation [29]

Now that the part is saved in a STL file format, it must be processed in a slicer program. This program will take the STL file and in conjunction with the print specifications introduced by the user will create the path for the extruder head to follow. The specifications include part orientation, layer height, type and dimensions of the material, infill percentage, printing speed, conditions of the adhesion to the build plate, cooling and support in case of overhang. Figure 2.11 represents the slicer program used in this thesis.

Then, this program saves all this information in G-Code format. G-Code is a **N**umerical **C**ontrol (NC) programming language which is used by automated machine tools, such as CNC machines and 3D printers.

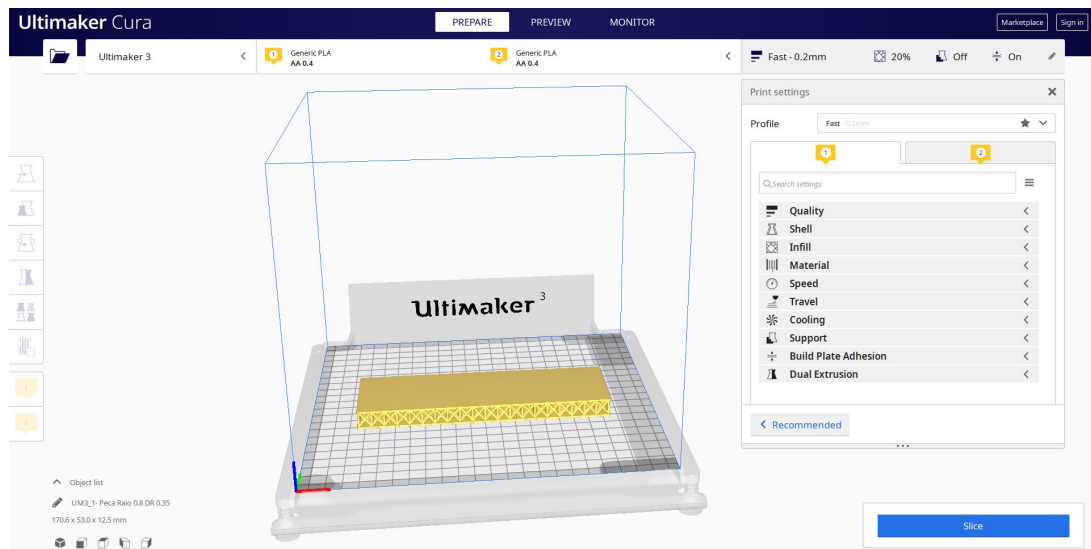


Figure 2.11: Ultimaker Cura, the slicer program used for this research

With the G-Code created, one would think that at this stage we are ready to print. But in fact, the printer also needs to be prepared before printing. The main preparations are setting up the material and level the build plate, but there are also other important things to check such as if the correct printer heads are installed. The thermoplastic material used in FDM printing comes in spools and it must be placed in the spool holder which can be separated or an integral part of the printer. The user inserts the information in the printer of what type of material is about to be loaded and only then can the material be fed into the printer. To insert a new spool, the tip is loaded into the drive gear, which is the part that unwinds the spool and pulls the material into the extrusion head. Once the material reaches the extrusion head, a small piece of material is immediately extruded to ensure that all is correct. The levelling of the build plate is an extremely important part of the printing process because it ensures that the printer head is perpendicular to the table.

These processes can vary from printer to printer but due to the advances and existence of more sophisticated printers, these normally can guide the user through these processes. Some even perform these checks automatically prior to every single print.

Now that everything is ready, we can start to print. To do this, we load the G-Code file into the print. The printer will start by heating the extrusion head and the build plate to desired temperatures in order to melt the filament once it gets to the nozzle. Once this temperature is reached, the print starts. Although the existence other types of FDM printers that use polar coordinates, the one used in this study used cartesian coordinates, so only the movements of this type of printer will be explained. A cartesian FDM printer works with a 3-axis system X, Y and Z but the extrusion head can only move in the X and Y axis. The movements performed in the Z axis are all done by the build plate, as it can be seen in figure 2.12. So, at the beginning of the print, the build plate goes to its maximum height in order to print the first layer. The extrusion deposits the material as regulated by the G-Code file, where it quickly cools and solidifies. Often this cooling is aided by fans which are mounted in the extrusion head. After all necessary passes by the extrusion head are performed that layer is finished. The build plate will move down and a new

layer starts to be deposited. Once all layers are deposited, the process is finished.

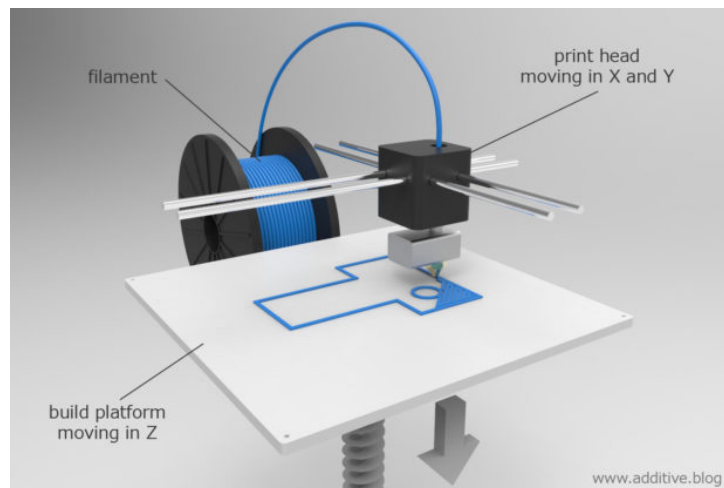


Figure 2.12: Movements of the printer head and of the build plane [30]

2.4.2 FDM Parameters

When a designer makes a part to be produced using the FDM method, he must be aware of some parameters that are specific to this method and design the part accordingly. This is especially true if the designer and the operator of the printer are not the same person [28].

Printer Parameters

There are various parameters regarding each printer, such as temperatures of nozzle and build plate, build speed, usage or not of a cooling fan, among others. These are normally set during the splicing phase and because they are more related with the printer than with the part, are chosen by the operator.

The printer parameters that are of great importance to the designer are the build size and the layer height. The build size is the space that a 3D printer has available to build a part, meaning that it is equivalent to the maximum size of a part that can be built using that printer. These dimensions are usually 200 x 200 x 200 mm for common desktop printers. If a designer wants to build a part larger than the available build size, he must take into consideration and design into the parts appropriate grooves and joints so that the parts can be assembled later. The layer height normally used in FDM printing varies between 50 and 400 microns and it will affect the mechanical properties of parts, the final quality of the print and the printing time. A smaller value of layer height will result in smoother parts and better representation of curved geometries, but it will result in higher production times and production costs. It is an important trade off that the designer must decide considering the final usage of the part.

Infill and Shell Thickness

When printing large solid parts using FDM, in order to reduce the printing time and to save material, solid geometries can be replaced by less dense structures. To do so, the outer perimeter is traced with

several passes, which is the shell, and the interior is substituted with a structure, which is the infill. This infill can have many different configurations and even vary its percentage between different planes of the same part. Figure 2.13 shows a part printed with many different infills. The shell thickness and the percentage and geometry of the infill are decided by the designer. Higher values of any of shell thickness and infill percentage will result in higher printing times and more material used but also in higher strength of the part. Desktop printers normally use an infill of 25% and a shell thickness of 1mm, which is a good compromise between strength and manufacturing time [31].

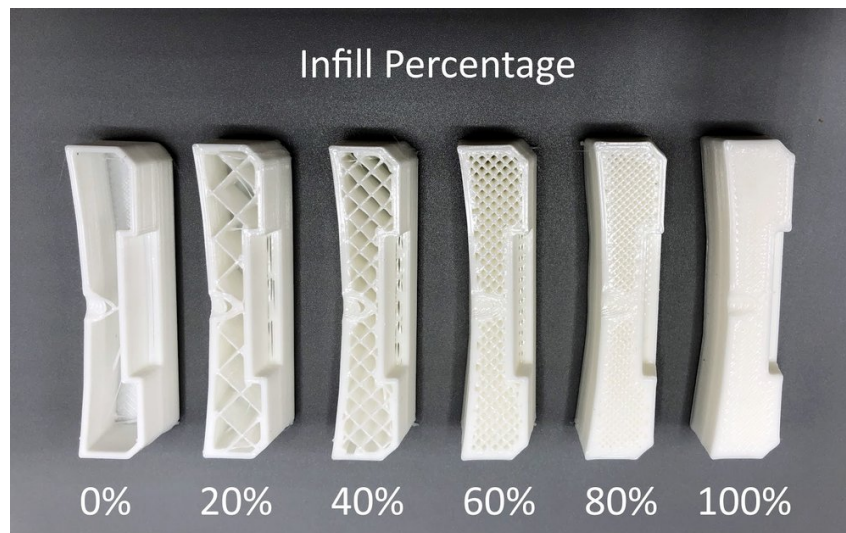


Figure 2.13: Part printed with the same shell thickness but different percentages of infill [31]

Layer Adhesion

Layer adhesion assures that the layers are well connected to each other and so preventing layer separation. When the molten material is extruded out of the nozzle, it is pressed against the layer below. The high temperature and pressure exerted on the layer that had already solidified re-melts the old layer and the new layer will be able to bond with the previous. Because of the pressure exerted, the pre-existing layer will be deformed into an oval, which means that FDM parts will always have a wavy surface, independently of the layer height. Because of this deformation, if the part has a precision feature, such as a thread or small hole, it might need post processing [32].

All FDM parts are being built with layers in the Z direction which means there is a discontinuity between layers. This means that the bonding strength between layers will be lower than the base strength of the material which results in parts that are anisotropic, as the strength in the Z direction will always be smaller than in the XY-plane. Studies made in parts of ABS with an infill of 50% where the printing orientation was changed (parts were printed horizontally and vertically), showed that the tensile strength in the X and Y direction is 4 times greater than in the Z direction [28]. The same study also showed that elongation in the X and Y directions is 10 times greater than elongation in the Z direction [28]. So, to avoid failure of the part, it is important that the orientation of the part regarding the stresses that it will suffer is taken into account. A more descriptive explanation can be seen in figure 2.14.

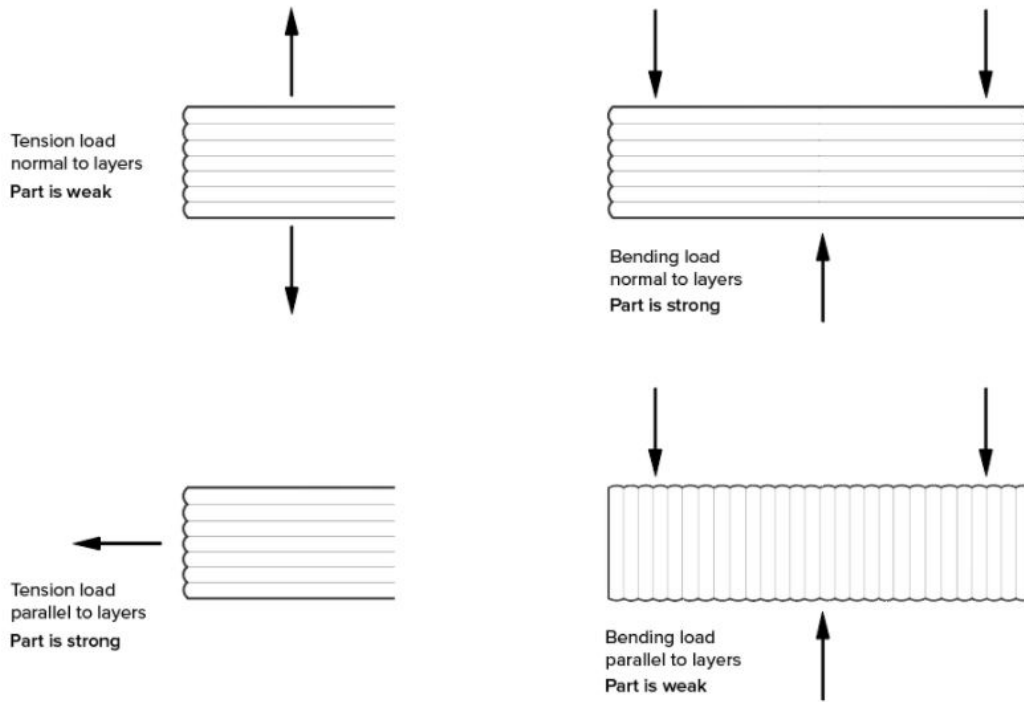


Figure 2.14: Building direction considering the stresses applied [32]

Overhangs, Bridges and Support Structures

Overhangs and bridges are parts of layers which do not have any material below it. If the part of the layer connects two previous layers, it is considered a bridge. However, if part of the layer does not connect two previous layers, meaning that when it ends it is not touching the end of a previous layer, it is an overhang. Using the letters Y, H and T in conjunction with the figure 2.15, helps to understand these concepts.



Figure 2.15: Overhangs and bridges represented by the letters Y, H and T [33]

Depending on the parts, to build parts with overhangs and bridges, a support structure may or may not be needed.

Regarding the overhangs, the part will need a support structure if the overhang makes an angle greater than 45-degrees with the vertical plane (or smaller than 45-degrees with the horizontal plane). This is known as the 45 degrees rule. This happens because there is always a tiny horizontal offset between layers, so all the layers are stacked with a small offset between each other. Because of this fact, the printer can print overhangs that do not tilt too much from the vertical and 45 degrees is generally considered the critical angle. Figure 2.16 shows when support is and is not needed when using overhangs [33].

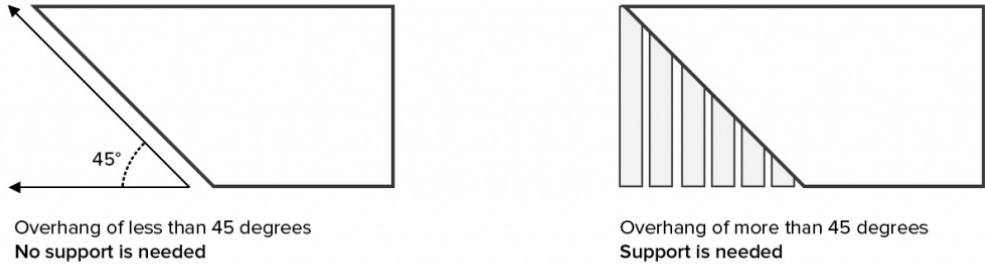


Figure 2.16: Overhangs with and without the need of support which depends on the angle with the horizontal. In the first figure, the angle with the horizontal is 45 degrees, so there is no need of support. In the second figure, the angle with the horizontal is smaller than 45 degrees so support is needed. [34]

Regarding the bridge, the part will require support if the bridge has more than 5 mm of length. For values smaller than 5 mm, the printer uses a technique called bridging, where it stretches the hot material for short distances and with minimal sagging. However, for values larger than 5mm this technique is no longer valid. Figure 2.17 shows a print that failed due to sagging and lack of support and the same print done with support.

Support structures are always undesirable when producing a 3D print because it means that it is necessary to use more material and that the printing time will be longer. It is always preferable that the designer divides the part into two or more smaller parts that do not need support structures in their production, as it can be seen in figure 2.18.



Figure 2.17: Failure caused by printing the letter T without support [33]

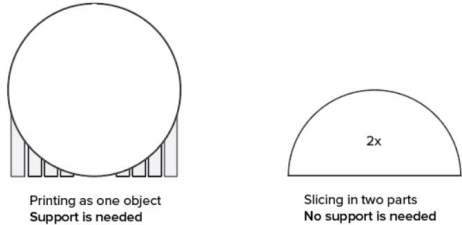


Figure 2.18: Dividing a part that needs a support structure into two that do not need support structures. [32]

Materials

There are various materials available for use in the FDM process. These can range from common thermoplastics like the polylactic acid (PLA) to high performance thermoplastics like polyethyleneimine (PEI). A diagram of the more commonly used materials is shown in figure 2.19. The material used will determine not only the mechanical properties of the part, but also the price and duration of the print [35].

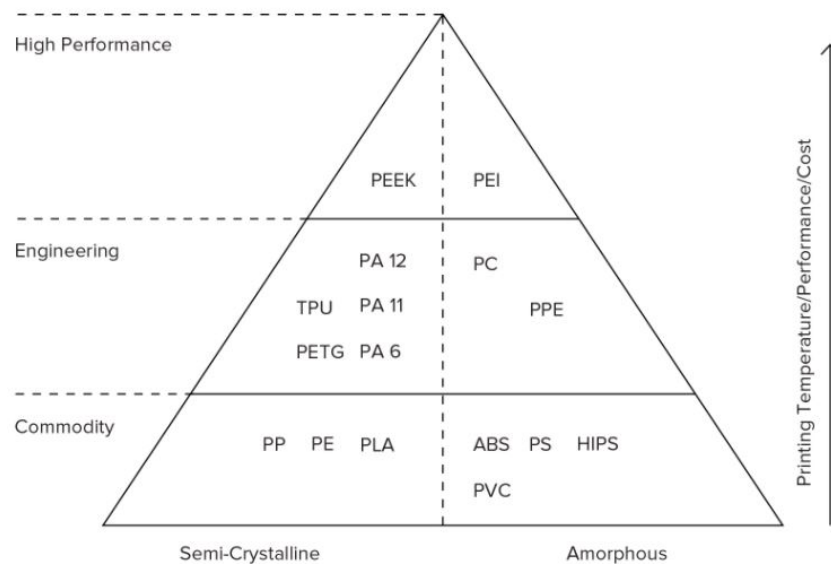


Figure 2.19: Diagram of materials used in FDM. [28]

Of all the materials presented in the diagram above, the most commonly used are the Acrylonitrile Butadiene Styrene (ABS) and the Polylactic Acid (PLA) and as such there are studies made on their influence on the final prints [23, 24]. Because of their common use, a comparison between these two materials is presented in table 2.1.

Table 2.1: Properties of ABS and PLA [35]

Properties	ABS	PLA
Tensile Strength (MPa)	27	37
Elongation	3.5% - 50%	6%
Flexural Modulus (GPa)	2.1-7.6	4
Density (g/cm^3)	1-1.4	1.3
Melting Point ($^{\circ}C$)	N/A (amorphous)	173
Biodegradable	No	Yes, under correct conditions
Glass Transition Temperature ($^{\circ}C$)	105	60
Spool Price (1kg, 1.75mm, black, \$USD)	21.99	22.99
Common Products	LEGO, Electronic housings	Cups, plastic bags

ABS is a common thermoplastic that is and was commonly used in the injection molding industry even before the invention of FDM methods. PLA is a semi-biodegradable thermoplastic derived from renewable resources such as corn starch or sugarcane.

Comparing some of the properties shown in the table, we can infer which material will have a better behaviour depending on the situation.

- **Part Accuracy** - Both materials are good to print a dimensionally accurate part, but because the PLA has a lower printing temperature it is less likely to warp. It can also print sharp corners better than the ABS.
- **Strength** - Both materials have adequate tensile strengths for prototype applications but ABS has improved ductility over the PLA.
- **Heat Resistance** - ABS has a much higher glass transition temperature so it is better suited to applications where heat is a factor.

2.4.3 FDM Printing Defects

In this section we will review some of the more common defects that appear during FDM printing and also how to prevent them, if possible [36].

Warping

Warping is the most common defect in FDM and so every designer must take this defect into mind when designing parts for FDM printing. Warping is caused by the solidification of the thermoplastic during the cooling phase, which will provoke its dimensions to decrease. But because different sections cool down at different rates, the dimensions will also change at different speeds. This differential in cooling will result in the formation of internal stresses that will pull the underlying layers upwards. This will cause the part to warp upwards, as shown in figure 2.20.

There are various techniques that a designer can use to prevent warping during the printing of the part. Some design features are more prone to warping, for example large flat areas should be avoided and sharp corners should be replaced by fillets. Thin protruding features are also prone to warping. If they cannot be avoided some sacrificial material should be added between the feature and the build platform. Finally, different materials are more prone to warping than others, such as materials with a high coefficient of thermal expansion like the ABS. From the printer side, the warping can be prevented by correctly regulating the temperatures of the build plate and of the surroundings. Another way to prevent this problem is to increase the adhesion between the part and the build plate.

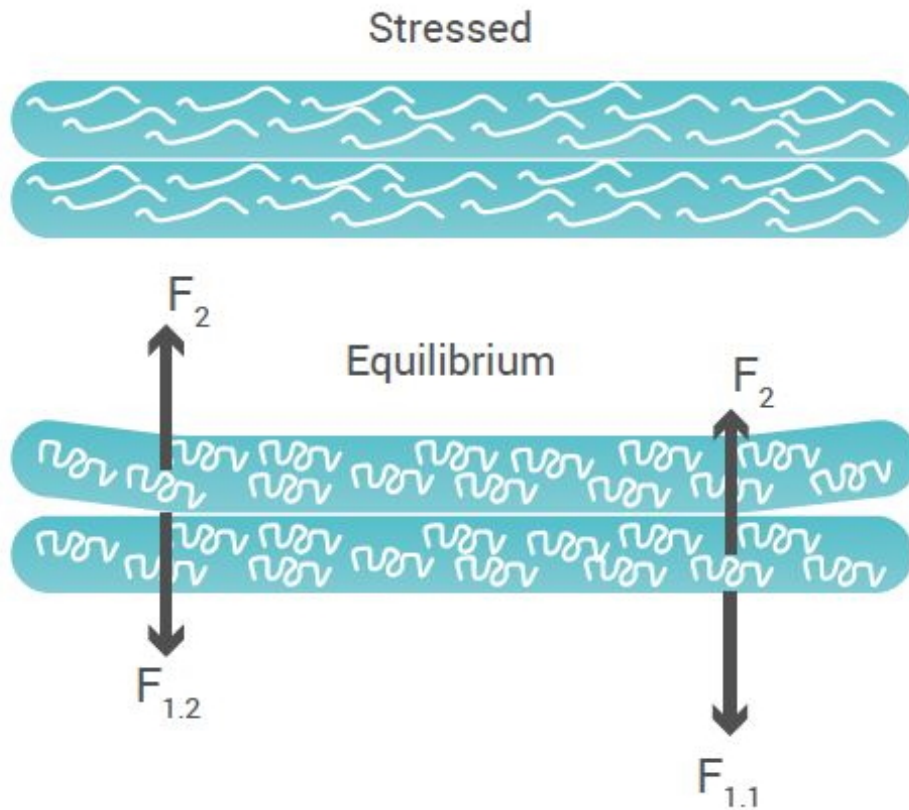


Figure 2.20: Edge Warping of an FDM part caused by the existing stresses in the layers [37]

Bad adhesion of the first layer to the Build Plane

Bad adhesion or total lack of adhesion between the first layer and the printing bed will result in a quickly decaying lack of quality of the print. This is because the other layers will not have a sound foundation to solidify on and so the problems will exacerbate. One example of this type of failure is shown in figure 2.21. This problem can be caused by various factors so each case will require a different solution.

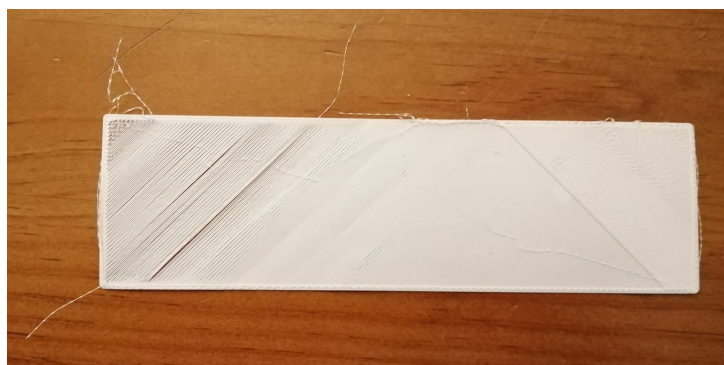


Figure 2.21: Example of print fail due to bad adhesion

The problem may be caused by an unlevelled build platform which can be addressed by performing a manual levelling of the platform; by the nozzle being too far from the build plane which can be corrected by adjusting the Z-axis offset; excessive printing speed; bad adjustment of the temperatures of the extruder and build plate; defects and/or debris in the build plate such as remains of glues; lack of

necessary brim/raft, which are extra rings of material added to the exterior of the first layer to aid the stickage of the first layer to the build plate.

Stringing or Oozing

Stringing or Oozing occurs when small strings of material are left behind on the printed part. This normally happens because materials ooze out of the nozzle while it moves to a new location. Figure 2.22 presents an example of stringing.

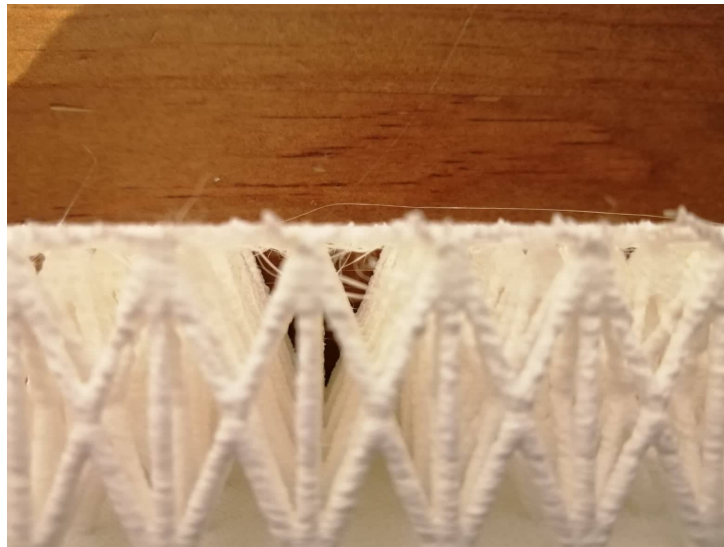


Figure 2.22: Print made for this work that failed.

Fortunately, most printers have an option that prevents this from happening, which is the retraction option. If enabled, after printing a section of the model, the filament will be pulled backward and when it is time to restart printing, the filament will be pushed back into the nozzle. When using this option, it is important to correctly set the retraction distance and retraction speed. If, even with the retraction option active the problem persists, there are other options that help prevent the stringing. If the extruder temperature is too high, stringing is likely to occur. Because this problem occurs more when the nozzle moves over open spaces, long movements over these open spaces should be avoided. Finally, an increase in the movement speed can also help to reduce the problem.

Grinding Filament

The majority of 3D printers has a small drive gear that grabs the filament and traps it against a bearing. This drive gear has sharp teeth that allow it to push the filament forward or backwards, depending on what is needed. But in some cases, the filament cannot move but the drive gears will keep moving. This will cause the drive gear to grind the filament and if it grinds away too much material, eventually there is nothing left for the teeth of the drive gear to grab on to. One example of a ground filament is presented in figure 2.23. This will result in the filament not moving and because of this the print will fail because no material reaches the nozzle. This problem can be detected by noticing small plastic shavings near the extruder motor and because the extruder motor is spinning but the filament is not moving.



Figure 2.23: Filament that was ground during the manufacture of specimens

This problem can be caused by incorrect retraction settings, which may be too aggressive. Another factor that can cause this problem is having a too low extruder temperature which can cause a deficient flow of thermoplastic. Decreasing the printing speed in order to reduce the drive gear speed and so prevent grinding can also be useful. Finally, if the problem persists after these changes, there may be clogging in the nozzle.

2.5 Behaviour of a cell in a Cellular Material

According to the studies made by Ashby [6], a cellular material has a bending-dominated deformation. This is because the stiffness and overall strength of the cellular material is much lower than a stretch-dominated material with the same relative density. So, analysis of the behaviour of a cell will only be presented under bending-dominated deformation.

The figure 2.24 shows the compressive stress-strain of a bending-dominated lattice. Because the material is linear elastic, it deforms linearly, with modulus \tilde{E} , until its elastic limit. At that point, the material either yields plastically, buckles or fractures. The lattice continues to collapse at an almost constant pressure also known as the plateau stress, $\tilde{\sigma}_{pl}$. This continues until the opposite sides of the cell start to impinge, when the stress starts to rise rapidly and the densification strain, $\tilde{\varepsilon}_d$. After this, the collapse starts with 3 collapse mechanisms possibly happening and the one which requires the least amount of stress dominates.

Observing the figure 2.25, the displacement δ can be estimated. The force F applied on the cell edges generates the stress $\sigma \propto F/L^2$. So, a strut with length L which is loaded at its mid-point by the force F will have a displacement δ given by

$$\sigma \propto \frac{FL^3}{E_s I}, \quad (2.2)$$

where E_s is the modulus of the material from which the strut is made and $I = t^4/12$ is the second moment of area of the cross-section $t \times t$. The whole cell suffers a compressive strain of $\varepsilon \propto 2\delta/L$.

Assembling all the results into the formula of the modulus $\tilde{E} = \sigma/\varepsilon$, we arrive at the conclusion that

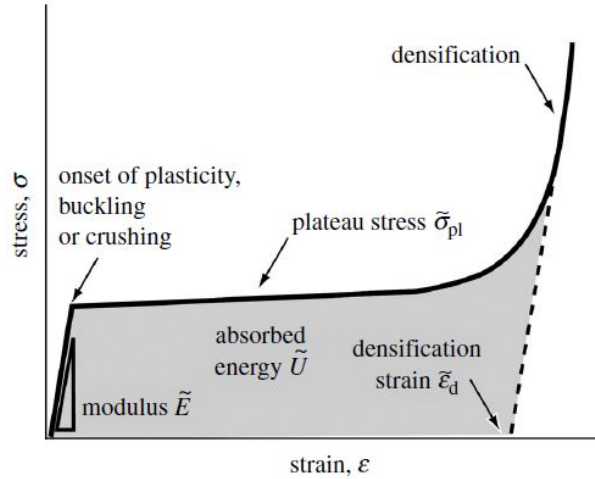


Figure 2.24: Compressive stress-strain behaviour of a bending-dominated lattice [6]

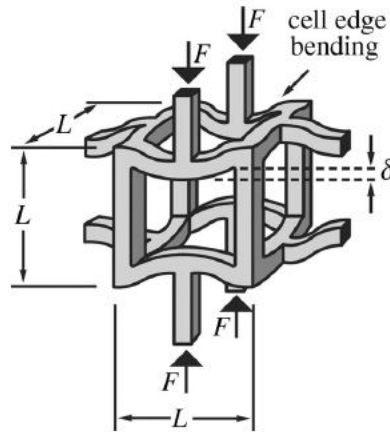


Figure 2.25: Bending-dominated lattice under stress [6]

$$\frac{\tilde{E}}{E_s} \propto \left(\frac{\tilde{\rho}}{\rho_s} \right)^2. \quad (2.3)$$

This result is typical of a lattice with bending-dominated behaviour. Because $\tilde{E} = E_s$ and $\tilde{\rho} = \rho_s$, the constant of proportionality is expected to be close to the unity.

2.6 Meta-materials

The advances in the areas of material manipulation, whether through research, development of new techniques or the creation of new ones lead to the creation of Meta-materials. A meta-material is a material that was modified by changing its properties in order to achieve properties that are not available in natural materials or to replicate materials where the processing is difficult.

These meta-materials are created by the repetition of elements made of the base material, which normally have much smaller dimensions than the finished product, as shown in figure 2.26. The dimensions of the structure, its orientation and arrangement define the properties of the meta-material. The combination of these variables allows the creation various meta-materials with different properties but all with the same base material.

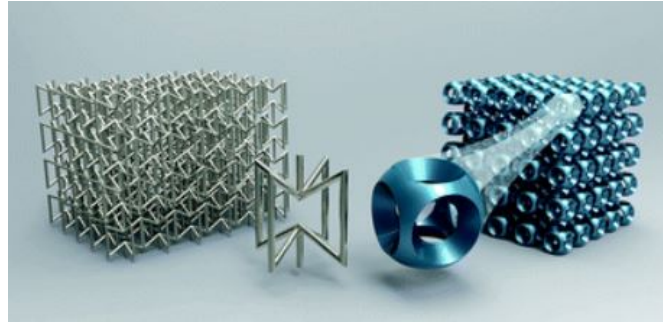


Figure 2.26: Examples of metamaterials [38]

2.6.1 Lattice Structures

A lattice structure is made of the periodic repetition of unit cells that are connected to each other in three dimensions. The unit cells used in lattice structures are mainly struts but they can also be small sheet panels.

The main difference between the cellular structures and the lattice structures is the arrangement of the unit cells. The manufacturing process of the cellular solids does not provide any control over the arrangement of the unit cells which means that the structure is random. But in the case of the lattice structures which are fabricated with AM methods, there is control in the arrangement of the cells.

So, the AM methods are the primary methods for manufacturing these structures. Besides the control over the arrangement of the cells, this method has many well-known advantages over traditional methods. Structures made using AM have, just like the cellular solids, a low weight combined with great properties under stress. It also provides more freedom for the designer of the structure as it can produce more complex shapes. These characteristics allow for control in the arrangement of the cells. Not only that, but this freedom also allows the designer to create structures that tackle specific problems or constraints.

There are many examples where 3D printed lattice structures have been applied to everyday objects with great advantages. In the shoe industry, various brands are applying this technology to their products, either to improve sports performance or to decrease production costs. In the performance side, brands like Nike ® and Reebok ® are applying lattice structures in their shoes which substitute the need for laces or in some cases the whole fabric of the shoe. These design changes lead to lighter shoes and less energy wasted. In other cases, the changes are applied with a focus on decreasing costs. Adidas reports that by using 3D printed soles, lead production decreased from 15-19 months to just 11 months [39]. Pictures of the various shoes mentioned are presented in figure 2.27.



Figure 2.27: Various examples of shoes that use 3D printed lattice structures [40–42]

But shoes are not the only products that use lattice structures in sports. Most recently, 3D printed bicycle saddles, such as the one presented in figure 2.28 have started to be used in high level competition. They are lighter than traditional saddles, which can provide an advantage. Recently, in American football, helmets have been developed with lattice structures. The struts are not connected individually which allows the helmet to deform locally and so absorb contacts with less risk for the players. A diagram of one of these helmets cut in half so that the struts can be seen is presented in figure 2.29.

Outside sports there are various examples where lattice structures are being implemented and used successfully. In architecture and construction, lattice structures are also starting to be used. New companies are being founded that specialize in manufacturing houses and pavilions using large scale 3D printing with lattice structures. Figure 2.30 shows one pavilion created for an architecture fair. As well as constructions, companies are also starting to produce various different types of furniture. Some companies are even starting to reproduce and even create new sculptures to be displayed at art museums [43, 44].

Besides the more ample and varied applications of the lattice structure, there are various studies on the usage of lattice structures as the core of sandwich panels. Various studies were made on the behavior and characteristics of lattice structures regarding the material with which they were constructed. These included studies made on structures manufactured in iron, steel, cobalt, zinc and even the combined materials by using inserts [47–51]. These studies were more focused on the effects that the production process would have on the finished product, as high temperatures were involved when manufacturing the sandwich panels. Some of the studies used **Selective Laser Melting (SLM)**, which is



Figure 2.28: 3D printed bicycle saddle [45]

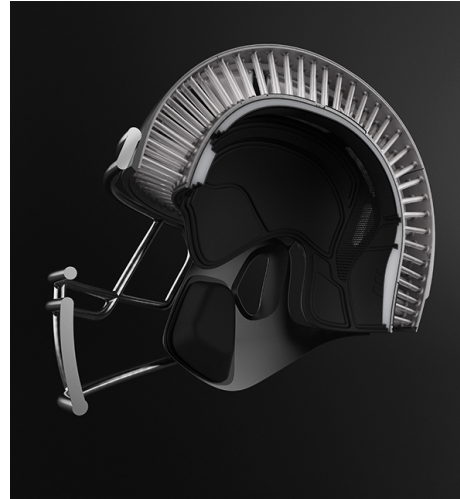


Figure 2.29: American Football helmet which uses 3D printed struts [46]



Figure 2.30: Pavilion made of 3D printed lattice structures [43]

another AM method. Lim and Kang [52] studied the effectiveness of sandwich panels with a core made of piano wires in different geometries. There are also many studies on lattice structures manufactured using the FDM method. Studies made on the various possible geometries, such as atomic geometries, Kagome configuration and Voronoi-based arrays all concluded that with the correct configuration of the core, 3D printed sandwich panels with a core made of lattice structures could equal or even surpass the performance of the common sandwich panels with hexagonal honeycomb core [53–57].

2.6.2 Relative Density

There are various properties that can be inferred for a lattice structure, the most important is, by far, the relative density, $\frac{\rho}{\rho_s}$. The relative density is the density of the unit cell divided by the density of the material from which the unit cell is made of [19].

Gibson [58] demonstrated that the relative density is a volume fraction of the total solid

$$\frac{\rho^*}{\rho_s} = \frac{M_s V_s}{V_T M_s} = \frac{V_s}{V_T} = \text{Volume Fraction of Solid}, \quad (2.4)$$

where M_s is the mass of the structure, V_s is the volume of the structure and V_T is the volume of the total solid.

Gibson also demonstrated that the relative density can be related with the porosity of a solid using

$$\text{Volume Fraction of Solid} = \frac{\rho^*}{\rho_s} = 1 - \text{Porosity} \quad (2.5)$$

Knowing this, it is possible, using the relative density, to grade structures and solids for their porosity. Solids with a low value of relative density (lower than 0,3) are called cellular solids. As the relative density increases the volume of the cell edges and faces get thicker causing the pore volume to decrease. If the relative density is high enough (higher than 0,8) then it is considered that there are only isolated pores in the solid. Figures 2.31 and 2.32 shows examples of the relation between the porosity of the solids and their classification.

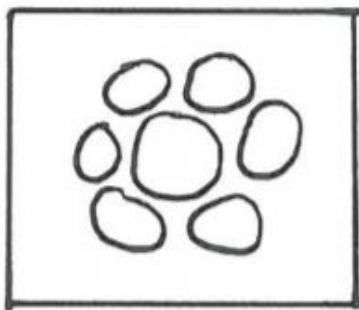


Figure 2.31: High porosity - cellular solid [58]

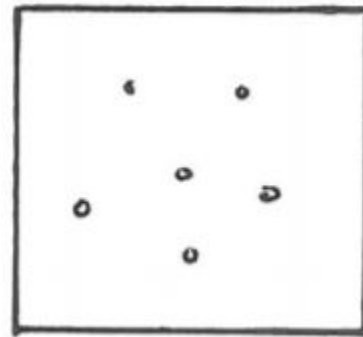


Figure 2.32: Low porosity - isolated pores in solid [58]

2.7 Failure Modes and Mechanisms of Lattice Structures

As mentioned, the relative density of a lattice structure is the most important property of that solid. So, it is not a surprise that this is also the most relevant property of the lattice structure when analysing its failure modes and mechanisms. Since the days when manufacturing these types of structures was made possible many studies have been performed to evaluate their behaviour under various types of loads.

3-Point Bending Load Test

Although there is a wide variety of studies available, the grand majority of them always uses 3-point bending load (3PB) as their means to apply the stress. This is because it is a simple test that, as long as the right measuring equipment is set up, can provide a very wide array of results [59].

In figure 2.33, a sandwich panel is being subjected to a 3PB loading. This sandwich panel has a width of b , the face sheets have a thickness of t and the core has a thickness of c . A 3-point bending consists in having three rollers of radius R , two positioned below the part and one above it. The roller above the part is positioned in the center of the top face sheet and the two rollers below the part are positioned in a manner that the overhang distance to the end of the part, represented by H , is the same. The length span between the two bottom roller is L . In this procedure either the top roller or the two bottom rollers are moved in a way which will provoke stress in the part. It is important to notice that, due to the equilibrium of forces, the force applied by each of the bottom rollers is half of the force applied by the top roller.

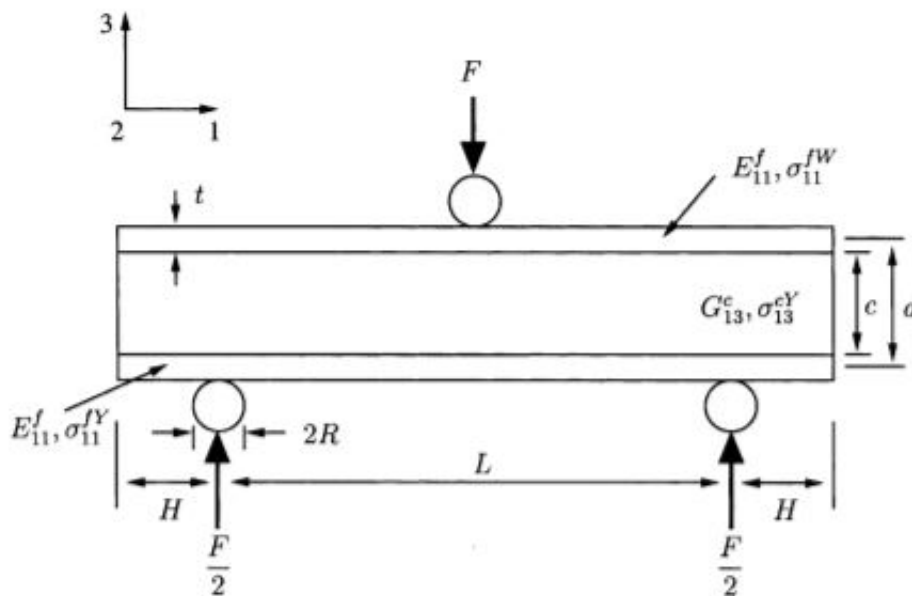


Figure 2.33: Example of a lattice structure under 3PB loading [59]

Failure Modes

Despite the various studies made about this subject, such as Araújo et al. [60] who investigated how the geometry of the core affected the failure, it is important to mention the advances made at the turn of the century by Deshpande and Fleck [59]. They used aluminium and brass tetraedical cores, with and without the use of polystyrene face sheets, to map out the various failure modes, dependent on failure observation and overhang. All the structures used (core, face sheets and their combination) were considered to be plastic solids. From their studies, they were able to discern between five failure modes, which are presented in the figure 2.34.

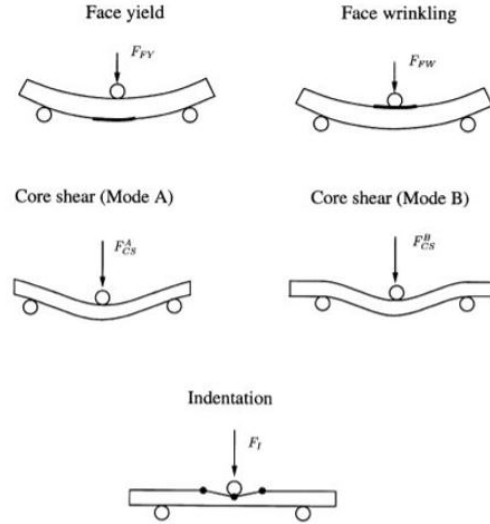


Figure 2.34: Failure modes of a sandwich beam under 3PB loading [59]

According to Hunt and Wadee [61], the relative elastic deflection δ , is given by the sum of the flexural deflection with the shear deflection

$$\delta = \frac{FL^3}{48(EI)_{eq}} + \frac{FL}{4(AG)_{eq}}, \quad (2.6)$$

where the equivalent flexural rigidity $(EI)_{eq}$ is given by

$$(EI)_{eq} = \frac{E_{11}^f btd^2}{2} + \frac{E_{11}^f bt^3}{6} \approx \frac{E_{11}^f btd^2}{2} \quad (2.7)$$

where the Young's modulus E_{11}^f of the face sheets in the 1 direction is defined in figure 2.33. It should also be noted that the contribution from the core to the overall bending stiffness is negligible when compared to contributions from the face sheets.

The equivalent shear rigidity that $(AG)_{eq}$, that appears in the equation 2.6, depends of the shear stiffness of the core and is given by

$$(AG)_{eq} = \frac{bd^2}{c} G_{13}^c, \quad (2.8)$$

where G_{13}^c is the shear modulus of the core in the 1-3 direction, the cross-sectional area A of the core and the mid-planes distance $d = c + t$ of the face sheets, again in the figure 2.33.

Having done a stiffness analysis, we only lack the strength calculation to arrive at a conclusion regarding the theories of the collapse modes. Ashby et al. [62] calculated the upper roller loads in sandwich beams, which were considered to be ideal plastic solids, for the competing failure modes.

Formulae for the collapse strength for each of the failure modes of a specimen under 3PB load are now presented:

- **Face Yield**

In this failure mode, the maximum bending moment on the cross section of the specimen is attained at the top roller. Once the maximum bending moment is high enough for the face sheets to be under a yield strength of σ_{11}^{fY} in the 1 direction, the plastic collapse occurs. The collapse load F_{FY} is

$$F_{FY} = \frac{4bt(c+t)}{L} \sigma_{11}^{fY}. \quad (2.9)$$

It should be noted that the contribution of the plastic bending of the core for this load can be neglected.

- **Face Wrinkling - Buckling**

The top face sheet is subjected to compressive stress and at the top roller, which is where the maximum bending moment of the cross-section is being applied. There may also be elastic or plastic buckling instead of the plastic collapse. The critical wrinkling stress of the top face in the 1 direction σ_{11}^{fW} is dependent of the various buckling modes existent for these kinds of structures. Although a different failure mode from the face yield, the collapse load formula is very similar,

$$F_{FW} = \frac{4bt(c+t)}{L} \sigma_{11}^{fW}. \quad (2.10)$$

- **Core Shear**

The great majority of the shear force applied to a sandwich beam under a 3PB loading is carried by the core. This means that plastic collapse of the core is a possibility. There are two different modes of core shear, which are represented in the figure 2.34, the mode A and mode B.

Mode A represents the core shear over the full length of the beam, $(L + 2H)$. In this mode, there is visible formation of plastic hinges directly beneath the top roller in both skins. The collapse load of mode A is

$$F_{CS}^A = 2 \frac{bt^2}{L} \sigma_{11}^{fY} + 2bc \sigma_{13}^{cY} \left(1 + \frac{2H}{L}\right), \quad (2.11)$$

where σ_{13}^{cY} is the strength of the core in the 1-3 directions.

Mode B only considers the core shear over the span length L . This mode also has formation of plastic hinges but in this case, they are located at the outer loading points in both of the face sheets. The collapse load of mode B is

$$F_{CS}^B = 4 \frac{bt^2}{L} \sigma_{11}^{fY} + 2bc\sigma_{13}^{cY}, \quad (2.12)$$

where σ_{13}^{cY} is the strength of the core in the 1-3 directions.

It is important to notice that in both modes the overhanging regions of the beams remain rigid.

The factor which rules over which deformation mode is the length of the overhang, H . For small overhangs, the collapse is ruled by mode A. Mode B becomes active if the length of the overhang satisfies the following condition:

$$H > \frac{1}{2} \frac{t^2}{c} \frac{\sigma_{11}^{fY}}{\sigma_{13}^{cY}} \quad (2.13)$$

Chapter 3

Materials and Methods

The objective of this work is to analyze the effect of variation of radius and relative density in the mechanical properties of a composite panel by carrying out three-point bending experimental tests (3PB). Finite Element Analysis (FEA) was also used to compare the numerical and experimental results. To study the effects of the variation of the said parameters, three values of radius and three values of relative density were chosen. This means that a total of nine lattice structures were designed in order to have all the combinations of radius and relative density.

3.1 Design

3.1.1 Material

The material used to manufacture the specimens was Poly-lactic Neutral Acid PLA-N, which is a variant of the Poly-lactic Acid or PLA. One of the spools used is presented in figure 3.1. The PLA is extensively researched and is one of the most commonly used biodegradable polymers.

PLA was first synthesized in 1932 by Wallace Carothers. At that time, it was one of the most promising biopolymers because its monomers can not only be produced from non-toxic renewable feedstock but also from the fermentation of sugars from sugarcane or corn starch. This can only happen because this monomer is a naturally occurring organic acid. Today, it has a wide range of applications such as medical applications, food packaging and large industrial scale [63].



Figure 3.1: PLA-N spool used in this work [64]

The PLA-N used in this thesis was engineered to further improve the capacities of the base material, which is the PLA and so it retains its capacity to be used in AM methods. PLA-N has 27,5% more torsional strength and 12,5% more flexural strength (for the spool used in this case) than the PLA [65].

The properties of the PLA-N material shown below in table 3.1 are provided by Filkemp which is the manufacturer of the spools used in this work [66].

Table 3.1: PLA-N properties of the material used [66]

Property	Value
Young's Modulus (MPa)	2400 ± 40
Tensile Stress at Yield (MPa)	35.2 ± 0.8
Tensile Stress at Break (MPa)	35.2 ± 3
Elongation at Yield (%)	2 ± 0
Elongation at Break (%)	6 ± 2
Flexural Strength (MPa)	68 ± 5
Flexural Modulus (MPa)	68 ± 5

3.1.2 Specimens Design

For the purpose of this study, a total of nine unit cells, which will translate to nine sandwich panels, were designed. All the designs were made using the **Computer Aided Design (CAD)** software Solidworks 2018 ®. The unit cell and sandwich panels used for the specimens in this study were based on atomic crystalline structures with cubic arrangements. Monteiro et al. [5] studied the influence of the core geometry in the overall performance of the structures. He analysed various geometries, which are presented in figure 3.2, based on the crystalline structures found in atomic arrangements.

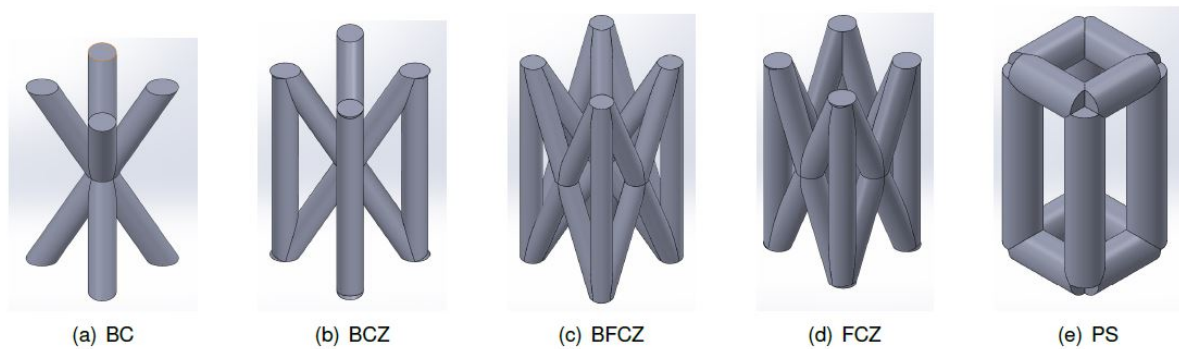


Figure 3.2: Core unit geometries studied by Monteiro et al. [5]. (a) BC - Body Centred; (b) BCZ - Body Centred with Z axis struts; (c) BFCZ - Body and Face Centred with Z axis struts; FCZ - Face Centred with Z axis struts; PS - Parallelepipedic Simple. [5]

In his study, Monteiro concluded that the best unit cell was the Body and Face Centred with Z axis struts (BFCZ). This structure has struts that begin in its vertices which intersect each other in the center of the unit and in the center of the lateral faces of the unit cell. This unit cell also has struts in the Z axis which connect the bottom vertices to the top vertices.

When evaluating the different core geometries, Monteiro et al. [5] always used the same radius and relative density for all the different cores. In order to be able to compare the results of this study with the ones previously found, the BCFZ core geometry will be used but the values of the relative density and the radius of the struts will vary. In his study, Monteiro used a relative density of 0.3 and a radius of 0.92 mm for all the cores. In this study, the relative densities will be 0.25, 0.3 and 0.35; the radius of the struts will be 0.8 mm, 0.92 mm and 1.1 mm. This means that in order to have specimens with all the combinations of radius and relative density, nine different specimens have to be designed.

In the design phase, it was decided that the length and the width of the unit cell are set values which were chosen arbitrarily. It was also decided that these two dimensions would only vary when the radius varies. By designing the specimens in this manner, they can be inscribed in a quadrangular prism, which will greatly facilitate the calculations of the relative density.

The relative density of the core basic unit is dependent of two factors, the radius of the structure and the overall height of the core unit. In order to obtain the desired relative density for each structure, the structures were first designed with a set radius and with no attention to its height. Then using the function "Measure" in the CAD software, the volume of the initial unit (V_{cell}) was obtained.

In order to calculate the relative density of the unit cell, we must create a polygon which encloses the unit cell. This polygon has the same height, width and length of the unit cell. The overall volume of this polygon (V_{Pol}) is:

$$V_{Pol} = L_u \times W_u \times H_u, \quad (3.1)$$

where L_u is the unit cell length, W_u is the unit cell width and H_u is the unit cell height.

Using the V_{Pol} and the volume obtained from CAD software, we can now calculate the relative density (ρ_{Rel}) of the unit cell using:

$$\rho_{Rel} = \frac{V_{unit}}{V_{Pol}} \quad (3.2)$$

Now that we have a reliable method for calculating ρ_{Rel} of the unit cell, we just need to vary the height of the cell core until we will obtain the desired values for the ρ_{Rel} .

Due to the constrains of the AM method, it is not possible to manufacture specimens with the same base dimensions but with all the relative densities desired. So approximate values had to be used and the percent relative error, e_{Rel} , was used to measure the deviation. This method was used to compare

the values of relative density obtained from the CAD software with the theoretical values of relative density desired. For this study, the maximum value of the deviation accepted as satisfactory was 10% .

$$e_{Rel} = \left| \frac{v_{teo} - v}{v_{teo}} \right| \times 100 \quad (3.3)$$

Because the specimens would be built using the AM process, the minimum height must be equal to the dimensions of the base (length and width) in order to avoid printing failures with overhangs. It is also important to note that the specimens with the same radius but with different relative density had to be constructed with the same dimensions of the base. This means that a specimen will only be considered satisfactory if it is able to reach the various values of the desired relative density by only varying its height.

The tables 3.2, 3.3 and 3.4 present the studies performed regarding the height of the unit cells, with the final dimensions highlighted (**red** is used when the desired relative density is 0.35, **blue** for the desired relative density of 0.3 and **magenta** for the desired relative density of 0.25).

Observing the table 3.2, which represent the study for the specimens with 0.8 mm of radius, we can see that it is only possible to build the three different specimens with the base dimensions at 10 mm. This is because using higher or lower base dimensions, it is impossible to create specimens with an acceptable e_{Rel} . If the base dimension were 9.5 mm, it would not be possible to create a specimen with a relative density of 0.25, even taking into account the accepted deviation. When the base dimension was 10.5 mm, it was impossible to create a specimen with a relative density of 0.35, even with the deviation. So the dimensions for the specimens with radius of 0.8 mm are 10 mm for the base dimension and heights of 10 mm, 14.5 mm and 28.5 mm for the relative densities of 0.35, 0.3 and 0.25 respectively.

Observing now table 3.3, used to represent the study for the specimens with 0.92 mm, two different base values were considered for the base dimensions, 11 mm and 11.5 mm. Analysing the specimens with 11 mm for the base dimensions, we can see that it is not possible to design a satisfactory specimen with a relative density of 0.25. So, the dimensions of the base for the specimens with 0.92 mm of radius are 11.5 mm. The heights of the specimens will be 11.5 mm, 16.5 mm and 33 mm for the relative densities of 0.35, 0.3 and 0.25 respectively.

Finally, observing table 3.4 used to represent the study for the specimens with 1.1 mm of radius, we can see that there were also two dimensions considered to the base dimensions, 13.5 mm and 14 mm. Considering the possibility to build all the specimens with the base dimensions of 13.5 mm, we notice that the specimen with the relative density of 0.25 would have to be much higher than all the other specimen previously built. This would result in larger manufacturing times and quantities of material used just to manufacturer this specimen, using the AM method. So, the dimensions of the base chosen for the specimens with 1.1 mm of radius were 14 mm. The heights of said specimens are 14 mm, 17.5 mm and 29 mm for the relative densities of 0.35, 0.3 and 0.25, respectively.

Table 3.2: Study of the height and relative density for specimens with 0.8 mm of radius

Radius (mm)	Base Dimensions (mm)	Height (mm)	V_{cell} (mm ³)	V_{Pol} (mm ³)	ρ_{Rel} Theo	ρ_{Rel} Real	e_{Rel} (%)
0.8	9.5	9.5	308.13	857.375	0.35	0.360	
0.8	9.5	10	319.23	902.5	0.35	0.354	
0.8	9.5	10.5	330.42	8947.625	0.35	0.349	
0.8	9.5	27	731.8	2436.75	0.3	0.300	
0.8	9.5	27.5	744.45	2481.875	0.3	0.300	
0.8	9.5	28	757.12	2527	0.3	0.300	
0.8	9.5	200	5236.71	18050	0.3	0.290	
⋮							
0.8	10	10	330.75	1000	0.35	0.331	5.500
0.8	10	14	422.79	1400	0.35	0.302	0.664
0.8	10	14.5	434.65	1450	0.3	0.300	0.080
0.8	10	15	434.65	1500	0.3	0.298	0.760
0.8	10	28.5	783.57	2850	0.25	0.275	9.975
0.8	10	29	796.51	2900	0.25	0.275	9.863
0.8	10	30	822.19	3000	0.25	0.274	9.625
0.8	10	50	1361.18	5000	0.25	0.272	8.894
⋮							
0.8	10.5	10.5	353.34	1157.625	0.3	0.305	
0.8	10.5	30	835.36	3307.5	0.25	0.253	
⋮							
0.8	12	12	420.92	1728	0.25	0.244	

Table 3.3: Study of the height and relative density for specimens with 0.92 mm of radius

Radius (mm)	Base Dimensions (mm)	Height (mm)	V_{cell} (mm ³)	V_{Pol} (mm ³)	ρ_{Rel} Theo	ρ_{Rel} Real	e_{Rel} (%)
0.92	10.5	10.5	443.15	1157.625	0.35	0.383	
0.92	10.5	15	578.1	1653.75	0.35	0.350	
0.92	10.5	200	6848.5	22050	0.3	0.311	
⋮							
0.92	11	11	473.11	1331	0.35	0.356	1.558
0.92	11	12	502.6	1452	0.35	0.346	1.102
0.92	11	26	947.43	3146	0.3	0.301	0.385
0.92	11	27	980.61	3267	0.3	0.300	0.052
0.92	11	27.5	997.2	3327.5	0.3	0.300	0.105
0.92	11	50	1758.31	6050	0.25	0.291	16.252
0.92	11	100	3497.7	12100	0.25	0.288	15.031
⋮							
0.92	11.5	11.5	503.03	1520.875	0.35	0.331	5.500
0.92	11.5	16	639.84	2116	0.3	0.302	0.794
0.92	11.5	16.5	655.55	2182.125	0.3	0.300	0.134
0.92	11.5	17	671.3	2248.25	0.3	0.299	0.471
0.92	11.5	32.5	1182.43	4298.125	0.25	0.275	10.041
0.92	11.5	33	1199.53	4364.24	0.25	0.275	9.941
0.92	11.5	35	1267.46	4628.75	0.25	0.274	9.529
0.92	11.5	50	1782.03	6612.5	0.25	0.270	7.798
0.92	11.5	100	3521.91	13225	0.25	0.266	6.523
⋮							
0.92	12	12	532.91	1728	0.3	0.308	
0.92	12	50	1804.03	7200	0.25	0.251	

Table 3.4: Study of the height and relative density for specimens with 1.1 mm of radius

Radius (mm)	Base Dimensions (mm)	Height (mm)	V_{cell} (mm ³)	V_{Pol} (mm ³)	ρ_{Rel} Theo	ρ_{Rel} Real	e_{Rel} (%)
1.1	12	12	709.89	1728	0.35	0.411	
1.1	12	90	1509.83	4320	0.35	0.350	
1.1	12	200	9657.82	28800	0.3	0.335	
⋮							
1.1	13.5	13.5	838.45	2460.375	0.35	0.341	2.634
1.1	13.5	20	1121.9	3645	0.3	0.308	2.5972
1.1	13.5	23	1258.27	4191.75	0.3	0.300	0.059
1.1	13.5	23.5	1281.44	4282.875	0.3	0.299	0.266
1.1	13.5	100	5018.89	18225	0.25	0.275	10.154
1.1	13.5	200	9996.29	36450	0.25	0.274	9.699
⋮							
1.1	14	14	881.18	2744	0.35	0.321	8.249
1.1	14	17	1010.12	3332	0.3	0.303	1.052
1.1	14	17.5	1032.06	3430	0.3	0.301	0.297
1.1	14	18	1054.2	3528	0.3	0.299	0.399
1.1	14	28.5	1536.81	5586	0.25	0.2751	10.047
1.1	14	29	1560.45	5684	0.25	0.275	9.814
1.1	14	50	2579.01	9800	0.25	0.263	5.266
1.1	14	100	5068.07	19600	0.25	0.259	3.430
⋮							
1.1	15	15	966.53	3375	0.25	0.286	

It is important to note that for all the specimens with a theoretical relative density of 0.25, it would be possible to design them with a greater height which would result in a smaller relative error when compared to the theoretical relative density. However, as noted in the case before, this would result in longer manufacturing times and large quantities of material used. Because of this, for all these specimens as soon as the relative error would be an acceptable value (below 10%), the specimens were considered satisfactory.

Table 3.5 presents all the specimens with their dimensions, relative densities and relative error regarding the relative densities desired. The technical drawings for all the unit cells can be found in appendix A. All of the unit cells designed for this study are presented from figures 3.3 to 3.11.

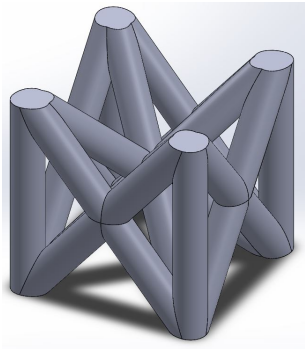


Figure 3.3: Unit Cell 1

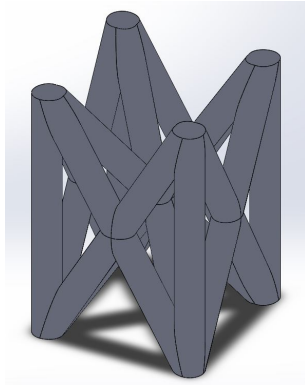


Figure 3.4: Unit Cell 2

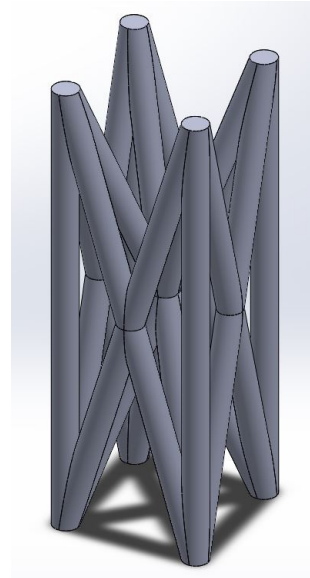


Figure 3.5: Unit Cell 3

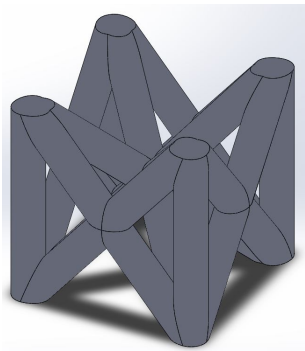


Figure 3.6: Unit Cell 4

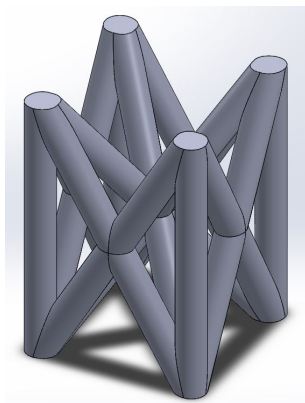


Figure 3.7: Unit Cell 5

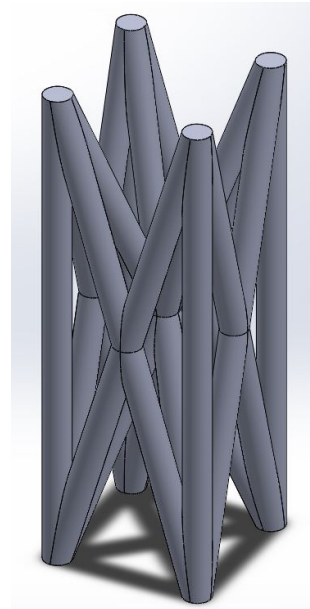


Figure 3.8: Unit Cell 6

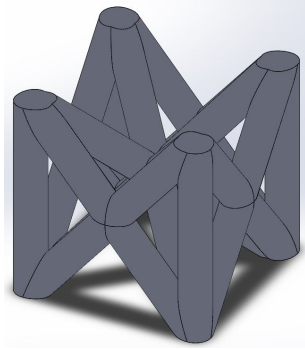


Figure 3.9: Unit Cell 7

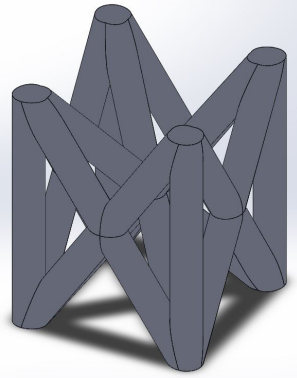


Figure 3.10: Unit Cell 8

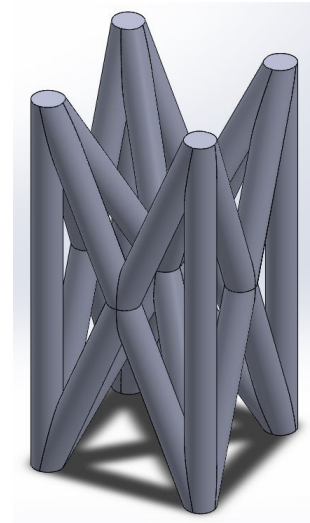


Figure 3.11: Unit Cell 9

Table 3.5: Dimensions and relative densities of the specimens. ρ_{Rel} is the real relative density obtained from the CAD software, ρ_{Teo} is the theoretical relative density that was desired and e_{Rel} (%) is the relative error between both.

Core	Radius (mm)	ρ_{Teo}	Base Dimensions (mm)	Height (mm)	ρ_{Rel}	e_{Rel} (%)
1	0.8	0.35	10	10	0.331	5.500
2	0.8	0.30	10	14.5	0.3000	0.080
3	0.8	0.25	10	28.5	0.275	9.975
4	0.92	0.35	11.5	11.5	0.331	5.500
5	0.92	0.30	11.5	16.5	0.3004	0.134
6	0.92	0.25	11.5	33	0.275	9.941
7	1.1	0.35	14	14	0.321	8.249
8	1.1	0.30	14	17.5	0.301	0.297
9	1.1	0.25	14	29	0.275	9.814

Once the unit cell structures are designed, the final sandwich panel specimens can be designed. Once again, in order to compare the obtained results with the results of Monteiro et al. [5], the specimens were designed to have approximately the same dimensions as the ones previously studied. In his studies, Monteiro et al. [5] used specimens with a length of 167 mm, a width of 53 mm and a total thickness of 22 mm. The value of the total thickness already includes the thickness of the top and bottom plates. These plates have a thickness of 1.25mm. The other dimensions of the plates are dependent on the dimensions of the core and they were designed with an extra 0.5 mm on each edge of the structure so that there is some extra space between the outer edges of the core and the edges of the plate. In order to maintain uniformity, the same design specifications will be used in the design of plates. Using these design specifications, the specimens were built. Table 3.6 presents the dimensions of all the specimens and an example of one of the specimens is shown in figure 3.12.

Because all the specimens are to be tested using 3PB test, it is important that there are z-struts in the middle of the specimen. In order to assure that this happens the number of z-struts in a direction needs to be odd. This will result in an even number of cell repetitions for that direction. This is because the number of z-struts in each direction is the number of repetitions in that direction plus one. This means that the number of z-struts in the length direction will always be an odd number, with one of the struts in the middle of the specimen in the lengthwise direction. Table 3.7 presents the number of repetitions in the length and width directions.

Table 3.6: Dimensions of the structures

Specimen	Radius of Core Structure (mm)	Relative Density of the Core Basic Unit	Length (mm)	Width (mm)	Thickness (mm)
1	0.8	0.35	170.6	53	12.5
2	0.8	0.3	170.6	53	17
3	0.8	0.25	170.6	53	31.5
4	0.92	0.35	176.7	51.1	14
5	0.92	0.3	176.7	51.1	19
6	0.92	0.25	176.7	51.1	35.5
7	1.1	0.35	168.4	50.4	16.5
8	1.1	0.3	168.4	50.4	20
9	1.1	0.25	168.4	50.4	31.5

Table 3.7: Number of cell repetitions in the length and width directions

Specimen	Number of Repetitions	
	Lengthwise	Widthwise
1	20	6
2	20	6
3	20	6
4	18	5
5	18	5
6	18	5
7	14	4
8	14	4
9	14	4

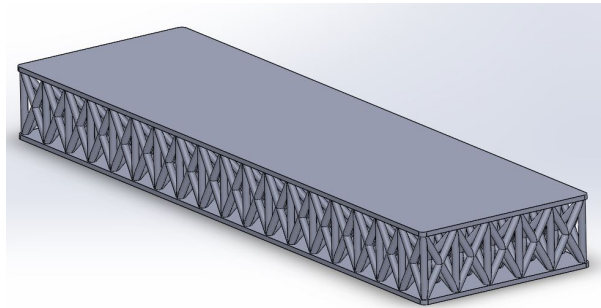


Figure 3.12: Specimen 5 - one example of the specimens designed for this study

3.2 Specimens Manufacture

In order for the experimental results to have a certain degree of certainty, 3 copies of each specimen were produced. This means that for the nine different types of specimens, a total of 27 specimens were printed. The prints were made in an Ultimaker 3 printer, which is shown in figure 3.13.

All the specimens were manufactured using the FDM method. As mentioned before, after the CAD designed is finished and saved into an STL format, the next step is introducing the STL file into a slicer software. In this case, the software used was CURA from Ultimaker. The slicer software slices the design and produces a G-Code file that machines can read. This G-file contains the path for the extruder head to follow and all the manufacturing parameters.

As mentioned in subsection 3.1.1 , the material used was PLA from 3D Filkemp PrintMaster Pro. The choice of the printing parameters is an important aspect as these are the factors that will determine the print quality. Because of this importance studies were made on the effect of these parameters [23]. The material was extruded with a temperature of 205°C and the build plate was at a temperature of 60°C. The print was made with an infill fraction of 100% and without the use of supports. A full list of all the manufacturing parameters can be found in appendix B. Two photographs of the printing process can be seen in figure 3.14. A mention must be made to the printing velocity. Although this parameter can be set with all the others parameters previously, the printer head sometimes need to move at a slower speed

because of the more complex geometry of the core. This would result in an average increase of 33% of all the theoretical printing times.



Figure 3.13: Ultimaker 3 - The 3D printer used to manufacture all the specimens

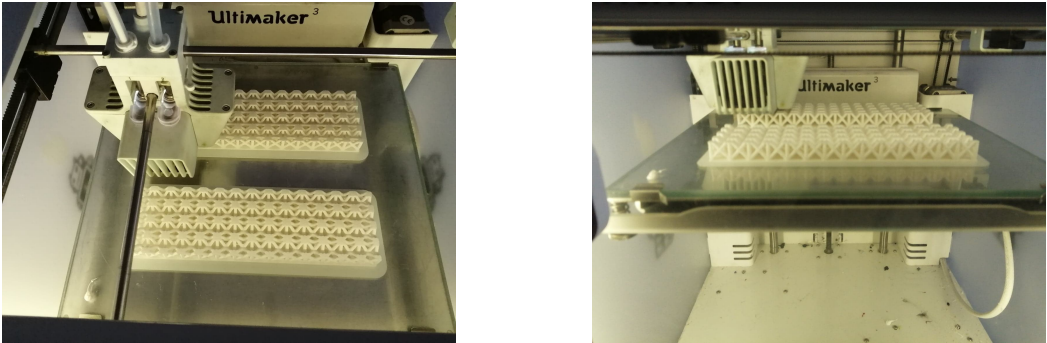


Figure 3.14: Two photographs taken during the printing process. In these photographs, we can see that two specimens are being printed at the same time. This option, despite being valid, is more prone to printing problems.

As it is the case with any manufacturing process, there are always imperfections and deviations between the theoretical models and the manufactured ones. So, all the specimens were measured and weighted after manufacturing. The dimensions measured after manufacturing and theoretical manufacturing times can be found in table 3.8.

Table 3.8: Dimensions of the specimens measured after manufacturing and theoretical printing times

Specimen	Length (mm)	Width (mm)	Thickness (mm)	Weight (g)	Theoretical Printing Time (hh:mm)
1.1	170.2	52.80	12.40	49.458	12:27
1.2	170.2	53.08	12.32	51.093	12:27
1.3	170.0	52.86	12.32	50.683	12:27
2.1	170.8	53.07	16.85	58.689	16:43
2.2	170.6	53.15	16.78	57.138	16:43
2.3	171.0	52.98	16.89	57.196	16:43
3.1	170.8	52.69	31.40	80.698	29:54
3.2	170.3	52.71	31.35	84.766	29:54
3.3	170.2	52.70	31.27	83.872	29:54
4.1	176.8	51.12	14.12	52.273	12:15
4.2	176.7	51.19	14.17	52.343	12:15
4.3	177.8	51.04	13.38	50.823	12:15
5.1	177.0	51.39	18.91	61.715	15:57
5.2	176.8	51.21	18.79	60.601	15:57
5.3	176.5	51.04	18.70	61.738	15:57
6.1	176.5	50.82	35.26	97.623	28:22
6.2	176.7	50.80	35.20	97.320	28:22
6.3	176.2	50.79	35.37	97.392	28:22
7.1	168.4	50.15	16.42	58.318	11:51
7.2	168.9	50.50	16.45	57.679	11:51
7.3	168.6	50.21	16.58	56.678	11:51
8.1	168.5	50.11	19.93	62.503	13:47
8.2	168.8	50.18	19.75	63.431	13:47
8.3	168.3	50.44	19.93	64.526	13:47
9.1	168.5	50.08	31.15	83.459	20:11
9.2	168.1	50.11	31.42	85.154	20:11
9.3	168.1	50.08	31.40	84.279	20:11

3.3 Experimental Procedure

All the geometries manufactured were subjected to a **3 Point Bending** test (3PB test). These tests were performed following the standard ASTM C393 – 00 (Standard Test Method for Flexural Properties of Sandwich Constructions) [67]. A representation of this type of test can be seen in figure 3.15 and in figure 3.16 two specimens prior to being tested are presented.

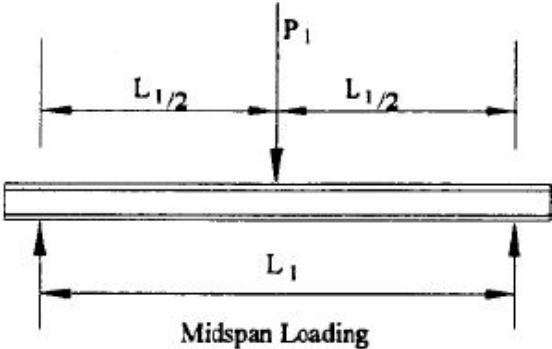


Figure 3.15: Loading diagram of a 3PB test

Because of the geometry of the unit cell, it is desirable that the loads are applied on the z-struts. However, due to different dimensions of the unit cells and of the specimens, this means that the midspan distance (represented by L_1 in the figure 3.15) and the overhang distance (horizontal distance between the beginning of the specimen and the bottom rollers) have to be adjusted for each specimen. As it is impossible to have the same midspan and overhang distances for all the specimens, the values were chosen in order to have the least amount of deviation between said values. The midspan and overhang distances can be found in table 3.9.

Table 3.9: Midspan and overhang distances

Specimen	Midspan (mm)	Overhang (mm)
1	140	30
2	140	30
3	140	30
4	138	34.5
5	138	34.5
6	138	34.5
7	140	28
8	140	28
9	140	28

The equipment used for all the experimental process was an Instron 3369 with a 50 kN load cell, which can be seen in figure 3.17. With this equipment, it is the upper roller that moves, and the two bottom rollers are fixed. For all the experimental procedures the upper roller moved downward at a speed of 2.5 mm/min. The load-displacement data from the procedures were obtained using the Bluehill software.



Figure 3.16: Two different specimens before the beginning of the experimental procedure



Figure 3.17: Instron 3369 with a specimen prior to initiating a procedure

3.4 Numerical Simulation

The numerical simulation made for this work was executed with the software Siemens NX, version 1915. This software uses the **Finite Element Method (FEM)** in its calculations. In order to proceed to all the calculations necessary, this software needs three different files: a part file, a fem file and a sim file. When all these files are ready, a solution solver to define the parameters of the solution is needed. Because there are nine different specimens, each specimen will need its part, fem and sim file. This means that 27 different files are needed to make a numerical simulation for all the specimens.

3.4.1 Part file

The part file is where all the geometries models needed for the numerical simulation are created. In this case, that included the rollers of the 3PB test. These geometries were created with the support of the Siemens NX CAD software.

There was an option to import the designs made in Solidworks to manufacture the specimens into the Siemens NX CAD software. However, taking this course of action would have resulted in extremely long processing times, because all the geometries would be represented by a 3D model. But in fact, the 3D model of the sandwich panels can be substituted with 1D and 2D geometries without the loss of accuracy or precision of the results. So, the top and bottom skins were substituted by bounded planes and the struts are substituted by lines.

Another way to simplify the model is divide it and introduce symmetries in the model. In order to be able to make this simplification, the symmetry plane must have a row or column of z-struts. As the symmetry planes must be in the middle of the specimen, this means that there must be z-struts in the middle of the specimen, either lengthwise or widthwise. So, this means that a symmetry plane can be used in a direction if the number of cell repetitions in that direction is even, as mentioned in section 3.1.2. Observing the table 3.7, we can see that all the specimens can have a symmetry plane that divides them in half in the length direction. In the width direction however, the specimens 4, 5 and 6 cannot be divided. This means that the said specimens can only have one symmetry plane and the other specimens can have two symmetry planes. Despite this, it was observed that introducing a symmetry plane in the width direction would lead to less accurate results. So, all the simulations were made with only a symmetry plane in the length direction. One of the part files design can be seen in figure 3.18.

One particularity of the part files is the usage of the divide face command. This command is used in to define the struct-skins connection area (further explained in section 3.4.2) and to divide the contact areas of the skins. The division of the contact areas of the skins aids in reducing the processing time.

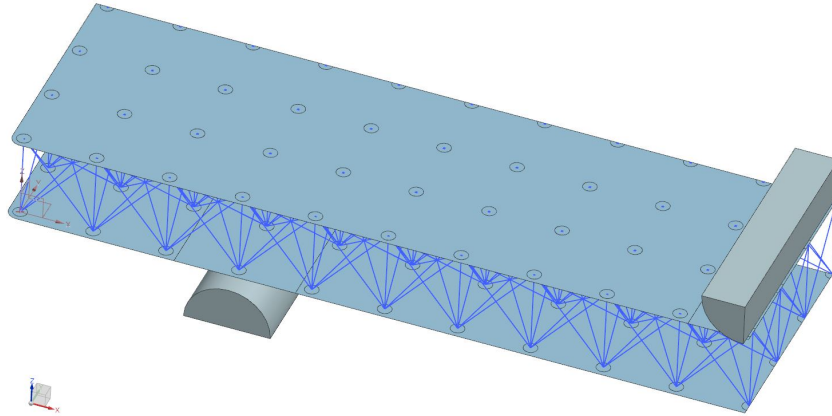


Figure 3.18: One of the part files created

3.4.2 Fem file

The fem file is where all the meshes are created and applied to models created in the part file. It is also in this file where the materials are assigned to the model.

In this fem file, a 1D mesh was applied to all the struts. This 1D mesh was a CBEAM type mesh with a cross-section defined as ROD and it has 8 elements for each strut. The value of the radius r for the ROD cross-section is dependent on the type of specimen and it can be seen in table 3.6.

The skins, which were substituted by bounded planes, have a 2D mesh. Because of the contacts between the skins and the rollers, the top and bottom skins must be defined as two different meshes. This happens because each skin needs to have its normal pointing different directions. Both these 2D meshes are of the CQUAD4 type with a defined thickness of 1.25 mm as this is the thickness of both skins. The meshing method used was the paver method. As these meshes have the most critical area, a mesh refinement study in order to choose an appropriate element size was applied. This study can be seen in section 3.4.5.

To properly connect the 1D mesh to the 2D meshes, meaning the struts to the skins, the user needs to define the connections. This can be done with the command 1D Connections. All the connectors are Point to Face with the RB3 type.

The last mesh that needs to be defined is the 3D meshes applied to the rollers. In this case, again because of the contacts, two different meshes need to be applied. The meshes used were 3D Swept Mesh with the CHEXA(8) type. In order to obtain good results, the element size of these meshes must correspond to the element size used for the 2D meshes. So, after the mesh refinement study, present in section 3.4.5, the correct element size will be found.

The material assigned to the 1D mesh and to the 2D meshes, which represent the struts and skins, was the PLA-N. To the 3D meshes the material used was the AISI 410 Stainless Steel.

Figure 3.19 represents one of the finalized Fem files created. Figures 3.20, 3.21, 3.22 and 3.23 represent the characteristics of the 1D mesh, 1D connections, 2D mesh and 3D mesh, respectively.

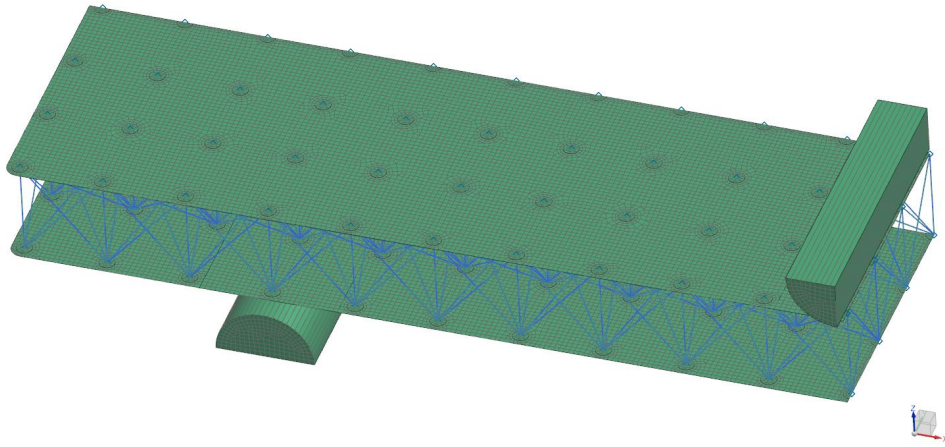


Figure 3.19: One of the fem files created

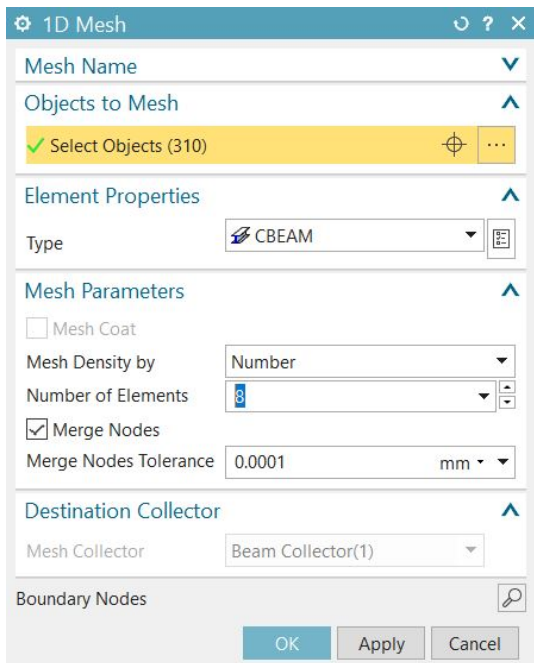


Figure 3.20: 1D mesh characteristics

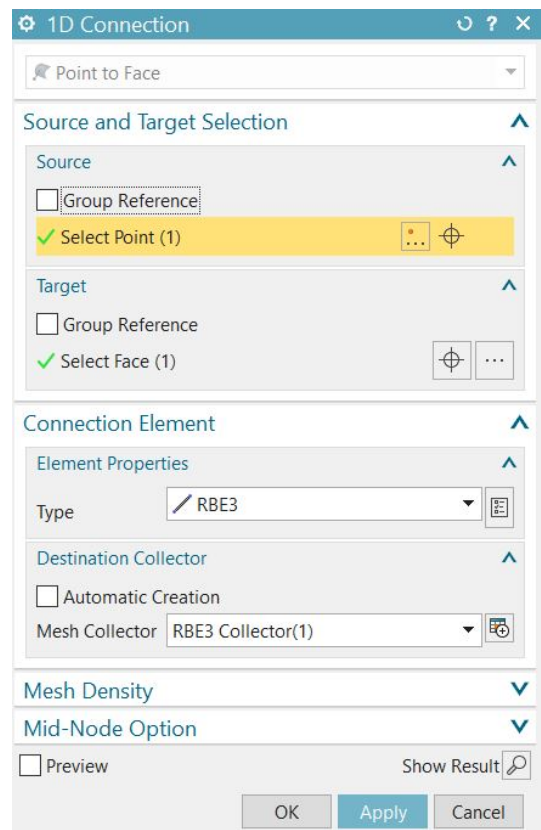


Figure 3.21: 1D point to face connections characteristics

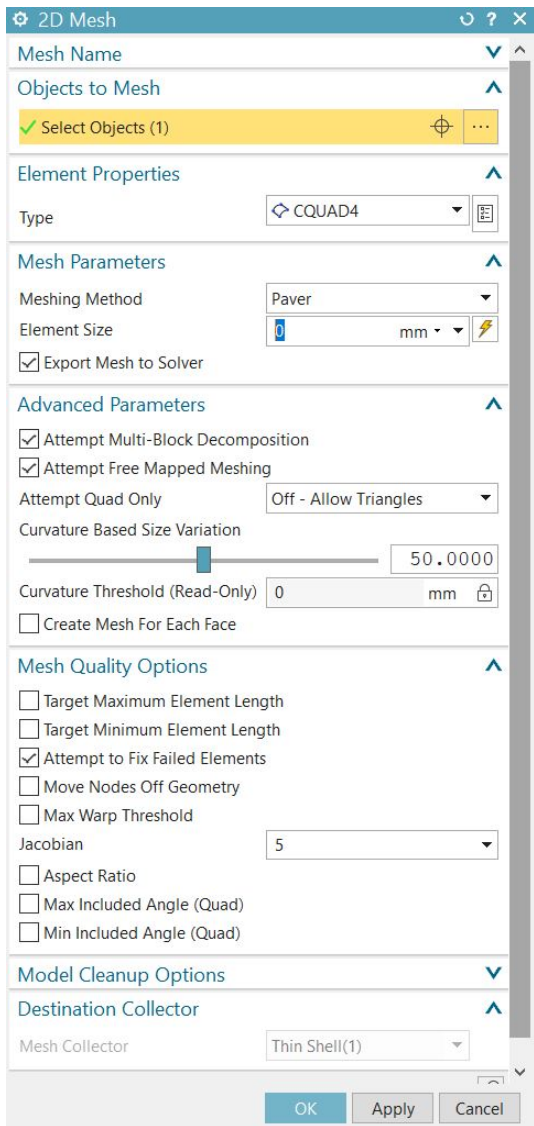


Figure 3.22: 2D mesh characteristics

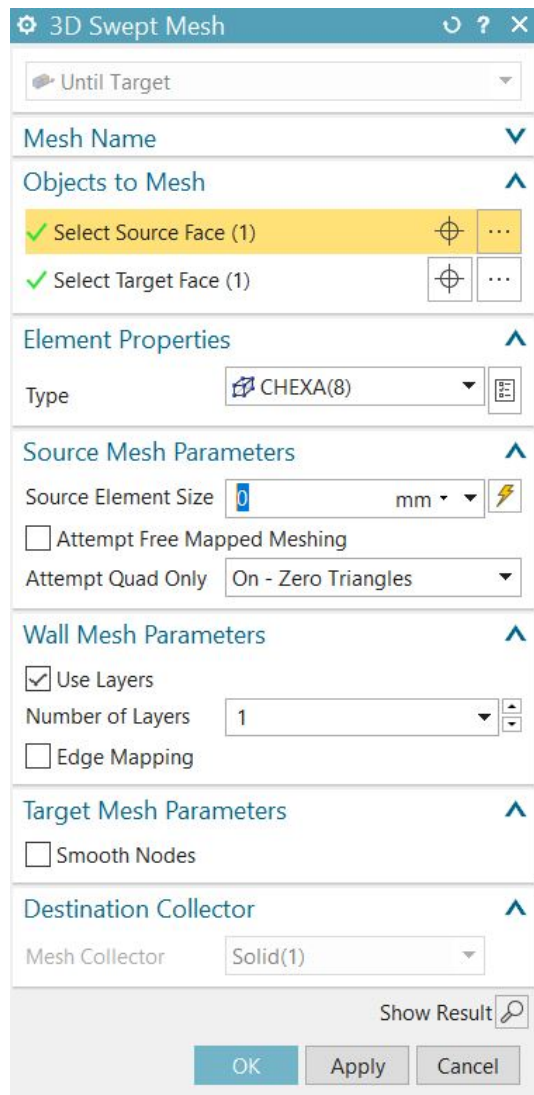


Figure 3.23: 3D mesh characteristics

3.4.3 Sim File

The sim file is the last file needed before running the numerical simulation. It is in this file that contacts and constraints are applied. Figure 3.24 represents one of the finalized sim files. As it can be seen in that picture, the contacts are shown in orange and the constraints are shown in blue.

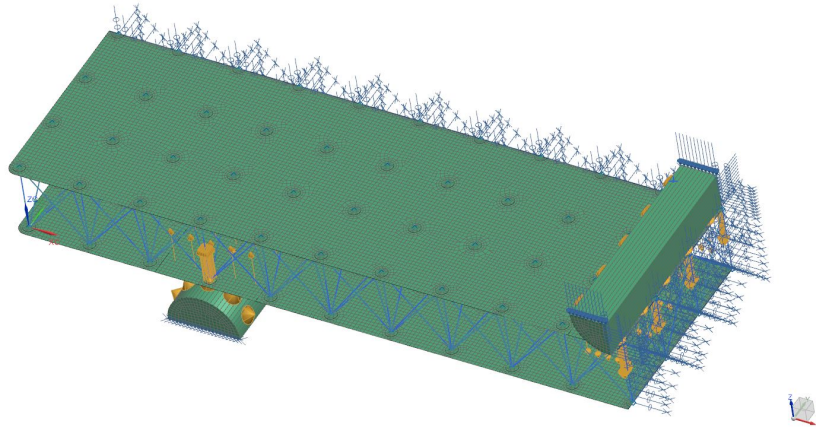


Figure 3.24: A sim file created

There are two contacts defined in this file, one between the bottom roller and the bottom skin contact area and another between the top roller and the top skin contact area. These two contacts have a coefficient of static friction of 0.3. In figure 3.25, all the contact parameters can be seen.

Along with the contact constraints, other constraints need to be added in order to have a correct simulation. A fixed constraint needs to be applied to the bottom roller, which tells the program that the mesh associated with that roller cannot move. An enforced displacement constraint needs to be applied to the top roller. Without this constraint, no stresses are applied to any of the meshes and the numerical simulation fails. The properties of the enforced displacement constraint can be seen in figure 3.26.

The symmetric constraints also need to be added and along with this symmetric constraints other constraints that define the degrees of freedom in the symmetry planes need to be added, otherwise the simulation will fail. These said constraints prevent the struts and skins from moving in a manner that is not real. As it was mentioned in section 3.4.1, symmetry planes can be applied in the lengthwise and widthwise directions, however the symmetries used were only applied to the lengthwise directions. Along with the addition of a constrain defining the symmetry plane, constrains need to be added allowing the struts and skins only to move along the z-axis and to only have rotations along the y-axis. An example for a constraint of this type applied to the struts can be seen in figure 3.27.

Because there are two types of geometries that are in these symmetry planes, the struts (1D elements) and the skin edges (2D elements), this means that there is need to add two extra constraints. This means that for each symmetry plane added, three different constraints need to be added: one defining the symmetry plane, one defining the degrees of freedom of the struts and another defining the degrees of freedom of the skins edges.

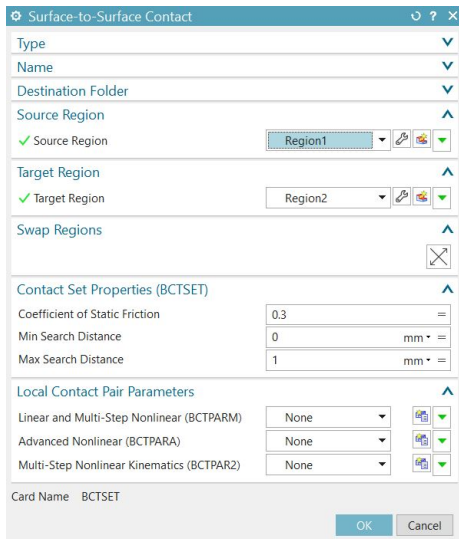


Figure 3.25: Contact parameters used for both contacts

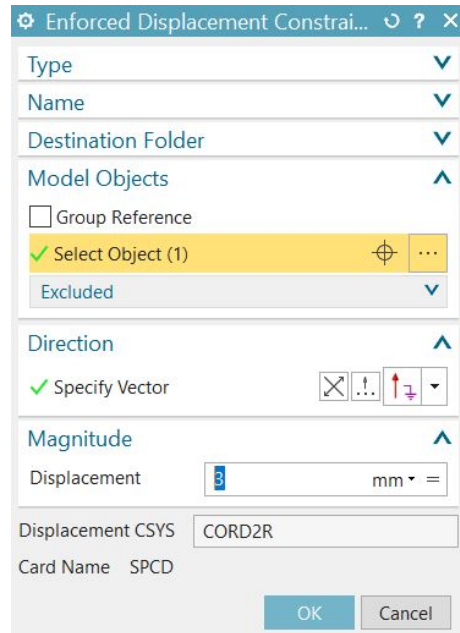


Figure 3.26: Enforced displacement constraint parameters

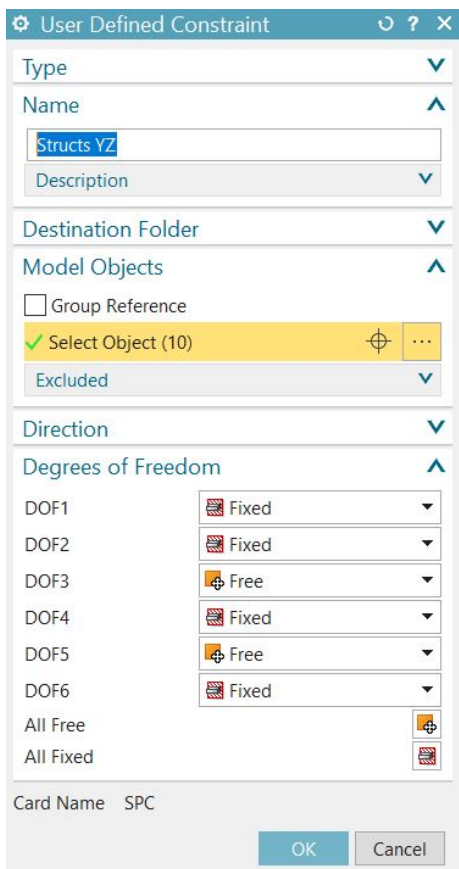


Figure 3.27: Constraint for the struts when using a y0z symmetry plane

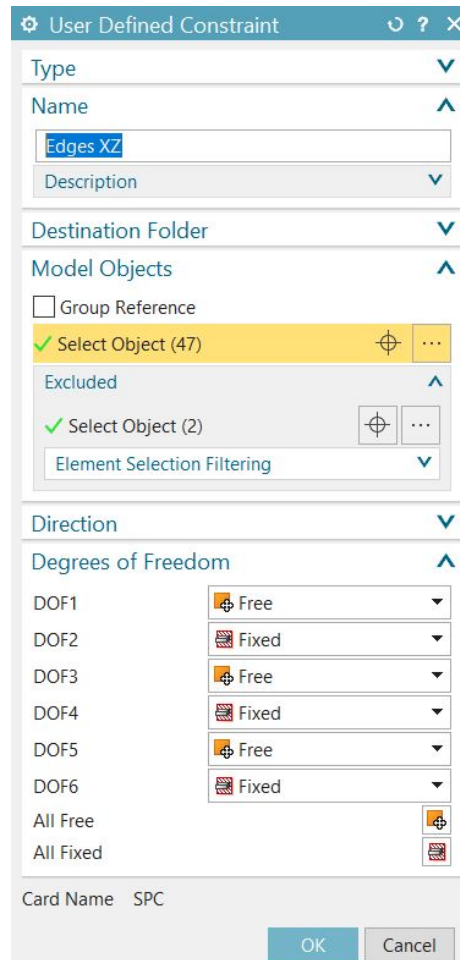


Figure 3.28: Constrain for the polygon edges when using a x0z symmetry plane

3.4.4 Solution Solver

When starting any sim file, the user is immediately prompted to define the solution. The solution is where the user defines which results are desired. In this case the SOL 101 Linear Statics - Global Constraints was chosen, which provides the standard Structural Output Requests. These outputs include displacement, elemental and nodal stress, reaction forces, von Mises stress among many others. These results will be analysed in section 4.

The only alteration that was made in the solution from the standard options, was changing the option AUTOMPC to Yes. This change can be made in the Bulk-Data section of the solution, in the Parameters folder. This is needed because some of the constrains applied in this file are applied to the nodes of the 1D Connectors created in the Fem file. If this option is not changed, a fatal error message will appear when solving the simulation.

The characteristics of the solution solver can be seen in figure 3.29.

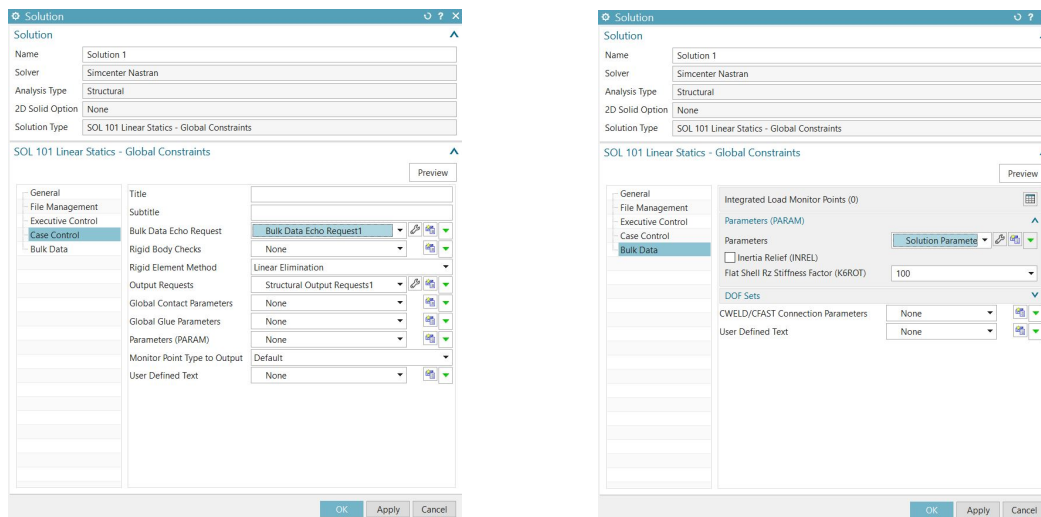


Figure 3.29: Solution characteristics - The case control section where the outputs are defined and bulk data section where the solution parameters are defined.

3.4.5 Mesh Refinement

After the part, fem and sim files are correctly created, a mesh refinement must be applied to the meshes created in the fem file in order to extract accurate results from the numerical simulations. The meshes of the skins were studied and refined because it is on these meshes that the maximum von Mises stresses are observed.

A mesh refinement study depends heavily on the element size presented in that mesh. Various meshes are created and the simulation is run. The desired result, which in this case is the von Mises stress, is registered and studied. When the results achieve an acceptable level of uniformity, meaning when the difference between values registered is less than 5%, the element size of the mesh is considered adequate. It is with these element sizes of the meshes that the simulations must be performed and the results registered.

An individual mesh refinement study was performed for each specimen. The studies were performed with a 3PB test with a displacement of 3 mm and the resulting von Mises stress were registered. These studies can be observed from figures 3.30 to figures 3.38.

As it can be seen in the figures mentioned, the variations of the von Mises stresses are, at the maximum, about 2.89%. Despite the various values and variations of the von Mises stresses, a trend can be noted in the specimens which have the same radius. For the specimens 1, 2 and 3, which have a radius of 0.8 mm, a neglectable variation of the von Mises stresses can be seen between elements with 0.65 mm and 0.7 mm. So, one of these element sizes is appropriate to perform the numerical simulations. The same conclusion can be applied to the group of specimens 4, 5 and 6, which have a radius of 0.92 mm, and to the group of specimens 7, 8 and 9, which have a radius of 1.1 mm. But on these cases the element size is not the same. For the specimens 4, 5 and 6 the neglectable variation of the von Mises stresses can be seen between elements with 0.7 mm and 0.75 mm size. For the specimens 7, 8 and 9 the neglectable variation of the von Mises stresses can also be seen between elements with 0.6 mm and 0.65 mm size. The choice of element size for each specimen and the corresponding number of elements and values of maximum variation of von Mises stress can be observed in table 3.10.

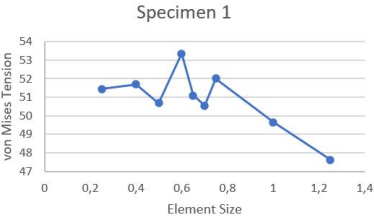


Figure 3.30: Mesh refinement for the specimen 1

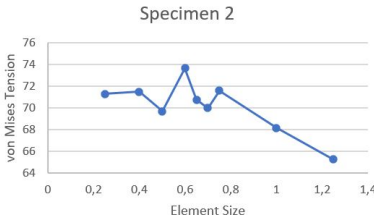


Figure 3.31: Mesh refinement for the specimen 2

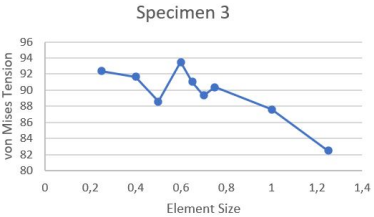


Figure 3.32: Mesh refinement for the specimen 3

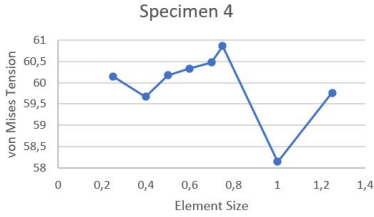


Figure 3.33: Mesh refinement for the specimen 4

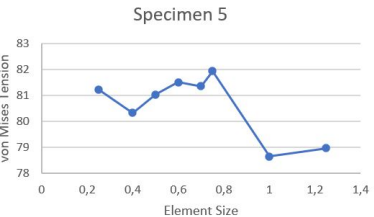


Figure 3.34: Mesh refinement for the specimen 5

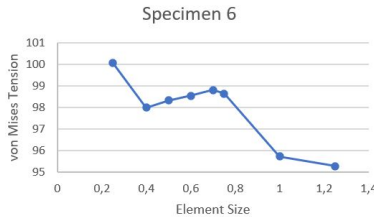


Figure 3.35: Mesh refinement for the specimen 6



Figure 3.36: Mesh refinement for the specimen 7



Figure 3.37: Mesh refinement for the specimen 8

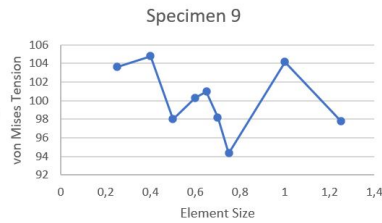


Figure 3.38: Mesh refinement for the specimen 9

Table 3.10: Results of the mesh refinement applied to the 2D bounded planes

Specimen	Element Size (mm)	Total Number of Elements	Maximum variation of von Mises Stress (%)
1	0.7	22483	2.89
2	0.7	22486	2.27
3	0.7	22491	1.88
4	0.7	22031	0.65
5	0.7	22028	0.73
6	0.7	22002	0.26
7	0.6	26457	2.08
8	0.6	26471	1.96
9	0.6	26471	2.37

Chapter 4

Results

In this chapter, the results of the experimental procedures and of the numerical simulations are presented and compared.

4.1 Numerical Simulations

From figures 4.1 to 4.9 the results of the FEA analysis for all the specimens are presented. The vertical displacement, the von Mises stresses in the skin elements and the vertical reaction forces applied to the top roller are presented for the specimen 1 but for the other specimens only the von Mises stresses in the skin elements are presented.

The table 4.1 summarizes the most important results from the FEA for each specimen. These results are the maximum vertical displacement, the maximum von Mises stress registered in the top skin and the vertical reaction force applied to the top roller. All these results were obtained by applying a enforced displacement of 4 mm to the top roller.

Table 4.1: FEA Results

Specimen	Vertical Displacement (mm)	Maximum σ_{VM} in top Skin (MPa)	Applied Force in top Roller (N)
1	4.007	67.72	457.08
2	4.009	93.56	853.97
3	4.022	119.61	1756.97
4	4.008	81.01	594.186
5	4.013	108.92	1075.21
6	4.026	131.97	2086.16
7	4.010	87.54	791.78
8	4.012	104.83	1145.40
9	4.021	133.99	2133.77

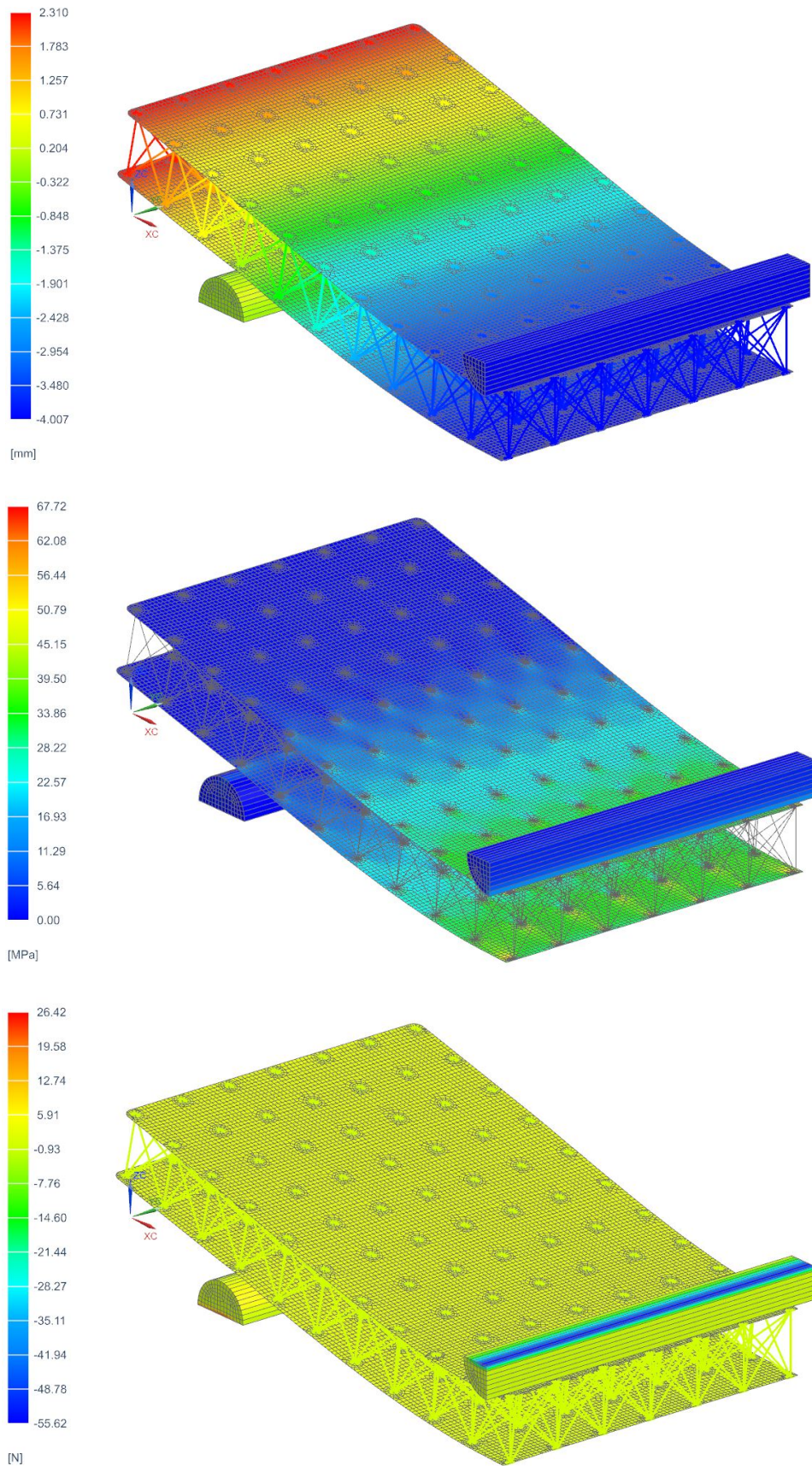


Figure 4.1: FEA of the specimen 1 under a 3PB test. The first picture presents the vertical displacement, the second picture presents the σ_{VM} on the skins and the third picture presents the vertical reaction forces applied to the rollers.

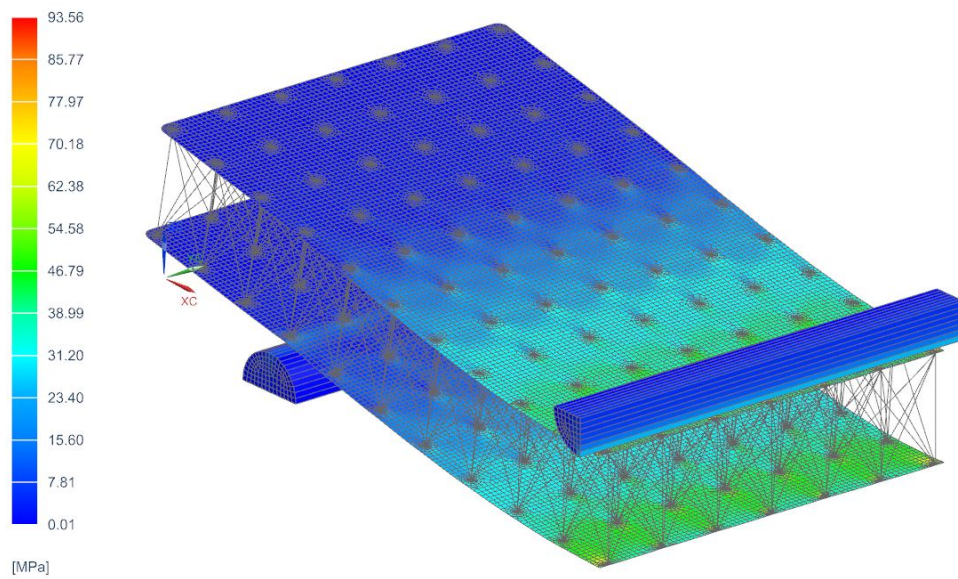


Figure 4.2: FEA of the specimen 2 under a 3PB test. The results presented are the σ_{VM} on the skins elements.

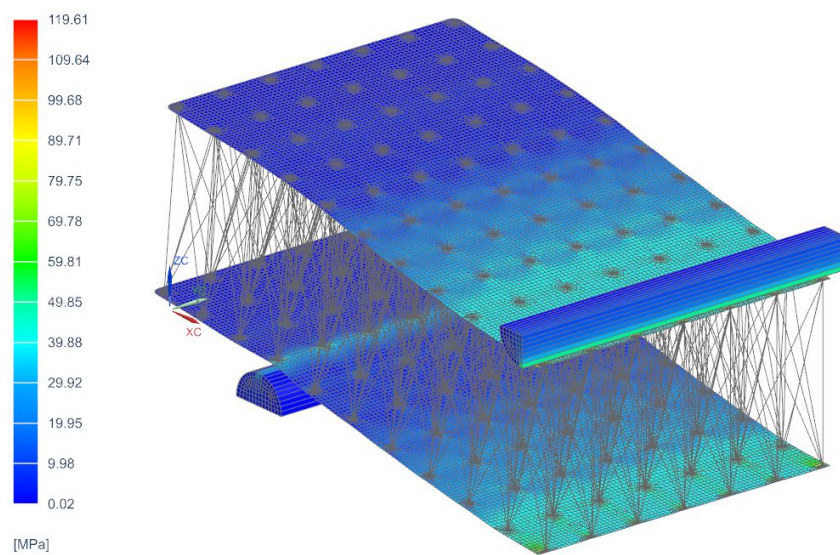


Figure 4.3: FEA of the specimen 3 under a 3PB test. The results presented are the σ_{VM} on the skins elements.

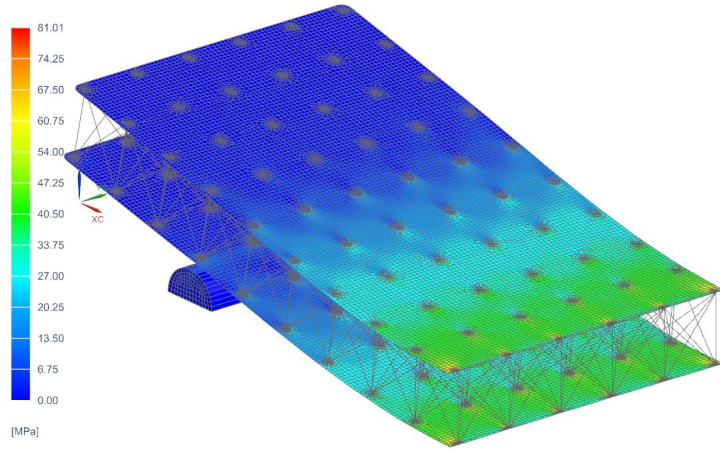


Figure 4.4: FEA of the specimen 4 under a 3PB test. The results presented are the σ_{VM} on the skins elements.

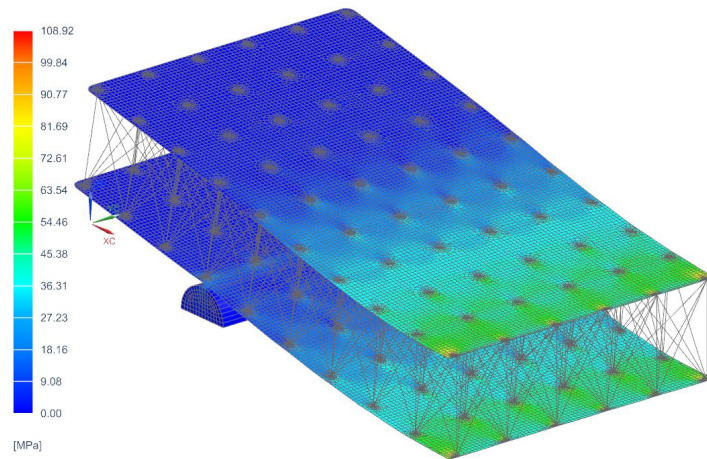


Figure 4.5: FEA of the specimen 5 under a 3PB test. The results presented are the σ_{VM} on the skins elements.

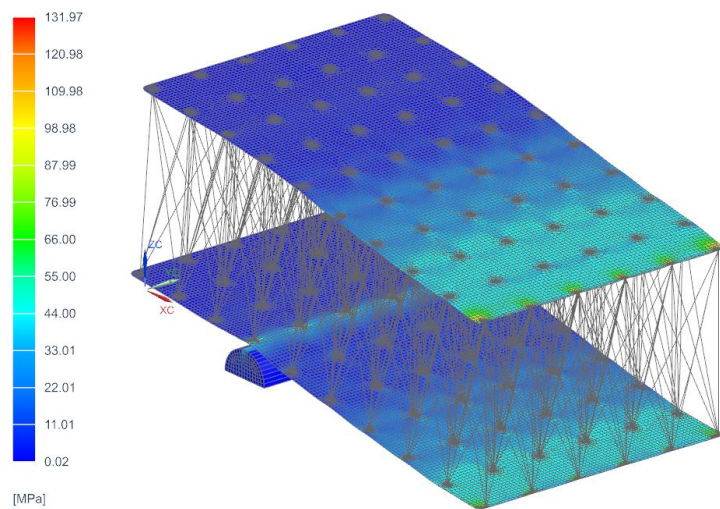


Figure 4.6: FEA of the specimen 6 under a 3PB test. The results presented are the σ_{VM} on the skins elements.

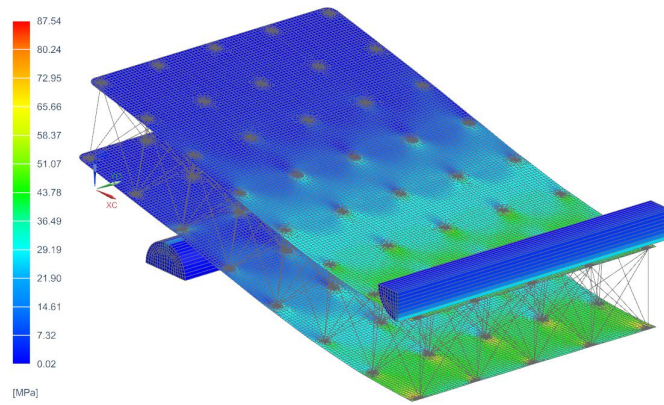


Figure 4.7: FEA of the specimen 7 under a 3PB test. The results presented are the σ_{VM} on the skins elements.

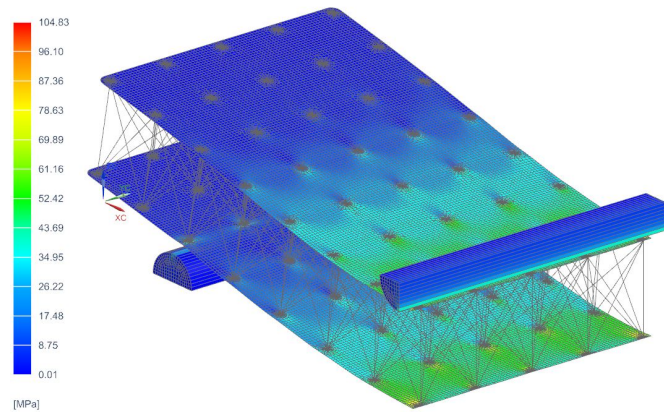


Figure 4.8: FEA of the specimen 8 under a 3PB test. The results presented are the σ_{VM} on the skins elements.

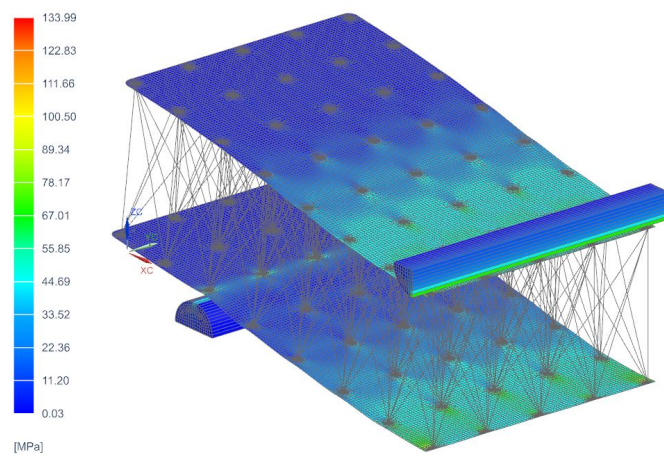


Figure 4.9: FEA of the specimen 9 under a 3PB test. The results presented are the σ_{VM} on the skins elements.

Table 4.2: FEA Results, specifically the force applied to the top roller, the maximum von Mises stress registered in the top skin, the stiffness and the absorbed energy by the specimens until a displacement of 4 mm

Specimen	Applied Force in top Roller (N)	Maximum σ_{VM} in top Skin (MPa)	Stiffness K (N/mm)	Absorbed Energy (J)
1	457.08	67.72	114.27	0.91
2	853.97	93.56	213.49	1.71
3	1756.97	119.61	439.24	3.51
4	594.19	81.01	148.35	1.19
5	1075.21	108.92	268.86	2.15
6	2086.16	131.97	521.77	4.17
7	791.78	87.54	197.95	1.58
8	1145.40	104.83	286.35	2.29
9	2133.77	133.99	533.44	4.27

Load-Displacement Curves

The figure 4.10 presents the numerical load-displacement curves of all the specimens studied. Using these curves, it is possible to calculate the stiffness K and the absorbed energy. The vertical forces applied to the top rollers were all registered with a displacement of 4 mm. The stiffness K is equivalent to the slope of the load-displacement curve and the absorbed energy is the area below each curve. All the results for the mentioned properties can be seen in table 4.2.

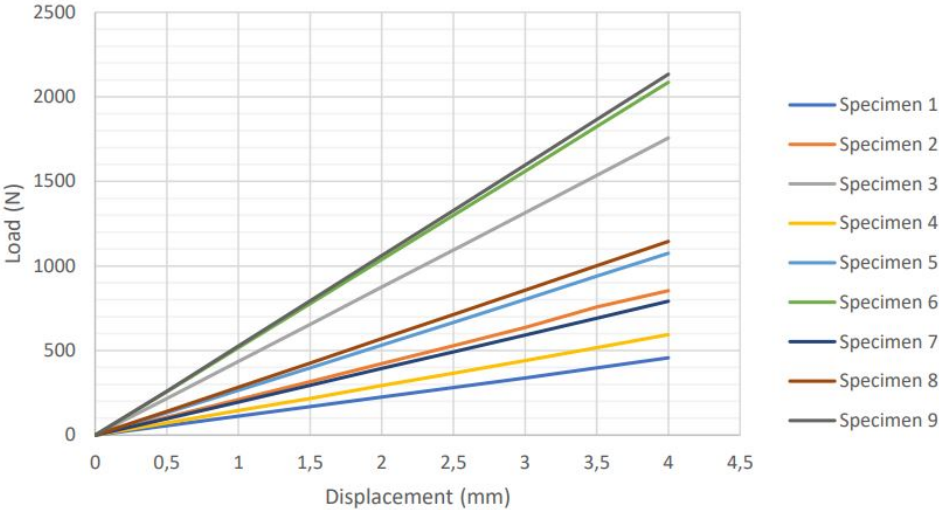


Figure 4.10: Numerical load-displacement curves of all the specimens analysed in this document

Observing now both figure 4.10 and table 4.2, we can make comparisons and draw conclusions from the data. In order to better analyse and compare the results, the data was re-arranged, depending on the variable. In table 4.3 the specimens are grouped by their strut radius in order to compare the effects of the relative density; in table 4.4 the specimens are grouped by their relative density in order to compare the effects of the strut radius.

Table 4.3: FEA results, where the specimens are grouped by radius

Specimen	Radius (mm)	Relative Density	Applied Force in top Roller (N)	Maximum σ_{VM} in top Skin (MPa)	Stiffness K (N/mm)	Absorbed Energy (J)
1	0.8	0.35	457.08	67.72	114.27	0.91
2		0.3	853.97	93.56	213.49	1.71
3		0.25	1756.97	119.61	439.24	3.51
4	0.92	0.35	594.19	81.01	148.35	1.19
5		0.3	1075.21	108.92	268.86	2.15
6		0.25	2086.16	131.97	521.77	4.17
7	1.1	0.35	791.78	87.54	197.95	1.58
8		0.3	1145.40	104.83	286.35	2.29
9		0.25	2133.77	133.99	533.44	4.27

Table 4.4: FEA results, where the specimens are grouped by relative density

Specimen	Relative Density	Radius (mm)	Applied Force in top Roller (N)	Maximum σ_{VM} in top Skin (MPa)	Stiffness K (N/mm)	Absorbed Energy (J)
1	0.35	0.8	457.08	67.72	114.27	0.91
4		0.92	594.186	81.01	148.35	1.19
7		1.1	791.78	87.54	197.95	1.58
2	0.3	0.8	853.97	93.56	213.49	1.71
5		0.92	1075.21	108.92	268.86	2.15
8		1.1	1145.40	104.83	286.35	2.29
3	0.25	0.8	1756.97	119.61	439.24	3.51
6		0.92	2086.16	131.97	521.77	4.17
9		1.1	2133.77	133.99	533.44	4.27

Observing first the table 4.3, we can see that a decrease of the relative density leads to a better performance of the specimen in all the studied parameters. But there is a trade-off because decreasing the relative density this geometry will lead to higher thickness and so higher production times, as it can be seen in table 3.8.

Observing now the table 4.4, we can see that an increase of the radius leads to a better performance of the specimen in all the studied parameters. Again, the same trade-off regarding the production time must be consider, as an increase of radius leads to higher production times.

4.2 Experimental Results

The specimens were subjected to a 3PB tests and the data was extracted from the test machine using the Bluehill software. The data extracted were the load-displacement curves for each specimen, which was later used to calculate the most important parameters for each specimen. The 27 experimental results obtained were divided into 9 different groups, one for each of type of specimen studied. The load-displacement curves are presented from figure 4.11 to figure 4.19, in which the last point of each curve is the maximum load applied to that specimen.

As it can be seen in the figures of the load-displacement curves for the tested specimens, their behaviour is consistent and there are not big deviations between specimens of the same type. All the curves present a long elastic region and then, as the the deformation enters the plastic regime, the plastic curve appears until the collapse. This leads to the conclusion that the specimens have a bending dominated behaviour and a brittle fracture.

Table 4.5 presents all the important parameters. It is important to mention that all the values presented were obtained until the maximum load point for each specimen. The stiffness is calculated from each curve by performing a linear regression to the points acquired. In order to have high degree of certainty, Matlab was used. The linear regression was applied to all the possible intervals of points that had at least 30% of all the total points registered until the maximum force point. Using this approach, the minimum value of R^2 achieved was $R_{min}^2 = 0.999$.

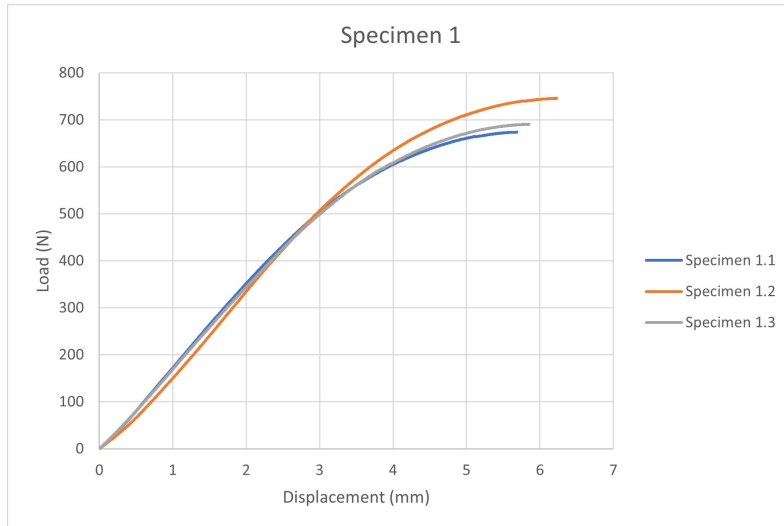


Figure 4.11: Experimental load-displacement curves of all the specimens 1

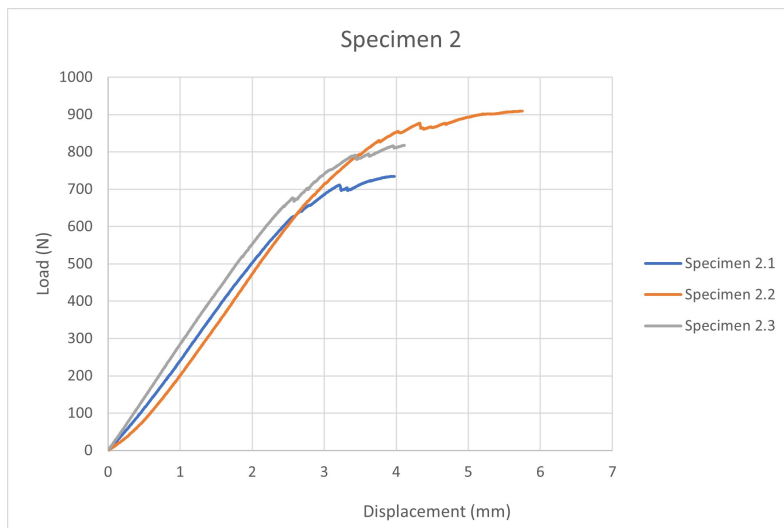


Figure 4.12: Experimental load-displacement curves of all the specimens 2

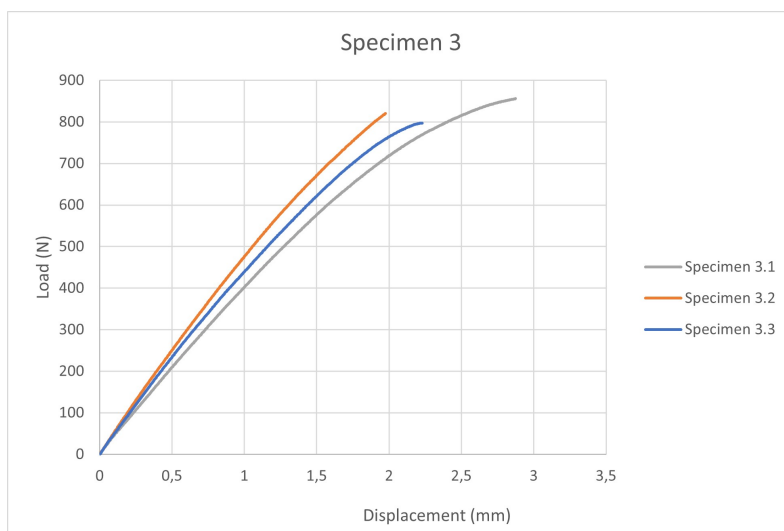


Figure 4.13: Experimental load-displacement curves of all the specimens 3

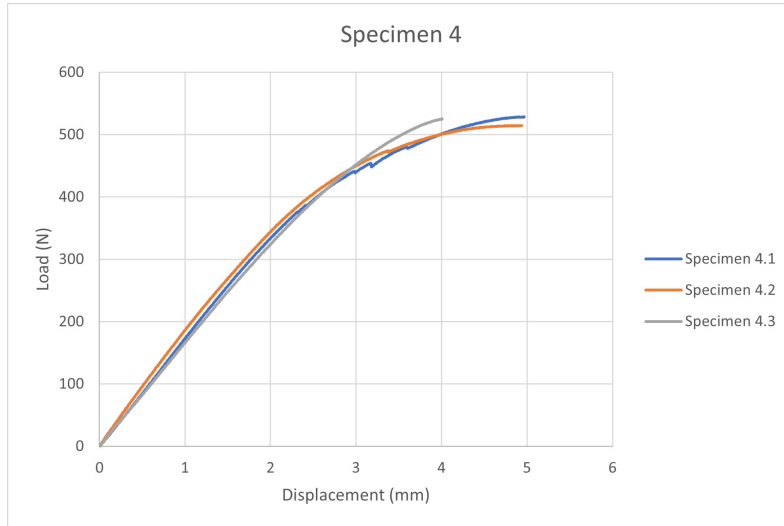


Figure 4.14: Experimental load-displacement curves of all the specimens 4

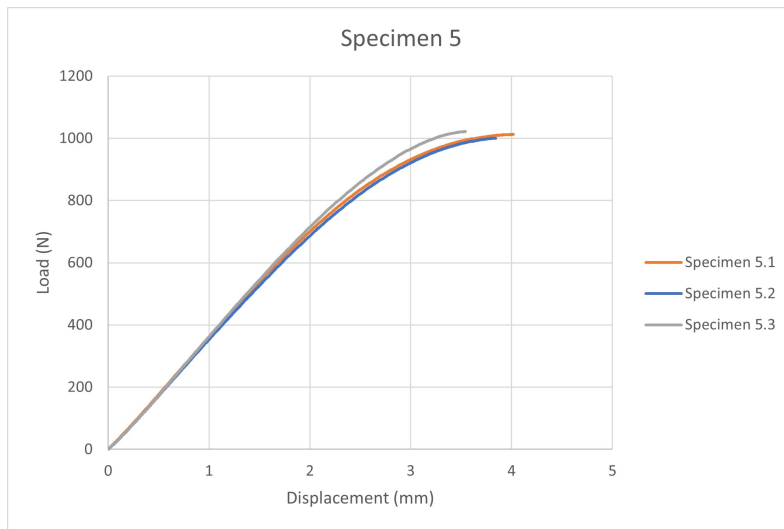


Figure 4.15: Experimental load-displacement curves of all the specimens 5

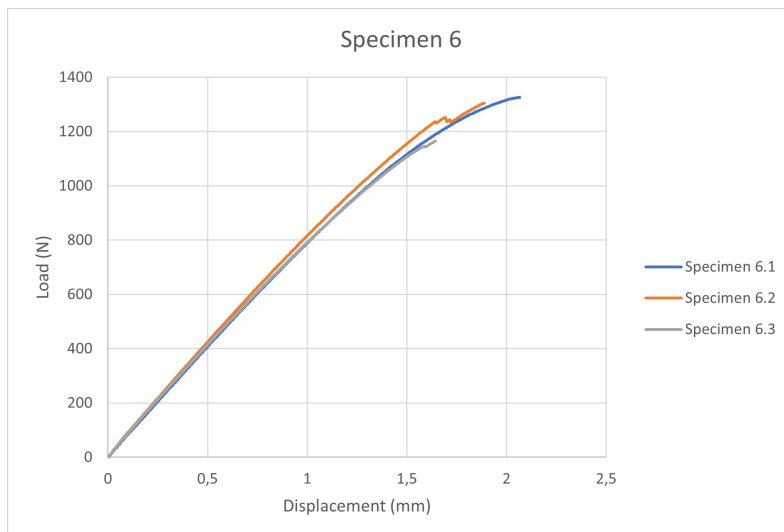


Figure 4.16: Experimental load-displacement curves of all the specimens 6

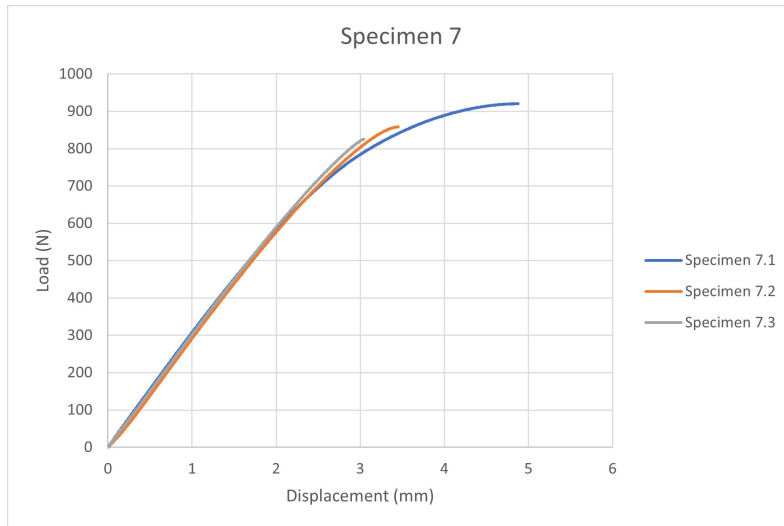


Figure 4.17: Experimental load-displacement curves of all the specimens 7

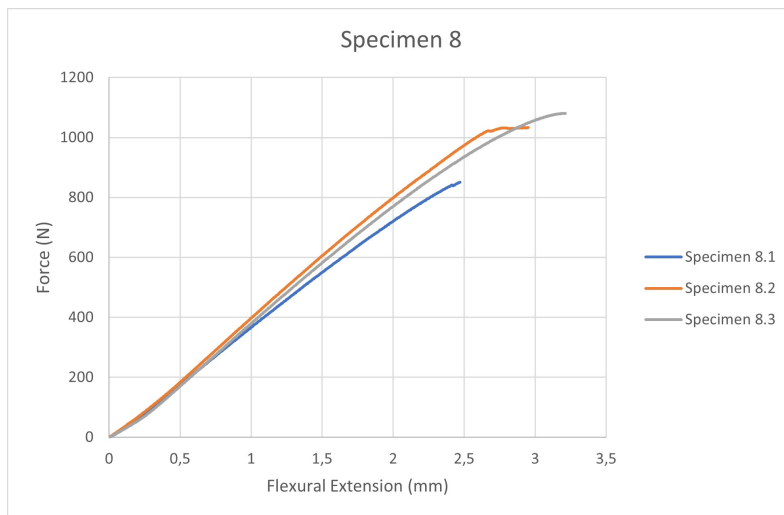


Figure 4.18: Experimental load-displacement curves of all the specimens 8

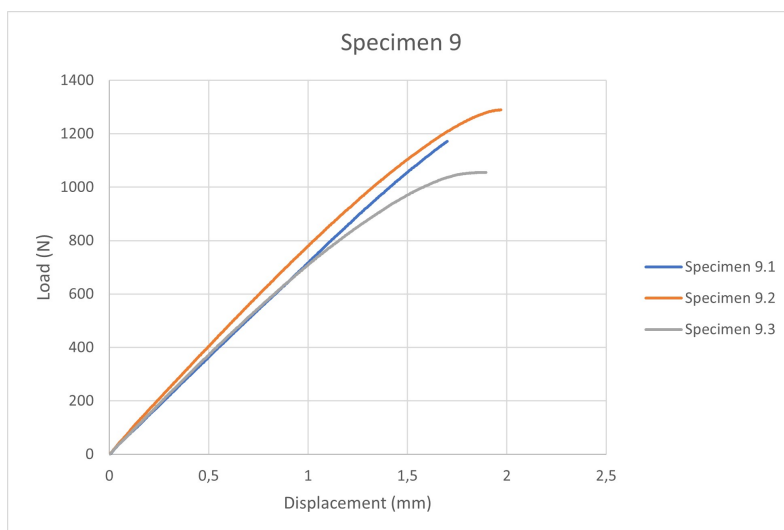


Figure 4.19: Experimental load-displacement curves of all the specimens 9

Table 4.5: Experimental results, specifically the force applied to the top roller, the stiffness and the absorbed energy by the specimens until the fracture

Specimen	Displacement (mm)	Maximum Load (N)	Stiffness K (N/mm)	Absorbed Energy (J)
1.1	5.68	674.19	182.16	2.43
1.2	6.23	746.13	183.47	2.88
1.3	5.85	690.68	177.08	2.55
Average 1	5.92 ± 0.15	703.67 ± 21.23	180.90 ± 1.91	2.62 ± 0.13
2.1	4.11	817.83	286.12	2.10
2.2	5.75	909.28	270.48	3.36
2.3	3.97	734.55	266.51	1.79
Average 2	4.61 ± 0.57	820.55 ± 44.36	274.37 ± 5.88	2.42 ± 0.47
3.1	2.88	855.77	402.63	1.48
3.2	1.98	820.01	465.91	0.89
3.3	2.23	797.37	457.46	1.02
Average 3	2.36 ± 0.26	824.38 ± 15.69	442.00 ± 19.69	1.13 ± 0.17
4.1	4.97	528.48	173.65	1.71
4.2	4.94	514.41	179.83	1.72
4.3	4.01	525.26	165.79	1.22
Average 4	4.64 ± 0.31	522.72 ± 4.15	173.09 ± 3.65	1.55 ± 0.16
5.1	4.02	1012.87	367.49	2.54
5.2	3.84	1000.33	360.77	2.33
5.3	3.54	1021.74	376.26	2.11
Average 5	3.80 ± 0.13	1011.65 ± 5.66	368.17 ± 4.04	2.33 ± 0.11
6.1	2.07	1326.36	807.89	1.59
6.2	1.89	1305.22	831.18	1.40
6.3	1.64	1165.56	814.22	1.05
Average 6	1.87 ± 0.11	1265.71 ± 50.08	817.76 ± 6.71	1.34 ± 0.15
7.1	4.88	921.03	301.77	2.94
7.2	3.45	858.58	304.16	1.65
7.3	3.04	825.48	303.76	1.35
Average 7	3.79 ± 0.54	868.36 ± 26.33	303.23 ± 0.72	1.98 ± 0.48
8.1	2.47	850.73	385.44	1.10
8.2	2.95	1032.90	425.83	1.69
8.3	3.21	1081.00	417.44	1.91
Average 8	2.88 ± 0.20	988.21 ± 68.74	409.57 ± 12.06	1.57 ± 0.24
9.1	1.70	1171.15	722.98	1.03
9.2	1.97	1289.35	784.47	1.45
9.3	1.90	1055.66	741.98	1.20
Average 9	1.86 ± 0.08	1172.05 ± 58.65	749.81 ± 17.33	1.23 ± 0.11

4.2.1 Failure Observations

After performing all the experimental procedures, it was noticed that the specimens had three distinct primary fracture modes. In some cases, even some specimens of the same type would have different fracture modes. The first fracture mode was characterized by the failure of the struts. In this fracture mode, the struts fail under pressure but tend to return to their original position (touching but not connected to each other). Once the load is alleviated, the fracture of the struts is not easily perceptible without re-applying the load. The second fracture mode was characterized by failure in the connection between the struts and the top skin. It is important to mention that in this failure mode there was not any failure between the struts and the bottom skin. Finally, the third and last failure mode is a mixed fracture mode, where none of the previously mentioned fracture modes were dominant. The specimens that fractured according to this mixed fracture mode had a total rupture of struts and skins in its mid-plane, just below where the top roller of the 3PB test was positioned. None of the fracture modes mentioned invalidates the existence of other fracture modes in the same specimen. Examples of these different fracture modes can be seen from figure 4.20 to figure 4.22. In table 4.6, we can see the specimens grouped according to their primary fracture mode.

Table 4.6: Specimens grouped according to their fracture modes. Mode 1 corresponds to the failure of the struts; mode 2 corresponds to failure in the connection between the struts and top skin; mode 3 corresponds to mixed failure mode

Radius (mm)	Relative Density	Primary Fracture Mode		
		Mode 1	Mode 2	Mode 3
0.8	0.35		1.3	1.1 and 1.2
	0.3	2.1, 2.2 and 2.3		
	0.25	3.1 and 3.2	3.3	
0.92	0.35		4.3	4.1 and 4.2
	0.3		5.1, 5.2 and 5.3	
	0.25	6.1, 6.2 and 6.3		
1.1	0.35		7.3	7.1 and 7.2
	0.3	8.1, 8.2 and 8.3		
	0.25		9.1, 9.2 and 9.3	

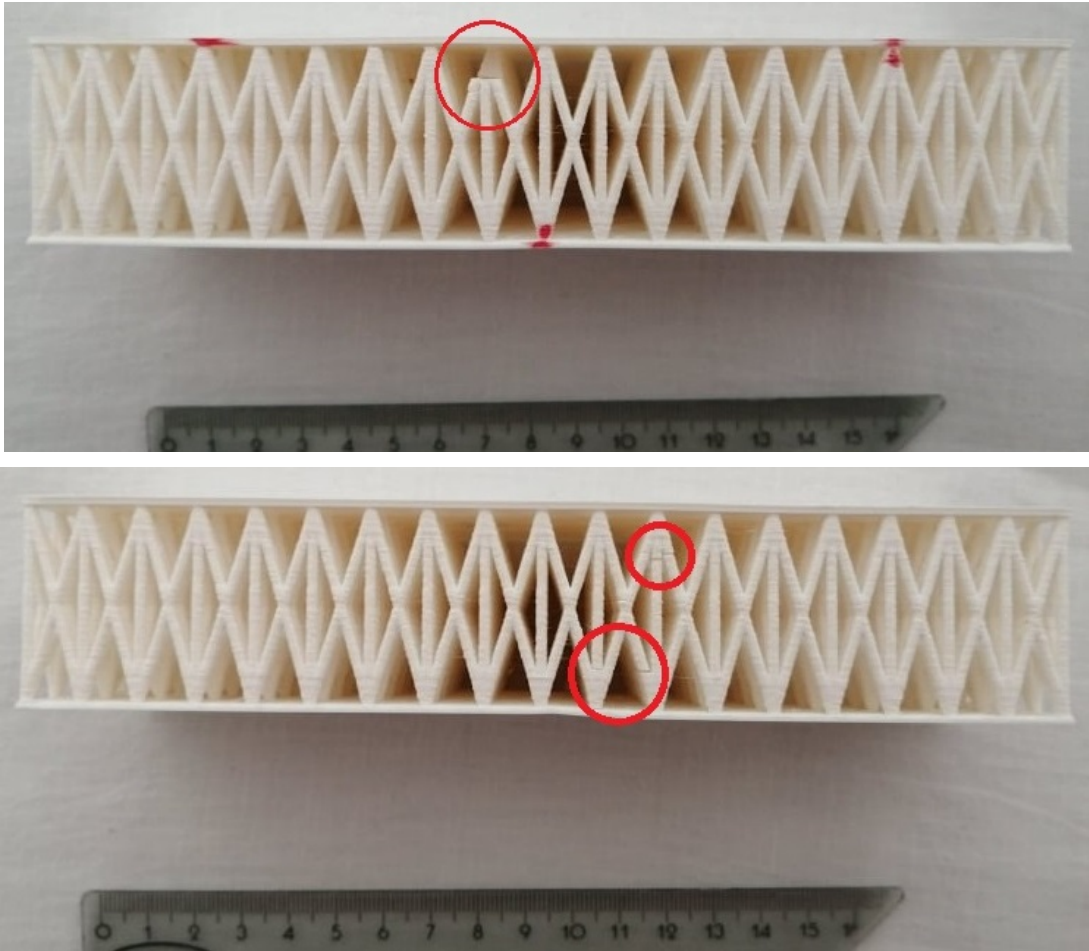


Figure 4.20: First fracture mode - Failure of the struts. The red circles highlight the failure of the struts.

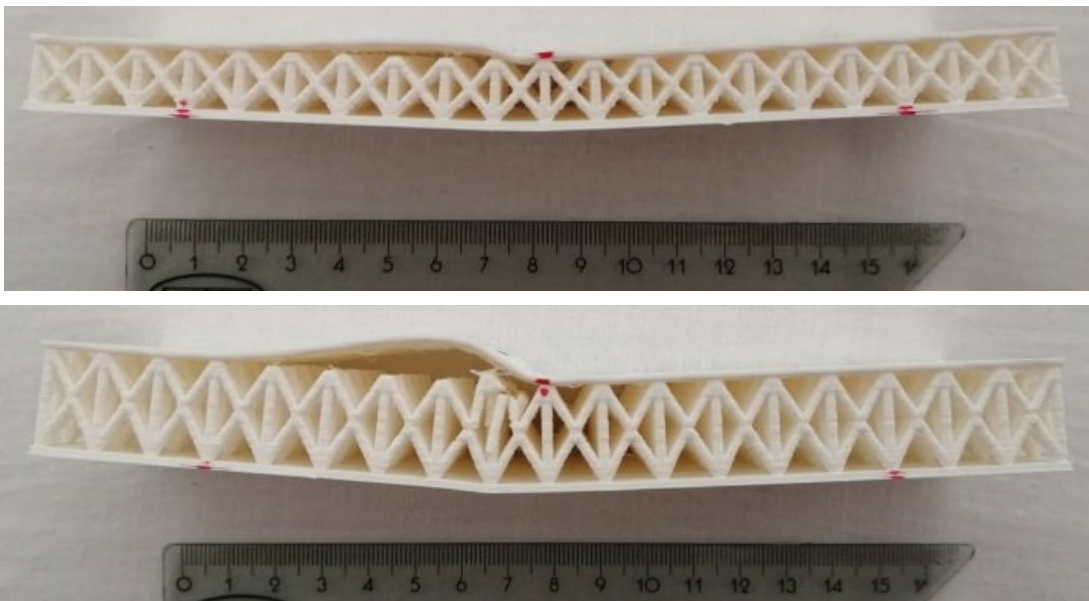


Figure 4.21: Second fracture mode - Failure of the connection between the struts and the top skin.

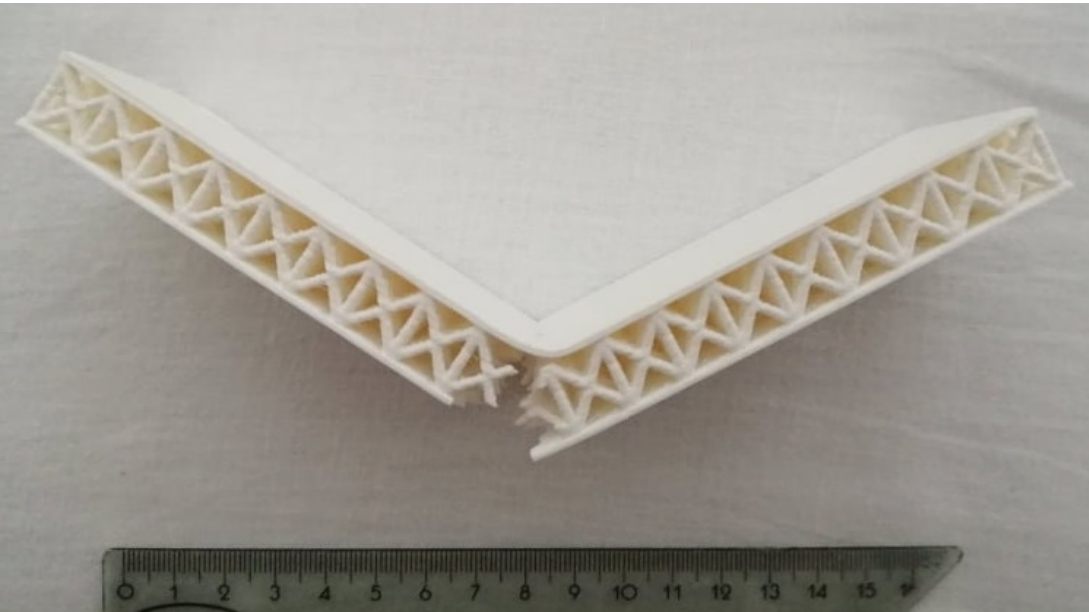
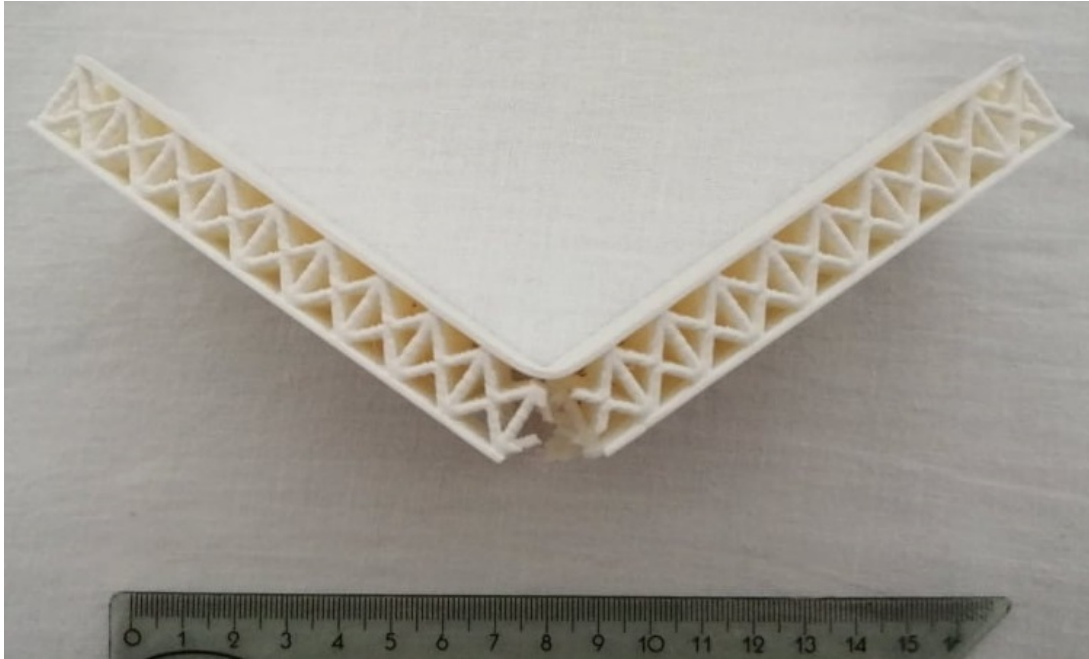


Figure 4.22: Third fracture mode - Mixed failure mode with total rupture of struts and skins in its mid-plane.

4.3 Comparison between methods

Observing all the specimens after the 3PB and their corresponding load-displacement curves, one can draw conclusions regarding the type of fracture. Regarding the observation of the specimens, there was only permanent deformation in the skins which fractured with the failure mode 2 (see section 4.2.1). Looking now at the load-displacement curves, all present a larger elastic than plastic deformation zone, with some a neglectful plastic deformation zone (specimen 8, for example). Because of this, one can conclude that the elastic behaviour prevails. So, a linear elastic numerical analysis is the best method compare with the experimental work and it was the method used.

In order to have a valid analysis, the results of the numerical simulation presented were calculated using using the average displacement from table 4.5. From figure 4.23 to figure 4.31, the comparisons between the experimental load-displacement curves and the numerical simulations are presented. Comparing the experimental and numerical load-displacement curves, the numerical results are consistent with the results obtained from the experimental procedure, specially when analysing the elastic deformation zone.

The main parameters of this thesis are the applied force, the stiffness and the energy absorption. The experimental and numerical results can be observed in table 4.7 and in table 4.8. As it was done before, in order to better analyse and compare the results, the data was re-arranged, depending on the variable. In table 4.7 the specimens are grouped by their strut radius in order to compare the effects of the relative density; in table 4.8 the specimens are grouped by their relative density in order to compare the effects of the strut radius. All the numerical results presented in said table are calculated using the average rupture displacement from the experimental tests.

Comparing first the results for specimens with the same strut radius but different relative densities, interesting conclusions arise. To do this comparison, one should use the table 4.7 as the specimens there are grouped by strut radius (specimens 1, 2 and 3 have a strut radius of 0.8 mm; specimens 4, 5 and 6 have strut a radius of 0.92 mm; specimens 7, 8 and 9 have strut a radius of 1.1 mm). Contrary to what was predicted by the numerical simulations, the experimental results suggest that a decrease in relative density does not equate to a better performance for all the parameters. Although, the experimental results almost totally agree in the numerical results regarding the influence of the relative density in the maximum load supported and stiffness of the specimen, with only the numerical load of the specimen 6 and the numerical stiffness of the specimen 9 disagreeing with this conclusion. Regarding the energy absorption, a trend is difficult to find. When the strut radius are 0.8 mm and 1.1 mm, the experimental results say that a increase of relative density leads to greater energy absorption. However, when the strut radius is 0.92 mm the experimental results present a maximum of energy absorption when the relative density is 0.3, so, for this radius, it seems that there is an optimal value or radius that results in maximum absorbed energy. The numerical results agree with the experimental results when the strut radius are 0.92 mm and 1.1 mm but when the strut radius is 0.8 mm there is a disagreement. For this radius, the numerical results have a maximum of absorbed energy when the relative density is 0.3, which is the same that happens when the strut radius is 0.92 mm.

Comparing now the results for specimens with the same relative density but different strut radius. To do this comparison, one should use the table 4.8 as the specimens there are grouped by their relative density (specimens 1, 4 and 7 have a relative density of 0.25; specimens 2, 5 and 8 have a relative density of 0.3; specimens 3, 6 and 9 have a relative density of 0.25). For the variation of radius it is more difficult to find a trend with the measured parameters. Looking firstly at the loads measured, when the relative density is 0.35 there is minimum of loads supported when the radius is 0.92 mm but when the relative density is 0.3 or 0.25 a maximum of loads supported appears at the same radius of 0.92 mm, which points to the existence of an optimal value of radius that leads to larger loads supported. The numerical results only agree with the experimental results for the specimens with relative density of 0.3. When the relative density is 0.35, the numerical results say that an increase of radius leads to an increase of loads supported but for relative densities of 0.25 a minimum of loads supported is registered when the radius is 0.92 mm.

Regarding the stiffness, experimental and numerical results are in agreement, except for the specimen 4. When the relative density is 0.35 or 0.3, an increase in radius leads to an increase in stiffness (again, except for the specimen 4) but when the relative density is 0.25 a maximum of stiffness appears when the strut radius is 0.92 mm.

Finally, observing the absorbed energy, there is a slight disagreement between the results. Almost all the numerical results say that an increase in strut radius leads to smaller absorbed energy, with only the absorbed energy measured for the specimen 6 disagreeing with this conclusion. The experimental results are a bit harder to analyze. When the relative density is 0.35 there is a minimum of absorbed energy when the radius is 0.92 mm. For the relative density of 0.3 is concluded that an increase in strut radius leads to smaller absorbed energy, which is the same conclusion that was obtained from the numerical results, For the relative density of 0.25 there is a maximum of absorbed energy when the strut radius is 0.92 mm.

Table 4.7: Values of the rupture displacement (d_{Fail}), maximum load (Load), stiffness (k) and energy absorption (E) from the numerical and experimental results. "Num" and "Exp" refer to numerical and experimental values, respectively. All the experimental values presented are averages of the values of each specimen. All the numerical values were calculated using the average rupture displacement. In this table the specimens are grouped according to the strut radius (specimens 1, 2 and 3 have a strut radius of 0.8 mm; specimens 4, 5 and 6 have strut a radius of 0.92 mm; specimens 7, 8 and 9 have strut a radius of 1.1 mm).

Specimen	d_{Fail} (mm)	Load Num (N)	Load Exp (N)	K Num (N/mm)	K Exp (N/mm)	E_{abs} Num (J)	E_{abs} Exp (J)
1	5.92	680.08	703.67	114.27	180.90	2.01	2.62
2	4.61	987.63	820.55	213.49	274.37	2.27	2.42
3	2.36	1032.56	824.38	439.24	442.00	1.22	1.13
4	4.64	691.09	522.72	148.35	173.09	1.60	1.55
5	3.80	1023.08	1011.65	268.86	368.17	1.94	2.33
6	1.84	951.90	1265.71	521.77	817.76	0.87	1.34
7	3.79	749.90	868.36	197.95	303.23	1.42	1.98
8	2.88	821.64	988.21	286.35	409.57	1.18	1.57
9	1.86	984.12	1172.05	280.94	749.81	0.91	1.23

Table 4.8: The same values of the rupture displacement (d_{Fail}), maximum load (Load), stiffness (k) and energy absorption (E) from the numerical and experimental results that were presented in table 4.7 but in this table the specimens are grouped according to their relative density (specimens 1, 4 and 7 have a relative density of 0.25; specimens 2, 5 and 8 have a relative density of 0.3; specimens 3, 6 and 9 have strut a relative density of 0.25).

Specimen	d_{Fail} (mm)	Load Num (N)	Load Exp (N)	K Num (N/mm)	K Exp (N/mm)	E_{abs} Num (J)	E_{abs} Exp (J)
1	5.92	680.08	703.67	114.27	180.90	2.01	2.62
4	4.64	691.09	522.72	148.35	173.09	1.60	1.55
7	3.79	749.90	868.36	197.95	303.23	1.42	1.98
2	4.61	987.63	820.55	213.49	274.37	2.27	2.42
5	3.80	1023.08	1011.65	268.86	368.17	1.94	2.33
8	2.88	821.64	988.21	286.35	409.57	1.18	1.57
3	2.36	1032.56	824.38	439.24	442.00	1.22	1.13
6	1.84	951.90	1265.71	521.77	817.76	0.87	1.34
9	1.86	984.12	1172.05	280.94	749.81	0.91	1.23

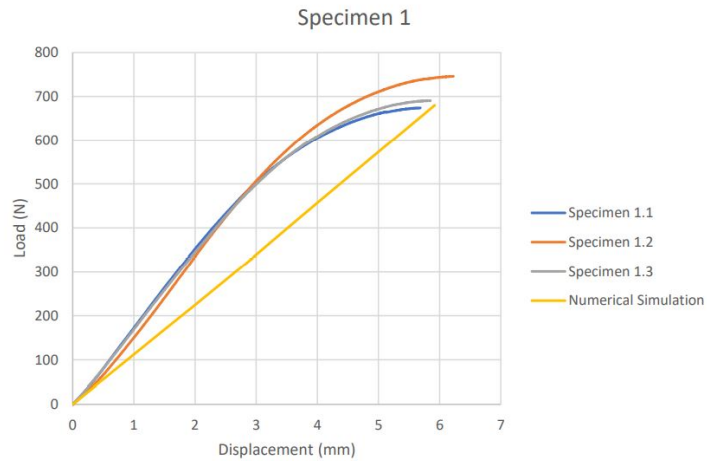


Figure 4.23: Comparison between the experimental load-displacement curves and the numerical simulation of specimen 1

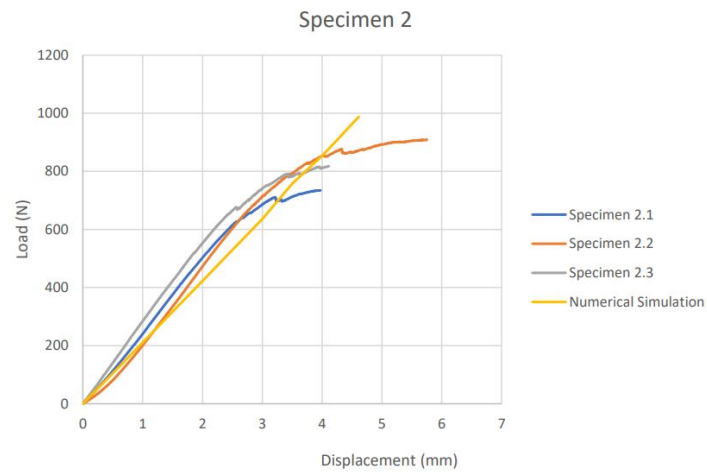


Figure 4.24: Comparison between the experimental load-displacement curves and the numerical simulation of specimen 2

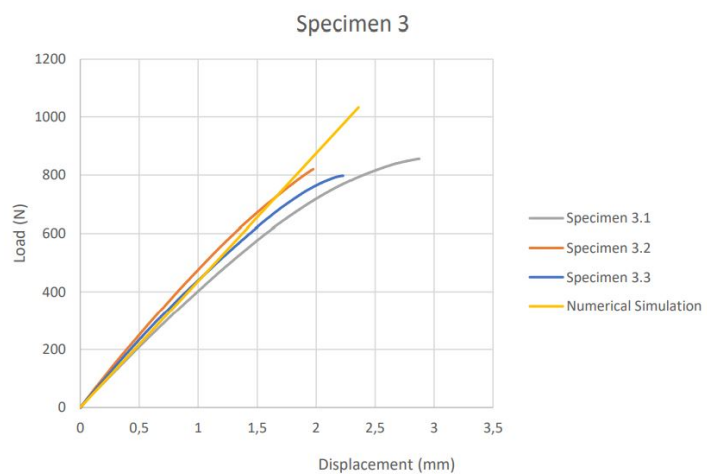


Figure 4.25: Comparison between the experimental load-displacement curves and the numerical simulation of specimen 3

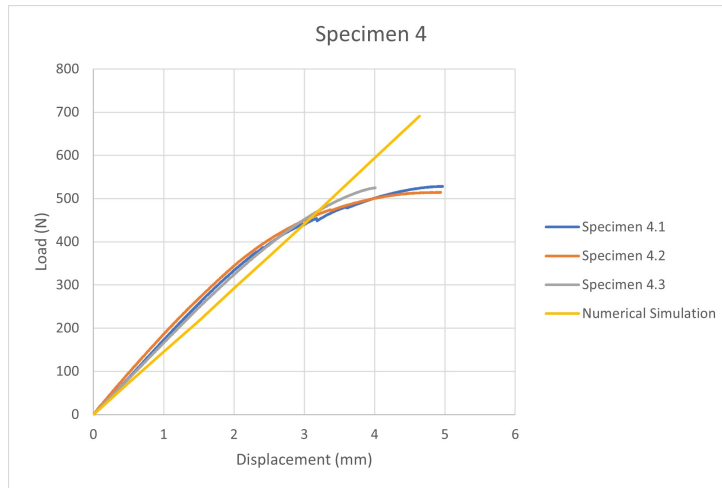


Figure 4.26: Comparison between the experimental load-displacement curves and the numerical simulation of specimen 4

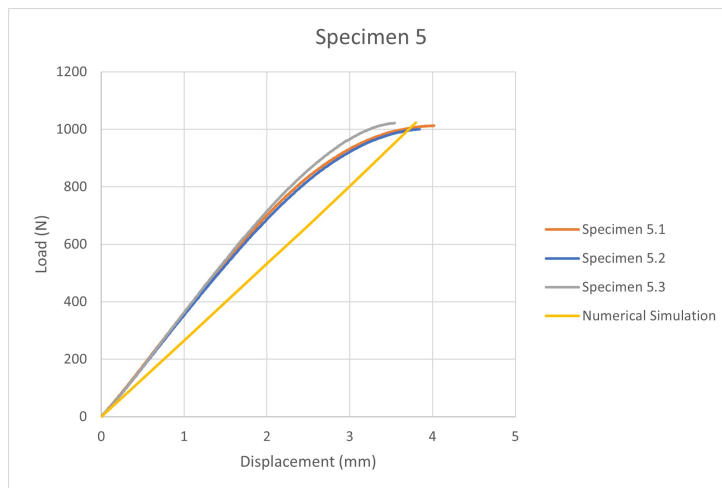


Figure 4.27: Comparison between the experimental load-displacement curves and the numerical simulation of specimen 5

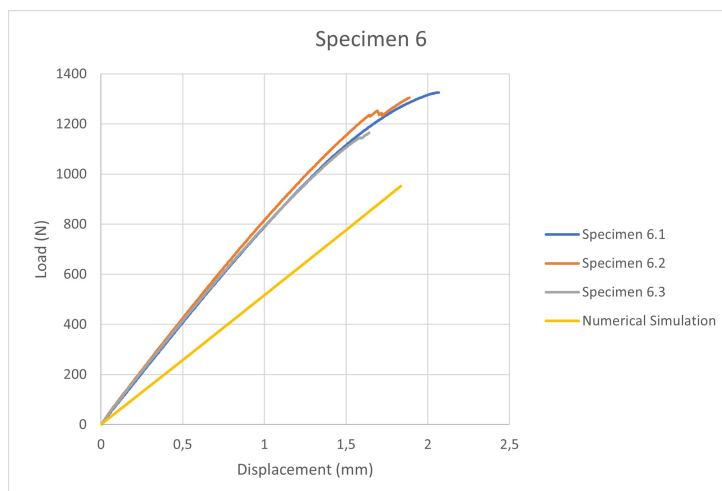


Figure 4.28: Comparison between the experimental load-displacement curves and the numerical simulation of specimen 6

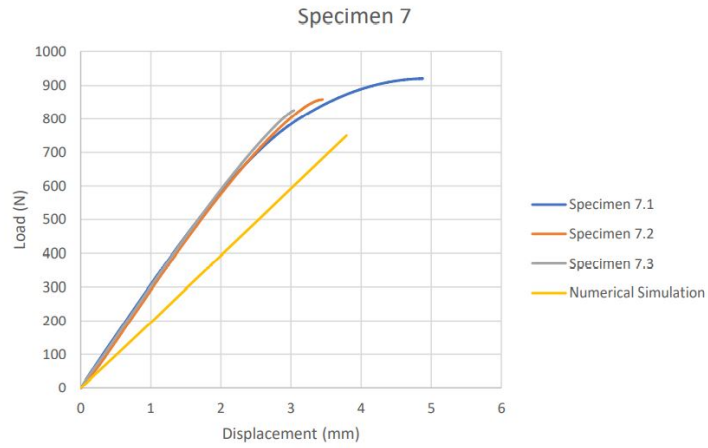


Figure 4.29: Comparison between the experimental load-displacement curves and the numerical simulation of specimen 7

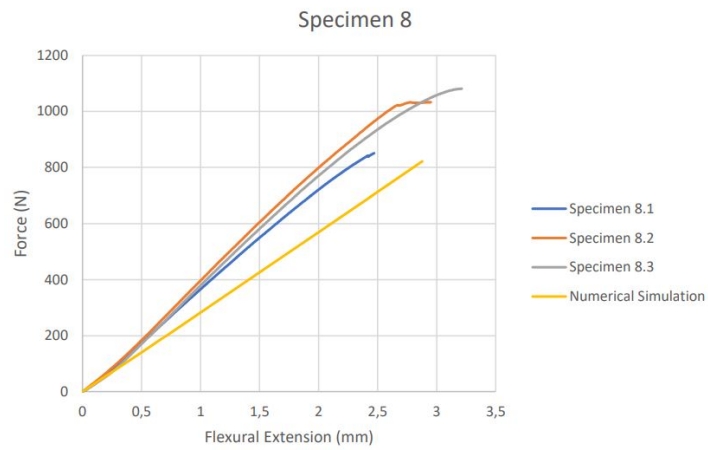


Figure 4.30: Comparison between the experimental load-displacement curves and the numerical simulation of specimen 8

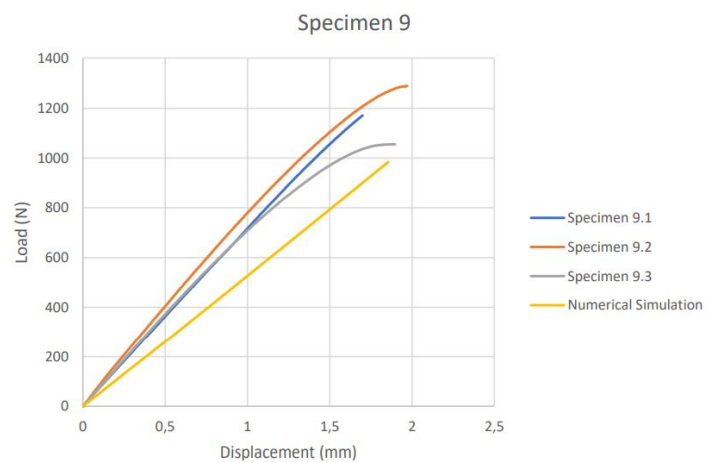


Figure 4.31: Comparison between the experimental load-displacement curves and the numerical simulation of specimen 9

Chapter 5

Conclusions

5.1 Achievements

In this thesis, nine sandwich panels were designed with a unit cell inspired by the crystalline structures with cubic arrangements. The unit cell used was a body and face centered unit cell with z-struts. The differences between the nine unit cells and consequently between the sandwich panels, were the radius of the struts and the relative density of the unit cell. Experimental tests and numerical simulations were used to analyse the mechanical response and failure behaviour of all the cores when subjected to three-point bending tests.

For the most part, the same tendency was found in the data obtained of the experimental tests and in the FEA. The load-displacement curves from the experimental tests are consistent with the data gathered from the numerical simulations, specially with the FEA that used less simplifications of the model. From this, we can conclude that all the specimens have brittle fracture and the elastic behaviour prevails. So, the linear numerical analysis used is the best method to compare the results.

As two parameters were varied for this study, we must analyse the effects of the variation individually.

Comparing the results of the variation of the relative density for structures with the same strut radius, the experimental results and numerical simulations point to the conclusion that a decrease of the relative density would lead to higher strength and stiffness. Regarding the energy absorption, the variation of relative density of structures with the same radius showed no clear trend that could be associated with the variation of relative density.

Comparing now the results of the variation of the radius of the struts for structures with the same relative density, there is not a good agreement between numerical and experimental results. Using the numerical results, it is difficult to find a trend because there rarely is an agreement between the effect of the said variation at the various values of relative density. On the other hand, the experimental results are more dispersed more consistent. These results suggest that at higher values of relative density there is a strut radius that results in minimum value of strength and stiffness. However, at lower values of relative density, there is a strut radius that results in maximum value of strength and stiffness. For the average values of relative density, the best results for strength and stiffness are found with different

values of strut radius. This leads to the conclusion the effects of the variation of the strut radius are different for different values of relative density. Regarding the the energy absorption, the experimental results show no clear trend when varying the strut radius for structures with the same relative density.

5.2 Future Work

Future work on this topic should consist in the search for new lattice topology and the improvement of the BCFZ topology used in order to create a structures that surpass the properties of the conventional hexagonal honeycomb structure.

The first could be achieved with a numerical topology optimization study. This would provide an alternative to the crystalline structures previously used. Due to the design freedom provided by the 3D printing method, an abundance of new topology can be created.

Due to the different failure modes encountered during this study, a future work made to develop of a failure map to predict the failure mode depending on the characteristic of the structures.

Finally, in order to create more accurate numerical simulations, a future work on the influence of the simplification of the numerical simulations should be conducted.

Bibliography

- [1] A. C. F. on Additive Manufacturing Technologies and A. C. F. on Additive Manufacturing Technologies. Subcommittee F42. 91 on Terminology. *Standard terminology for additive manufacturing technologies*. Astm International, 2012.
- [2] H. Y. Sarvestani, A. Akbarzadeh, A. Mirbolghasemi, and K. Hermenean. 3d printed meta-sandwich structures: Failure mechanism, energy absorption and multi-hit capability. *Materials & Design*, 160: 179–193, 2018.
- [3] TotalMateria. Sandwich steel panels: Part one. in: Total Materia Website (2017), <https://www.totalmateria.com/page.aspx?ID=CheckArticlesite=ktsLN=PTNM=484> Accessed: 2020-12-08.
- [4] H. Araújo, M. Leite, A. Ribeiro, A. Deus, L. Reis, and M. F. Vaz. The effect of geometry on the flexural properties of cellular core structures. *Proceedings of the Institution of Mechanical Engineers, Part L: Journal of Materials: Design and Applications*, 233(3):338–347, 2019.
- [5] J. Monteiro, M. Sardinha, F. Alves, A. Ribeiro, L. Reis, A. Deus, M. Leite, and M. F. Vaz. Evaluation of the effect of core lattice topology on the properties of sandwich panels produced by additive manufacturing. *Proceedings of the Institution of Mechanical Engineers, Part L: Journal of Materials: Design and Applications*, 2020.
- [6] M. F. Ashby. The properties of foams and lattices. *Philosophical Transactions of the Royal Society A: Mathematical, Physical and Engineering Sciences*, 364(1838):15–30, 2006.
- [7] T. Bitzer. Honeycomb technology: materials, design, manufacturing, applications and testing. *Springer Science & Business Media*, 1997.
- [8] Y. Li and Z. Jin. Free flexural vibration analysis of symmetric rectangular honeycomb panels with scsc edge supports. *Composite structures*, 83(2):154–158, 2008.
- [9] C. Foo, L. Seah, and G. B. Chai. Low-velocity impact failure of aluminium honeycomb sandwich panels. *Composite Structures*, 85(1):20–28, 2008.
- [10] A. Francesconi, D. Pavarin, A. Bettella, C. Giacomuzzo, M. Farud, R. Destefanis, M. Lambert, and F. Angrilli. Generation of transient vibrations on aluminum honeycomb sandwich panels subjected to hypervelocity impacts. *International Journal of Impact Engineering*, 35(12):1503–1509, 2008.

- [11] L. Yongqiang and Z. Dawei. Geometrically nonlinear forced vibrations of the symmetric honeycomb sandwich panels affected by the water. *Composite structures*, 93(2):880–888, 2011.
- [12] J. Fatemi and M. Lemmen. Effective thermal/mechanical properties of honeycomb core panels for hot structure applications. *Journal of Spacecraft and Rockets*, 46(3):514–525, 2009.
- [13] X. Li, P. Zhang, Z. Wang, G. Wu, and L. Zhao. Dynamic behavior of aluminum honeycomb sandwich panels under air blast: Experiment and numerical analysis. *Composite Structures*, 108:1001–1008, 2014.
- [14] T. Koda and T. Matsuda. Analysis of elastic-viscoplastic behavior of honeycomb sandwich panels based on a homogenization theory for free edge analysis. In *Key Engineering Materials*, volume 535, pages 357–360. Trans Tech Publ, 2013.
- [15] A. Petras and M. Sutcliffe. Failure mode maps for honeycomb sandwich panels. *Composite structures*, 44(4):237–252, 1999.
- [16] S. M. Lee and T. K. Tsotsis. Indentation failure behavior of honeycomb sandwich panels. *Composites science and technology*, 60(8):1147–1159, 2000.
- [17] D. Horrigan and R. Staal. Predicting failure loads of impact damaged honeycomb sandwich panels—a refined model. *Journal of Sandwich Structures & Materials*, 13(1):111–133, 2011.
- [18] R. Staal, G. Mallinson, K. Jayaraman, and D. Horrigan. Predicting failure loads of undamaged sandwich honeycomb panels subject to bending. *Journal of Sandwich Structures & Materials*, 11(2-3):73–104, 2009.
- [19] M. F. Ashby and L. J. Gibson. Cellular solids: structure and properties. *Press Syndicate of the University of Cambridge, Cambridge, UK*, pages 175–231, 1997.
- [20] AdditiveManufacturing. Am basics. in: Additive Manufacturing Website (2020), <https://additivemanufacturing.com/basics/> Accessed 2020-12-09.
- [21] J. Go, S. N. Schiffres, A. G. Stevens, and A. J. Hart. Rate limits of additive manufacturing by fused filament fabrication and guidelines for high-throughput system design. *Additive Manufacturing*, 16: 1–11, 2017.
- [22] S. Jiang. *Processing rate and energy consumption analysis for additive manufacturing processes: Material extrusion and powder bed fusion*. PhD thesis, Massachusetts Institute of Technology, 2017.
- [23] J. Fernandes, A. M. Deus, L. Reis, M. F. Vaz, and M. Leite. Study of the influence of 3d printing parameters on the mechanical properties of pla. 2018.
- [24] C. M. Vicente, T. S. Martins, M. Leite, A. Ribeiro, and L. Reis. Influence of fused deposition modeling parameters on the mechanical properties of abs parts. *Polymers for Advanced Technologies*, 31(3):501–507, 2020.

- [25] L. Long. 3d printing is poised to continue outpacing growth of traditional manufacturing. in: engineering.com website (2018), <https://www.engineering.com/AdvancedManufacturing/ArticleID/16873/3D-Printing-Is-Poised-to-Continue-Outpacing-Growth-of-Traditional-Manufacturing.aspx> Accessed 2020-12-30.
- [26] T. Wohlers, T. Caffrey, et al. 3d printing and additive manufacturing: State of the industry annual worldwide progress report. *Wohlers report*, 2014.
- [27] T. Gutowski, S. Jiang, D. Cooper, G. Corman, M. Hausmann, J.-A. Manson, T. Schudeleit, K. Wegener, M. Sabelle, J. Ramos-Grez, et al. Note on the rate and energy efficiency limits for additive manufacturing. *Journal of Industrial Ecology*, 21(S1):S69–S79, 2017.
- [28] A. B. Varotsis. Introduction to fdm 3d printing. in: 3D Hubs Website, <https://www.3dhubs.com/knowledge-base/introduction-fdm-3d-printing/> Accessed 2020-12-09.
- [29] D. Chakravorty. Stl file format (3d printing) – simply explained. in: All3DP Website (2019), <https://all3dp.com/what-is-stl-file-format-extension-3d-printing/> Accessed 2020.12.09.
- [30] A. Blog. Fdm – fused deposition modeling (or fff, pjp, lpd). in: Additive Blog Website (2020), <https://www.additive.blog/knowledge-base/3d-printers/fdm-fused-deposition-modeling-fff-pjp-lpd/> Accessed 2020-12-11.
- [31] D. Pros. Choosing infill percentage for 3d printed parts. in: 3D Pros Website (2020), <https://www.3d-pros.com/choosing-infill-for-3d-printed-parts> Accessed 2020-12-11.
- [32] B. Hudson. How to design parts for fdm 3d printing. in: 3D Hubs Website, <https://www.3dhubs.com/knowledge-base/how-design-parts-fdm-3d-printing/overhangs> Accessed 2020-12-11.
- [33] P. Cain. Supports in 3d printing: A technology overview. in: 3D Hubs Website (2020), <https://www.3dhubs.com/knowledge-base/supports-3d-printing-technology-overview/fdm> Accessed 2020-12-11.
- [34] Richa. The secret to amazing 3d prints lies in these slicer settings! in: Geeetech Make It Possible Website (2020), <https://www.geeetech.com/blog/2018/01/the-secret-to-amazing-3d-prints-lies-in-these-slicer-settings/> Accessed 2020-12-11.
- [35] K. Giang. Pla vs. abs: What's the difference? in: 3D Hubs Website, <https://www.3dhubs.com/knowledge-base/pla-vs-abs-whats-difference/> Accessed 2020-12-11.
- [36] S. 3D. Print quality troubleshooting guide. in: Simplify 3D Website (2020), <https://www.simplify3d.com/support/print-quality-troubleshooting/> Accessed 2020-12-11.
- [37] Filament2Print. How to create a 3d printing profile. in: Filament2Print Website, <https://filament2print.com/gb/blog/77how-+-create-+-3d-+-printing-+-profile.html> Accessed 2020-12-11.

- [38] H. M. Kolken and A. Zadpoor. Auxetic mechanical metamaterials. *RSC advances*, 7(9):5111–5129, 2017.
- [39] 3dsourced. How 3d printed shoes quietly took over the world. in: 3dsourced Website (2020), <https://3dsourced.com/feature-stories/3d-printed-shoes/Adidas> Accessed 2020-12-10.
- [40] B. Dunne. These 3d-printed sneakers are nike’s next big step forward. in: Sole Collector Website (2018), <https://solecollector.com/news/2018/04/nike-flyprint-3d-printed-zoom-vaporfly-elite-sneaker-review> Accessed 2020-12-10.
- [41] H. Watkin. Reebok launches 3d printed shoe called the liquid floatride run. in: All3DP Website (2018), <https://all3dp.com/reebok-launches-latest-3d-printed-shoe-called-liquid-floatride-run/> Accessed 2020-12-10.
- [42] Humble and Rich. Adidas futurecraft 4d sneakers review. in: Humble and Rich Website, <https://boutique.humbleandrich.com/adidas-futurecraft-4d-sneakers-review/> Accessed 2020-12-10.
- [43] Branch technology. in: Branch Technology Website (2020), <https://www.branch.technology/> Accessed 2020-12-09.
- [44] T. Vialva. Scan the world’s jonathan beck at the statens museum for kunst, national gallery of denmark. *3D Printing Industry*, 1:24–27, September 2019.
- [45] F. Radius. Understanding 3d printed lattices: Performance and design considerations. in: Fast Radius Website, <https://www.fastradius.com/resources/understanding-3d-printed-lattices-performance-and-design-considerations/> Accessed 2020-12-10.
- [46] B. T. Stuff. Vics zero1. in: Bless This Stuff Website, <https://www.blessthisstuff.com/stuff/wear/headwear/vics-zero1/> Accessed 2020-12-10.
- [47] Y. Li, H. Jahr, P. Pavanram, F. Bobbert, U. Puggi, X.-Y. Zhang, B. Pوران, M. Leeflang, H. Weinans, J. Zhou, et al. Additively manufactured functionally graded biodegradable porous iron. *Acta biomaterialia*, 96:646–661, 2019.
- [48] M. Mazur, M. Leary, M. McMillan, J. Elambasseril, and M. Brandt. Slm additive manufacture of h13 tool steel with conformal cooling and structural lattices. *Rapid Prototyping Journal*, 2016.
- [49] S. Limmahakhun, A. Oloyede, K. Sitthiseripratip, Y. Xiao, and C. Yan. Stiffness and strength tailoring of cobalt chromium graded cellular structures for stress-shielding reduction. *Materials & Design*, 114:633–641, 2017.
- [50] Y. Li, P. Pavanram, J. Zhou, K. Lietaert, F. Bobbert, Y. Kubo, M. Leeflang, H. Jahr, and A. Zadpoor. Additively manufactured functionally graded biodegradable porous zinc. *Biomaterials Science*, 8(9):2404–2419, 2020.
- [51] G. Qi, Y.-L. Chen, P. Richert, L. Ma, and K.-U. Schröder. A hybrid joining insert for sandwich panels with pyramidal lattice truss cores. *Composite Structures*, page 112123, 2020.

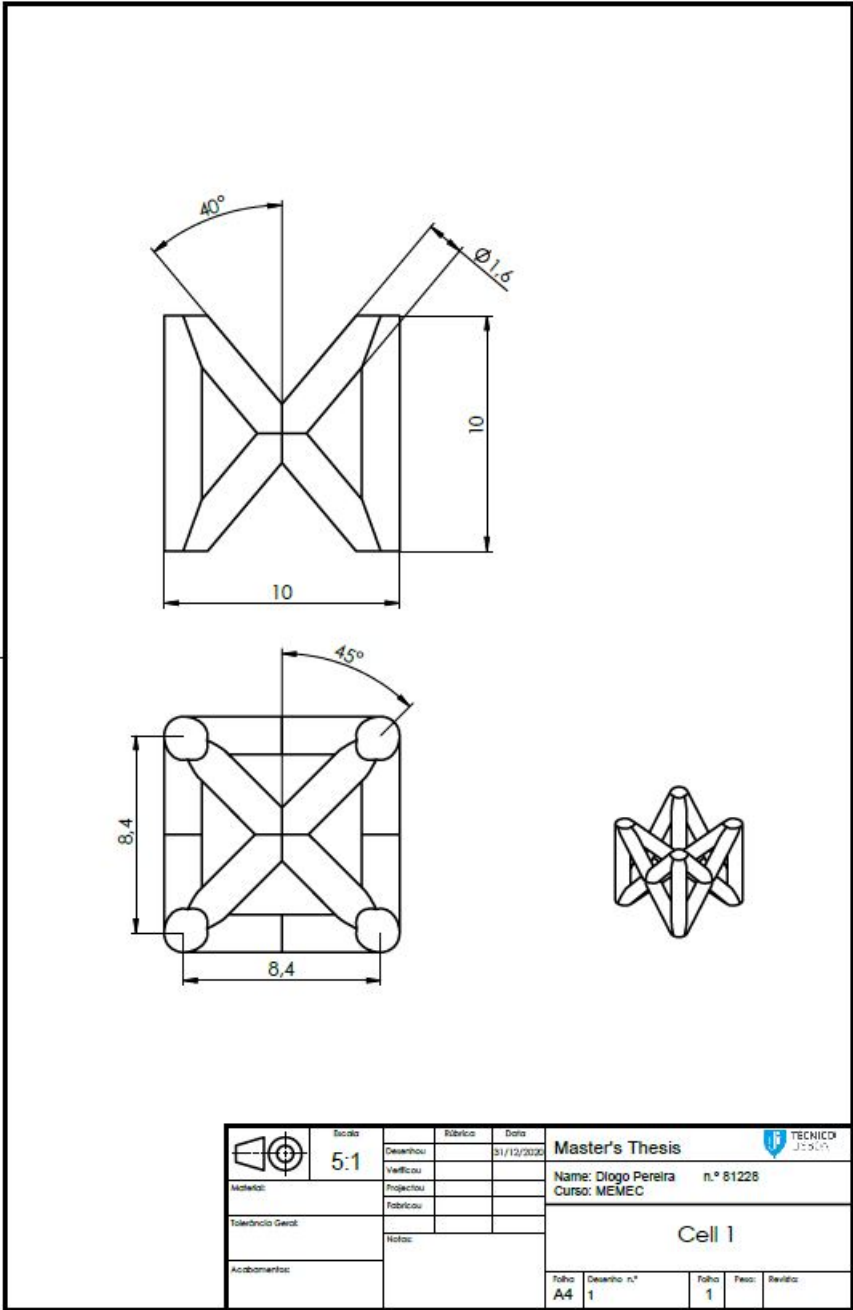
- [52] J.-H. Lim and K.-J. Kang. Mechanical behavior of sandwich panels with tetrahedral and kagome truss cores fabricated from wires. *International Journal of Solids and Structures*, 43(17):5228–5246, 2006.
- [53] M. Mohsenizadeh, F. Gasbarri, M. Munther, A. Beheshti, and K. Davami. Additively-manufactured lightweight metamaterials for energy absorption. *Materials & Design*, 139:521–530, 2018.
- [54] I. Ullah, M. Brandt, and S. Feih. Failure and energy absorption characteristics of advanced 3d truss core structures. *Materials & Design*, 92:937–948, 2016.
- [55] J. Kadkhodapour, H. Montazerian, A. C. Darabi, A. Anaraki, S. Ahmadi, A. Zadpoor, and S. Schmauder. Failure mechanisms of additively manufactured porous biomaterials: Effects of porosity and type of unit cell. *Journal of the mechanical behavior of biomedical materials*, 50: 180–191, 2015.
- [56] H.-Y. Lei, J.-R. Li, Z.-J. Xu, and Q.-H. Wang. Parametric design of voronoi-based lattice porous structures. *Materials & Design*, page 108607, 2020.
- [57] Y. Liu, Z. Dong, J. Ge, X. Lin, and J. Liang. Stiffness design of a multilayer arbitrary bcc lattice structure with face sheets. *Composite Structures*, 230:111485, 2019.
- [58] L. Gibson. Cellular solids: Structure, properties and applications. *Massachusetts Institute of Technology* (https://ocw.mit.edu/courses/materials-science-and-engineering/3-054-cellularsolids-structure-properties-and-applications-spring-2015/lecturenotes/MIT3_054S15_L2_Proc.pdf), 2015.
- [59] V. S. Deshpande and N. Fleck. Collapse of truss core sandwich beams in 3-point bending. *International journal of solids and structures*, 38(36-37):6275–6305, 2001.
- [60] H. Araújo, M. Leite, A. Ribeiro, A. M. Deus, L. Reis, and M. F. Vaz. Investigating the contribution of geometry on the failure of cellular core structures obtained by additive manufacturing. *Frattura ed Integrità Strutturale*, 13(49):478–486, 2019.
- [61] G. W. Hunt and M. A. Wadee. Localization and mode interaction in sandwich structures. In *Localization And Solitary Waves In Solid Mechanics*, pages 301–320. World Scientific, 1999.
- [62] M. F. Ashby, T. Evans, N. A. Fleck, J. Hutchinson, H. Wadley, and L. Gibson. *Metal foams: a design guide*. Elsevier, 2000.
- [63] S. Farah, D. G. Anderson, and R. Langer. Physical and mechanical properties of pla, and their functions in widespread applications—a comprehensive review. *Advanced drug delivery reviews*, 107:367–392, 2016.
- [64] D. F. P. M. Pro. 3d printer filament, pla blend. in: 3D Filkemp Print Master Pro Website (2020), <http://3dprintmasterpro.com/shop/pla-n/122-3d-printer-filament-pla-blend-285-mm-011-in-signal-white-10-kg-22-lb-5600929900716.html> Accessed 2020-12-11.

- [65] G. P. 3D. 3d print master pro pla-n by filkemp. in: Go Print 3D Website (2020), <https://www.goprint3d.co.uk/filkemp-pla-n.html> Accessed 2020-12-11.
- [66] *PLA for 3D Printing - 881N*. Filkemp, February 2018.
- [67] A. Standard. C393–00. standard test method for flexural properties of sandwich constructions, 2000.

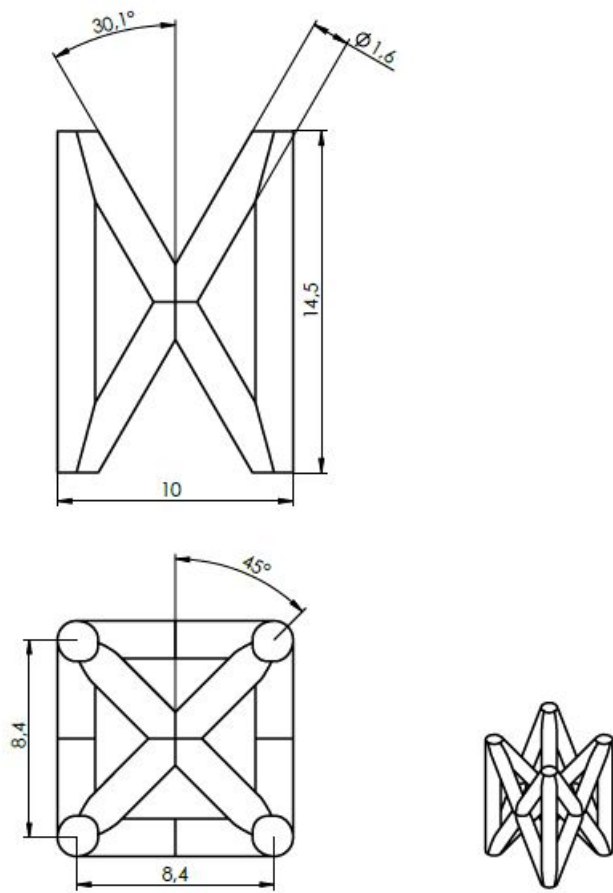
Appendix A

Technical drawings

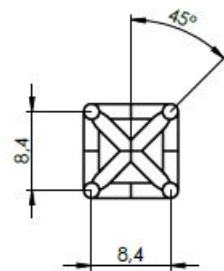
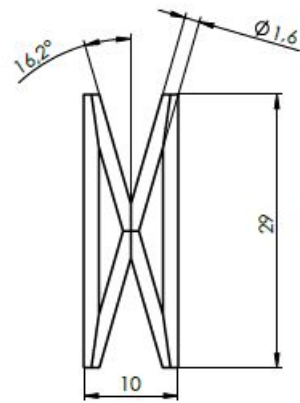
In the present appendix are included the technical drawings of all the unit cells studied in this work. These technical drawings are included in order to manufacture and reproduce the unit cells and the sandwich panels, if someone wishes to do so.





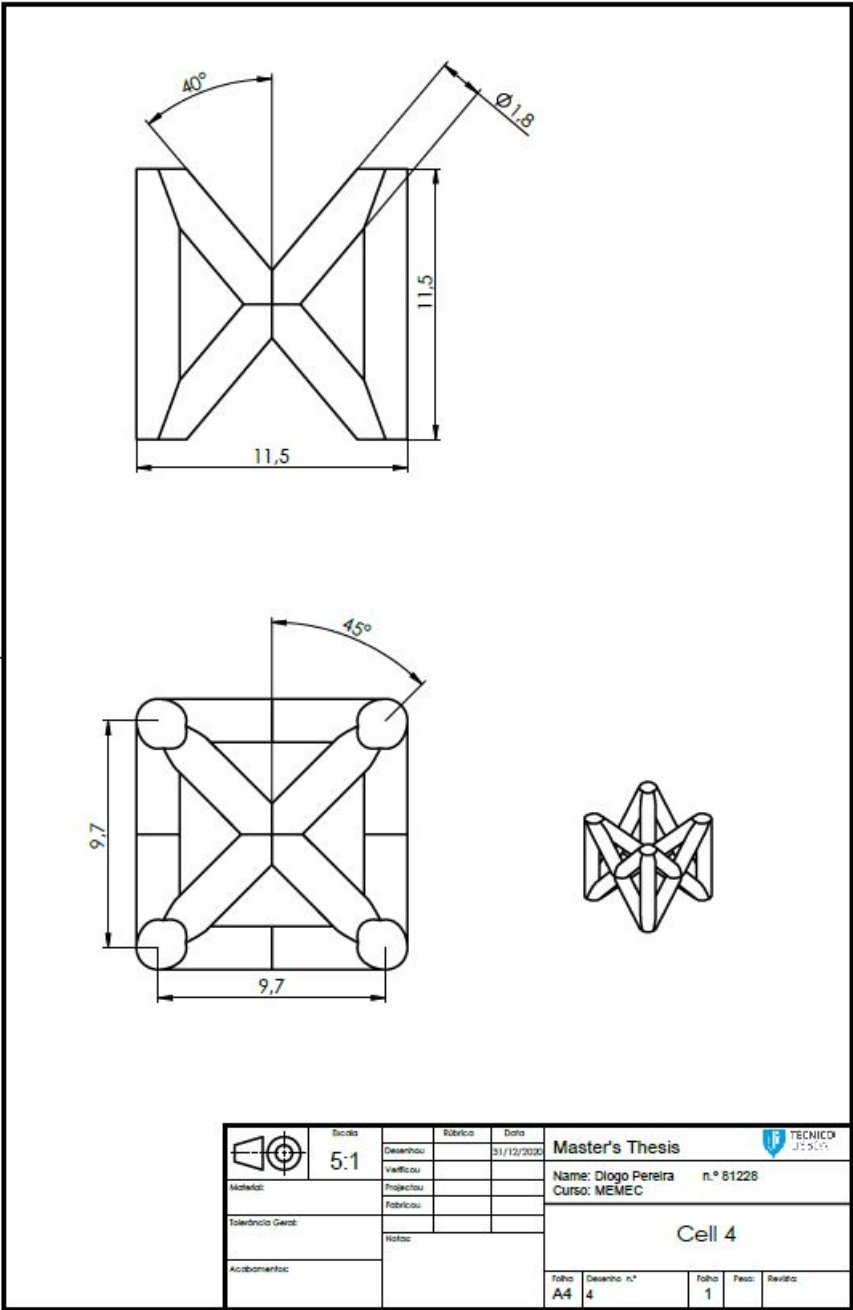
	Escala	5:1	Revisões	Data	Master's Thesis
				31/12/2020	
Material:			Projectado		Curso: MEMEC
Tolerância Geral:			Fabricado		Cell 1
Acabamentos:			Notas:		
Folha	Desenho n.º	Folha	Fase	Revisão	
A4	1	1			



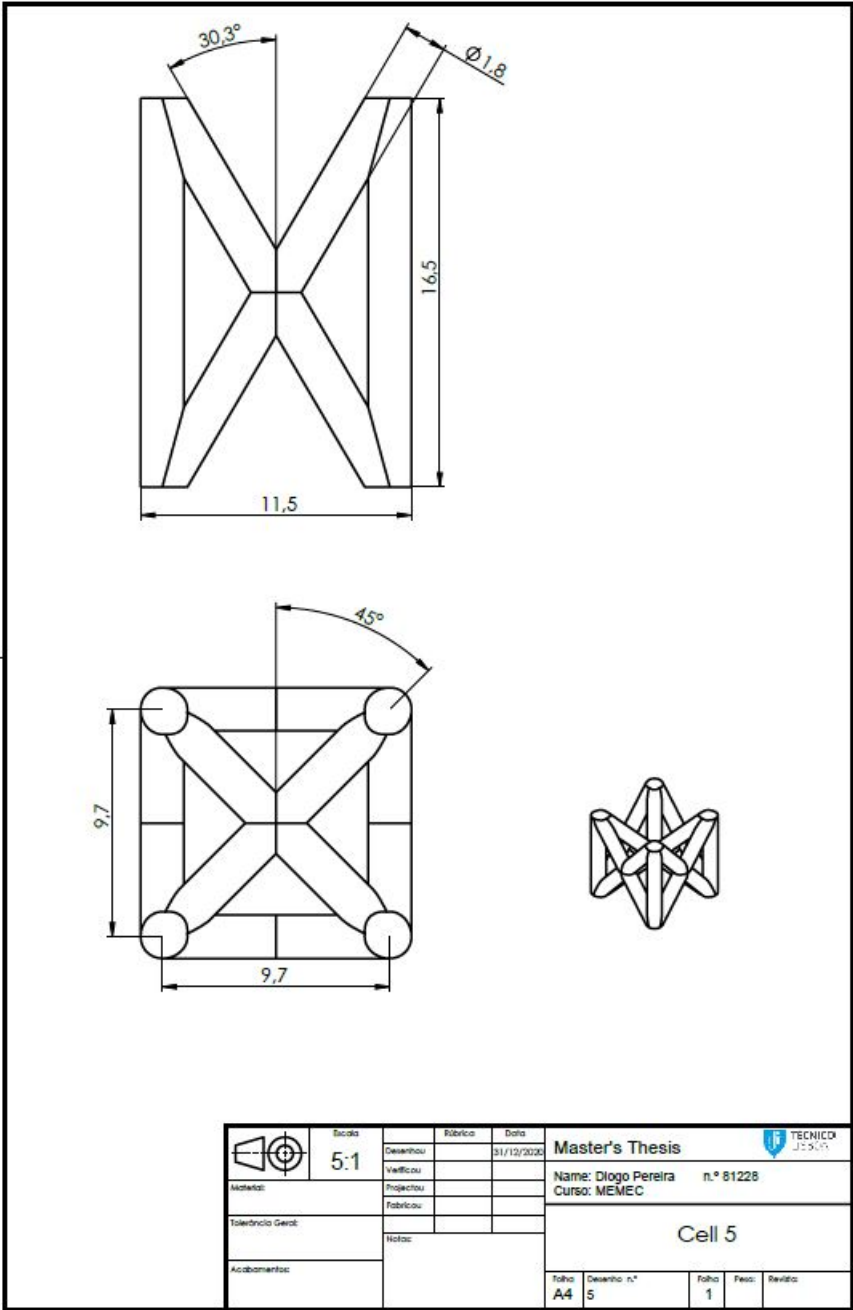
	Escala	5:1	Desenhado		Data	31/12/2020	Master's Thesis		
	Verificado		Projectado		Nome: Diogo Pereira	n.º 81228			
Material:			Fabricado		Curso: MEMEC		Cell 2		
Tolerância Geral:			Notas:						
Acabamentos:					Folha	Desenho n.º	Folha	Fase	Revisão
					A4	2	1		



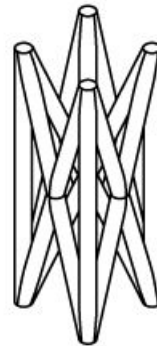
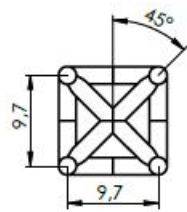
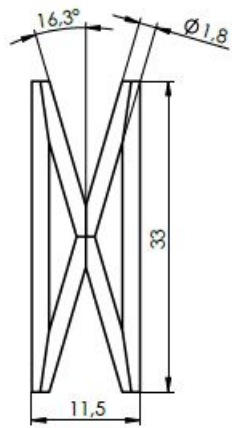
Escala		Revisão		Data	
 5:1	Desenhado			Master's Thesis  Name: Diogo Pereira n.º 81228 Curso: MEMEC	
	Verificado		31/12/2020		
	Projetado				
	Fabricado				
Material:		Notas:		Cell 3	
Tolerância Geral:					
Acabamentos:					
Folha	Desenho n.º	Folha	Fase	Revisão	
A4	3	1			



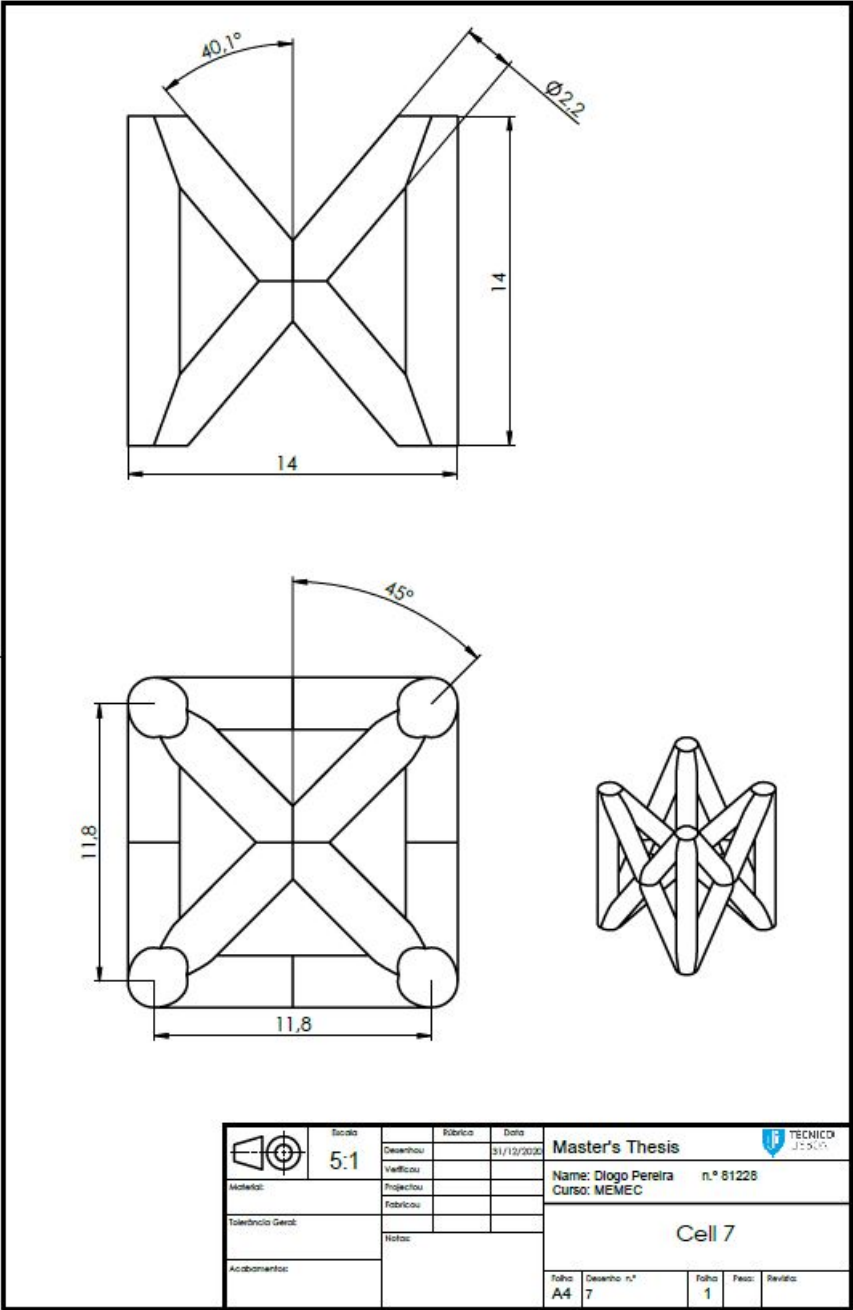
	Escala 5:1	Elabora _____	Data 31/12/2020	Master's Thesis				
	Verifica _____	Projecta _____	Fabrica _____	Name: Diogo Pereira	n.º 61228			
Materia:	Tolerância Geral:	Notas:	Cell 4					
Acabamentos:				Folha A4	Desenho n.º 4	Folha 1	Passos 1	Revisões 1



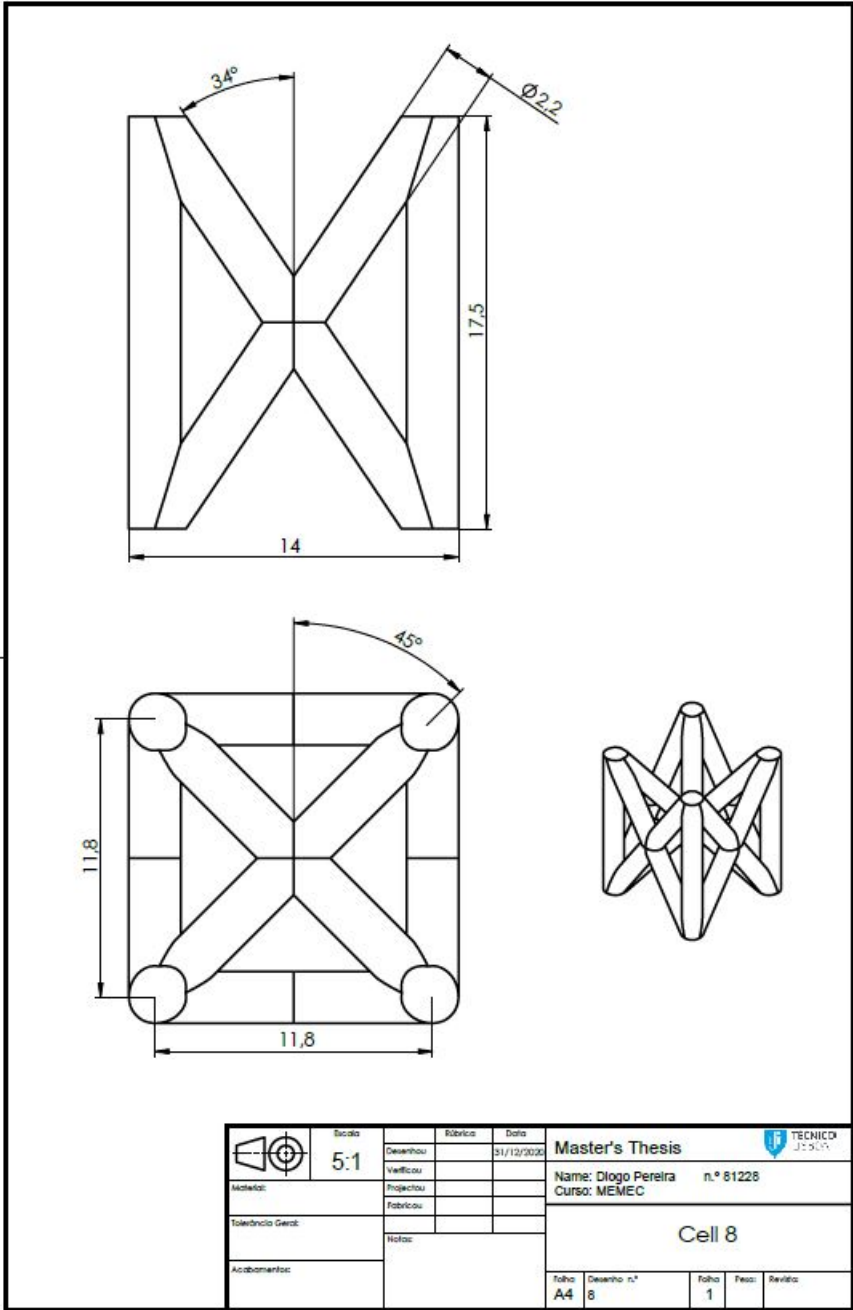
	Escala	5:1	Revisão	Data	Master's Thesis	
	Desenhado			31/12/2020		Name: Diogo Pereira n.º 81228
	Verificado					Curso: MEMEC
	Material:					
Tolerância Geral:					Cell 5	
Acabamentos:						
Notas:					Folha	
					Desenho n.º	
					Folha	
					Peso	
					Revisão	
					A4	
					5	
					1	



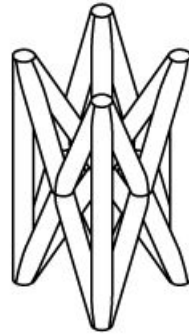
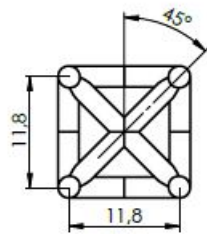
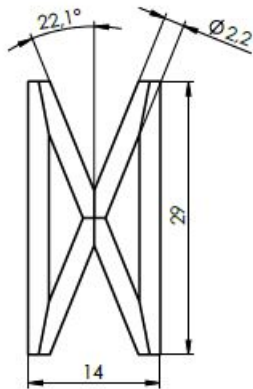
	Escala	Rótulo	Data	Master's Thesis
	2:1	Desenho	31/12/2020	
Matéria:	Projectado			Curso: MEMEC
Tolerância Geral:	Fabricado			Cell 6
Acabamentos:	Notas:			
Folha	Desenho n.º	Folha	Fase	Revisão
A4	6	1		



	Escala	Rótulo	Data	Master's Thesis
	5:1	Desenhado	31/12/2020	
Modelo:	Verificado	Projectado	Fabricado	Curso: MEMEC
Tolerância Geral:	Notas:			Cell 7
Acabamentos:	Folha			Folha
	A4			7
	Desenho n.º			1
	Folha			1
	Folha			1
	Folha			1



	Escala 5:1	Desenhou Verificou Projectou Fabricou	Data 31/12/2020	Master's Thesis	
	Material:	Tolerância Geral:	Notas:	Name: Diogo Pereira Curso: MEMEC	n.º 81228
Acabamentos:				Cell 8	
Folha A4	Desenho n.º 8	Folha 1	Fases 1	Revisões	












	Escala	Fórmula	Data	Master's Thesis	
	2:1	Desenho	31/12/2020		Name: Diogo Pereira n.º 81228
Material:	Verifica	Projecta	Fabrica	Curso: MEMEC	
Tolerância Geral:	Notas:			Cell 9	
Acabamentos:	Folha	Desenho n.º	Folha	Fase	Revisão
	A4	9	1		







Appendix B

Manufacturing Parameters

In the present appendix are included all the manufacturing parameters used to manufacture the sandwich panels. These parameters are included so that if someone wants to manufacture the panels, can do so.

 Shell ▼		
Wall Thickness	1	mm
Wall Line Count	3	
Top/Bottom Thickness	1	mm
Top Thickness	1	mm
Top Layers	5	
Bottom Thickness	1	mm
Bottom Layers	5	
Horizontal Expansion	0	mm
 Infill ▼		
Infill Density	20	%
Infill Pattern	Triangles	▼

 Material ▼		
Printing Temperature	205	°C
Build Plate Temperature	 60	°C
 Speed ▼		
Print Speed	70	mm/s
 Travel ▼		
Enable Retraction	<input checked="" type="checkbox"/>	
Z Hop When Retracted	<input checked="" type="checkbox"/>	
 Cooling ▼		
Enable Print Cooling	<input checked="" type="checkbox"/>	
Fan Speed	100	%
 Support ▼		
Generate Support	 <input type="checkbox"/>	

 Build Plate Adhesion ▼		
Enable Prime Blob	<input checked="" type="checkbox"/>	
Build Plate Adhesion Type	  Brim	▼
Build Plate Adhesion Extruder	 Extruder 1	 ▼
 Dual Extrusion ▼		
Enable Prime Tower	 <input type="checkbox"/>	